Università degli Studi di Trieste

Facoltà di Scienze Matematiche, Fisiche e Naturali
Dottorato di Ricerca in fisica Sperimentale - FIS/01
XXI Ciclo di Dottorato (2006-2008)

Measurement of the Branching Ratio

of the charmless decay $Bs \rightarrow \phi\phi$

at CDFII

Benedetto Di Ruzza

Advisors:

Dott.ssa Anna Maria Zanetti
Prof. Livio Lanceri

Coordinator:

Prof. Gaetano Senatore

2008

devoted to Trieste

Contents

III

IV

Chapter 1

Introduction

We present a study of the charmless $B_s \to \phi\phi$ decay performed with the CDFII detector at the Fermilab Tevatron Collider. Charmless B_s^0 decays currently can be studied only at the Tevatron and represent a field still to be fully explored that offers additional ways to test our present theoretical understanding. The $B_s \to \phi\phi$ belongs to a particular class of these decays: the B_s meson decays into a pair of vector particle and the final state is self-conjugate. It can be used to measure the B_s decay width difference $(\Delta\Gamma_s)$, to improve our understanding about the Cabibbo Kobayashi Maskawa matrix, and to perform tests of decay polarization predictions.

The $B_s \to \phi\phi$ decay proceeds through a $b \to s\bar{s}s$ transition and in the Standard Model the dominant process is the $b \to s$ "penguin" diagram. The same penguin amplitude is involved in several processes which have shown several discrepancies with the Standard Model predictions, raising considerable attention on the theoretical side and new physics interpretations have been considered to explain the experimental data. To shed light on this experimental and theoretical rather complex scenario, new and more precise measurements are clearly needed in as many interesting channels as possible. The study of $B_s \to \phi\phi$ channel is an important player in this experimental effort.

The $B_s \to \phi\phi$ decay has been observed for the first time by CDF in 2005 [1] in a data sample of 180 pb^{-1}; eight events have been seen and a first measurement of the Branching Ratio (BR) has been performed.
In this thesis we present an update of this measurement with an integrated luminosity of $2.9 fb^{-1}$. An improvement of a factor 5 compared to the previous Branching Ratio measurement is achieved.

In Chap.2 a short introduction on the Standard Model with special emphasis on the electroweak sector is presented.
In Chap.3 the Fermilab accelerator complex and the CDFII detector is described. The trigger strategy to select events relevant to B physics is ex-

plained in some detail.

In Chap.4 we present the data sample used for this analysis and some informations concerning the offline reconstruction program.

In Chap.5 the Monte Carlo program and its validation procedure are explained.

In Chap.6 the strategy of the Branching Ratio measurement and the optimization procedure used to define the analysis selection criteria both for the $B_s \rightarrow \phi\phi$ and the $B_s \rightarrow J/\psi\phi$ decays are presented.

In Chap.7 all the steps needed to perform the measurement of the BR are reported. Signal yields of the $B_s \rightarrow \phi\phi$ and the $B_s \rightarrow J/\psi\phi$ decays are presented. The trigger and selection efficiencies and the muon efficiency are evaluated. The ratio of the $BR(B_s \rightarrow \phi\phi)$ to the $BR(B_s \rightarrow J/\psi\phi)$ is measured and is used to compute the Branching Ratio of $B_s \rightarrow \phi\phi$. The systematic errors on the BR are estimated.

In Chap.8 we present the summary of our results.

Chapter 2

Theory Overview

In this chapter a general description of the Standard Model is given and some peculiarities of the neutral B mesons are described in more detail.

2.1   The Standard Model

The Standard Model (SM) of particle physics is the theoretical framework which provides the best description of the properties of the elementary particles and their interactions.

The Standard Model is a quantum field theory where fermions with spin $1/2$ interact with each other by exchanging bosons which transmit gauge forces. Table 2.1 shows the elementary particles (quarks and leptons) organized in three generations and Table 2.2 shows the known fundamental forces in nature. The Standard Model describes three of the four known fundamental interactions between the elementary particles.

  The SM unifies the electroweak theory and quantum chromodynamics into a structure which can be described by gauge groups $SU(3)_C \times SU(2)_L \times U(1)_Y$. The group $SU(3)_C$ is the gauge group of the theory of strong interactions known as *Quantum Chromodynamics* (QCD), and there are $3^2 - 1 = 8$ massless gauge bosons called "gluons", corresponding to the eight generators of the $SU(3)_C$ group.

The group $SU(2)_L$ has three generators of gauge symmetry and would nor-

		Generation 1		Generation 2		Generation 3	
Quarks		Up	u	Charm	c	Top	t
		Down	d	Strange	s	Bottom	b
Leptons		Electron	e	Muon	μ	Tau	τ
		Electron Neutrino	ν_e	Muon Neutrino	ν_μ	Tau Neutrino	ν_τ

Table 2.1: *Generations of the Standard Model*

Interaction field	Boson	Spin
Gravitation field	Gravitons	2
Weak field W^+,W^-,Z	particles	1
Electromagnetic field	Photons	1
Strong filed	Gluons	1

Table 2.2: *Fundamental Interactions*

mally give three massless gauge bosons. However the gauge symmetry is broken through a mechanism called *Spontaneous Symmetry Breaking* (SSB), which occurs because of a $SU(2)$ doublet scalar field called the Higgs field [2].

$$SU(3)_C \times SU(2)_L \times U(1)_Y \quad \xrightarrow{SSB} \quad SU(3)_C \times U(1)_{QED} \qquad (2.1)$$

The SSB mechanism generates the masses of the weak gauge bosons, and gives rise to the appearance of a physical scalar particle in the model, the so-called Higgs. The fermion masses are also generated through the SSB.
The flavor sector of the Standard Model is based on the Spontaneously broken gauge group

$$SU(2)_L \times U(1)_Y \quad \longrightarrow \quad U(1)_{QED} \qquad (2.2)$$

where the three gauge bosons (W^+, W^- and Z^0) acquire mass by coupling to the Higgs field. These bosons mediate the weak force, while the massless photon in $U(1)_{QED}$ group mediates the electromagnetic force. The large masses of the gauge bosons are responsible for the short range of the weak force and the "weakness" of the weak interactions. The Higgs Field, with four degrees of freedom, loses one degree of freedom to each of the massive bosons, the other degree of freedom is the Higgs Boson.
The SM constitutes one of the most successful achievements in modern particle physics. It provides a very elegant theoretical framework, which is able to describe most of the known experimental facts in particle physics with high precision.
Direct searches for the Higgs at the e^+e^- collider LEP, at CERN, have excluded it below a mass of 114 GeV/c^2 (at the 95% Confidence Level). It is currently being sought at Fermilab. As of August 2008, combined result from CDF and D0 experiments at the Tevatron excluded the Higgs boson at 170 GeV/c^2 (at 95% confidence level) [3]. If the Higgs boson is not found at Tevatron, the Large Hadron Collider (LHC) at CERN, a high luminosity machine with a center of mass energy of 14 TeV, will have a much better chance.
Although the Standard Model has achieved great success since its birth, it is still not a perfect theory for several reasons.

- The primary reason is that it does not include the gravity, one of the four known fundamental interactions.

- There are many free parameters in the Standard Model, such as the fermion masses and coupling constants, which are not predicted by the theory.

- There are no explanation for the three generations of elementary particles.

For these reasons, there is both theoretical interest in a more complete theory and experimental interest in the search for phenomenon beyond the Standard Model.

2.2   The QCD interaction in the Standard Model

Assuming that mesons are $M = q\bar{q}$ states, while baryons have three quark constituents, $B = qqq$, one can nicely classify the entire hadronic spectrum. However, in order to satisfy the FermiDirac statistics one needs to assume the existence of a new quantum number, color, such that each species of quark may have $N_C = 3$ different colors: $q^\alpha, \alpha = 1, 2, 3$ (red, green, blue). Baryons and mesons are then described by the color-singlet combinations

$$B = \tfrac{1}{\sqrt{6}}\epsilon^{\alpha\beta\gamma}|q_\alpha q_\beta q_\gamma\rangle \quad ; \quad M = \tfrac{1}{\sqrt{2}}\delta^{\alpha\beta}|q_\alpha \bar{q}_\beta\rangle \tag{2.3}$$

In order to avoid the existence of non-observed extra states with non-zero color, one needs to further postulate that all asymptotic states are colorlessly, i.e., singlets under rotations in color space. This assumption is known as the confinement hypothesis, because it implies the non-observability of free quarks: since quarks carry color they are confined within color-singlet bound states.
Electromagnetic interactions are associated with the particle electric charges, while the quark flavors (up, down, strange, charm, bottom, top) are related to electroweak phenomena. The strong forces are flavor conserving and flavor independent; the carriers of the electroweak interaction (γ, Z, $W^\pm$) do not couple to the quark color. Thus it seems natural to take color as the charge associated with the strong forces and try to build a quantum field theory based on it [4] [5].

2.2.1   Non-Abelian gauge symmetry

Let us denote q_f^α a quark field of color α and flavor f. To simplify the equations let us adopt a vector notation in color space: $q_f^T \equiv \left(q_f^1, q_f^2, q_f^3\right)$
The free Lagrangian

$$\mathcal{L}_0 = \sum_f \bar{q}_f(i\gamma^\mu\partial_\mu - m_f)q_f \tag{2.4}$$

is invariant under arbitrary global $SU(3)_C$ transformations in color space,

$$q_f^\alpha \to (q_f^\alpha)' = U_\beta^\alpha q_f^\beta, \quad UU^\dagger = U^\dagger U = \mathbb{1}, \quad \det U = 1 \tag{2.5}$$

The $SU(3)_C$ matrices can be written in the form

$$U = exp\{i\tfrac{\lambda^a}{2}\theta_a\} \tag{2.6}$$

where $\frac{1}{2}\lambda^a(a = 1, 2, \ldots, 8)$ denote the generators of the fundamental representation of the $SU(3)_C$ algebra, and a are arbitrary parameters. The matrices λ^a are traceless and satisfy the commutation relations

$$U = [\tfrac{\lambda^a}{2}, \tfrac{\lambda^b}{2}] = if^{abc}\tfrac{\lambda^c}{2}, \tag{2.7}$$

with f^{abc} the $SU(3)_C$ structure constants, which are real and totally antisymmetric.

We require the Lagrangian to be also invariant under local $SU(3)_C$ transformations, $\theta_a = \theta_a(x)$. To satisfy this requirement, we need to change the quark derivatives by covariant objects. Since we have now eight independent gauge parameters, eight different gauge bosons $G_a^\mu(x)$, the so-called gluons, are needed:

$$D^\mu q_f \equiv [\partial^\mu + ig_s\tfrac{\lambda^a}{2}G_a^\mu(x)]q_f \equiv [\partial^\mu + ig_sG^\mu(x)]q_f \tag{2.8}$$

Notice that we have introduced the compact matrix notation:

$$[G^\mu(x)]_{\alpha\beta} \equiv \left(\tfrac{\lambda^a}{2}\right)_{\alpha\beta} G_a^\mu(x) \tag{2.9}$$

We want $D^\mu q_f$ to transform in exactly the same way as the color-vector q_f; this fixes the transformation properties of the gauge fields:

$$D^\mu \to (D^\mu)' = UD^\mu U^\dagger \quad G^\mu \to (G^\mu)' = UG^\mu U^\dagger + \tfrac{i}{g_s}\left(\partial^\mu U\right)U^\dagger \tag{2.10}$$

Under an infinitesimal $SU(3)_C$ transformation:

$$q_f^\alpha \to \left(q_f^\alpha\right)' = q_f^\alpha + i\left(\tfrac{\lambda^a}{2}\right)_{\alpha\beta}\delta\theta_a q_f^\beta$$
$$G_a^\mu \to (G_a^\mu)' = G_a^\mu - \tfrac{i}{g_s}\partial^\mu\left(\delta\theta_a\right) - f^{abc}\delta\theta_b G_c^\mu.$$

The non-commutativity of the $SU(3)_C$ matrices gives rise to an additional term involving the gluon fields themselves. For constant $\delta\theta_a$, the transformation rule for the gauge fields is expressed in terms of the structure constants f^{abc}; thus, the gluon fields belong to the adjoint representation of the color group. Note also that there is a unique $SU(3)_C$ coupling g_s. In QED it is possible to assign arbitrary electromagnetic charges to the different fermions. Since the commutation relation (2.7) is non-linear, this freedom

does not exist for $SU(3)_C$.

To build a gauge-invariant kinetic term for the gluon fields, we introduce the corresponding field strengths:

$$G^{\mu\nu}(x) \equiv -\frac{i}{g_s}[D^\mu, D^\nu] = \partial^\mu G^\nu - \partial^\nu G^\mu + ig_s[G^\mu, G^\nu] \equiv \frac{\lambda^a}{2}G_a^{\mu\nu}(x),$$
$$G_a^{\mu\nu}(x) \equiv \partial^\mu G_a^\nu - \partial^\nu G_a^\mu - g_s f^{abc} G_b^\mu G_c^\nu$$

Under a gauge transformation we have,

$$G^{\mu\nu} \rightarrow (G^{\mu\nu})' = U G^{\mu\nu} U^\dagger \tag{2.11}$$

and the color trace $\mathrm{Tr}(G_a^{\mu\nu} G_{\mu\nu}^a) = \frac{1}{2}G_a^{\mu\nu}G_{\mu\nu}^a$ remains invariant.

Taking the proper normalization for the gluon kinetic term, we finally have the $SU(3)_C$ invariant Lagrangian of Quantum Chromodynamics (QCD):

$$\mathcal{L}_{QCD} \equiv -\frac{1}{4}G_a^{\mu\nu}G_{\mu\nu}^a + \sum_f \bar{q}_f \left(i\gamma^\mu D_\mu - m_f\right) q_f \tag{2.12}$$

It is worthwhile to decompose the Lagrangian into its different pieces:

$$
\begin{aligned}
\mathcal{L}_{QCD} \equiv \quad & -\frac{1}{4}\left(\partial^\mu G_a^\nu - \partial^\nu G_a^\mu\right)\left(\partial_\mu G_\nu^a - \partial_\nu G_\mu^a\right) + \sum_f \bar{q}_f^\alpha \left(i\gamma^\mu D_\mu - m_f\right) q_f^\alpha \\
& -g_s G_a^\mu \sum_f \bar{q}_f^\alpha \gamma_\mu \left(\tfrac{\lambda^a}{2}\right)_{\alpha\beta} q_f^\beta \\
& +\frac{g_s}{2} f^{abc}\left(\partial^\mu G_a^\nu - \partial^\nu G_a^\mu\right) G_\mu^b G_\nu^c - \frac{g_s^2}{4} f^{abc} f_{ade} G_b^\mu G_c^\nu G_\mu^d G_\nu^e
\end{aligned}
$$

The first line contains the correct kinetic terms for the different fields, which give rise to the corresponding propagators. The color interaction between quarks and gluons is given by the second line; it involves the $SU(3)_C$ matrices λ^a. Finally, owing to the non-Abelian character of the color group, the $G_a^{\mu\nu}G_{\mu\nu}^a$ term generates the cubic and quartic gluon self-interactions shown in the last line; the strength of these interactions (Fig. 2.1) is given by the same coupling gs which appears in the fermionic piece of the Lagrangian.
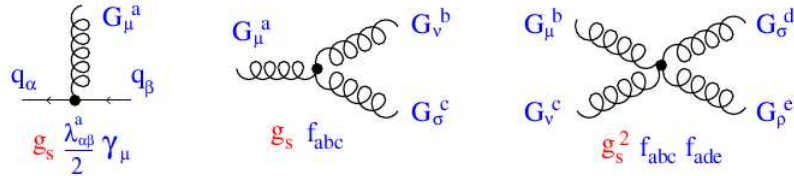

Figure 2.1: *Interaction vertexes of the QCD Lagrangian.*

In spite of the rich physics contained in it, the Lagrangian in eq. 2.12 looks very simple because of its color symmetry properties. All interactions are given in terms of a single universal coupling gs, which is called the strong

$$\begin{aligned}
\mathbf{E}_R &= (e_R, \mu_R, \tau_R), \quad Y_{\mathbf{E}} = -2; \\
\mathbf{U}_R &= (u_R, c_R, t_R), \quad Y_{\mathbf{U}} = \frac{4}{3}; \\
\mathbf{D}_R &= (d_R, s_R, b_R), \quad Y_{\mathbf{D}} = -\frac{2}{3};
\end{aligned}$$

Table 2.3: *Right-Handed Fermions Singlets*

coupling constant. The existence of self-interactions among the gauge fields is a new feature that is not present in QED; it seems then reasonable to expect that these gauge self-interactions could explain properties like asymptotic freedom (strong interactions become weaker at short distances) and confinement (the strong forces increase at large distances), which do not appear in QED [6].

2.3 The CP violation in the Standard Model

In the Standard Model, there are only two ways to break the CP symmetry. The first of these is in the QCD Lagrangian. However, this has not been found experimentally, On the other hand, CP symmetry can also be broken in the weak interaction through the Cabibbo-Kobayashi-Maskawa (CKM) mechanism (see later), which has been verified by the experiments. Further from a theoretical point of view, the CKM model could exist along with other sources of CP violation. We therefore will discuss how the CKM mechanism explains the CP violation in the Standard Model.

One of the striking features of charged current weak interactions is that they couple to both vector and axial vector currents ($V - A$ structure), unlike QED and QCD which couple solely to a vector-vector current. Consequently, the left-handed and right-handed fermions transform differently under the electroweak gauge group $SU(2) \times U(1)$. The right-handed fermions are singlets under $SU(2)$, and do not couple to charge $W^{\pm}$ bosons (see table 2.3).

On the other hand, left-handed fermions do couple to $W^{\pm}$, and are doublets under $SU(2)$ (see table 2.4).

In the above definitions, $Y = 2(Q - I_3)$ is the hypercharge, where Q is charge, and I_3 is the weak isospin. In the Standard Model, fermion masses, flavor violation and CP violation all arise from Yukawa interactions among the fermion fields and with the Higgs field. We can see this considering the simple situation where we only have the first leptons generation, then the Lagrangian interaction is:

$$\mathcal{L}_Y = -y e^{i\delta} \bar{l}_L \phi e_R - y e^{-i\delta} \bar{e}_R \phi^{\dagger} l_L \tag{2.13}$$

$$\mathbf{L}_L = \left[\begin{pmatrix} \nu_e \\ e \end{pmatrix}_L, \begin{pmatrix} \nu_\mu \\ \mu \end{pmatrix}_L, \begin{pmatrix} \nu_\tau \\ \tau \end{pmatrix}_L \right], \quad Y_{\mathbf{L}} = -1;$$

$$\mathbf{Q}_L = \left[\begin{pmatrix} u \\ d \end{pmatrix}_L, \begin{pmatrix} c \\ s \end{pmatrix}_L, \begin{pmatrix} t \\ b \end{pmatrix}_L \right], \quad Y_{\mathbf{Q}} = \frac{1}{3};$$

Table 2.4: *Left-Handed Fermions Doublets*

where $\bar{l}_L = (\bar{\nu}u_L, \bar{e}_L)$, and y is real. To preserve Lorentz invariance ϕ must have spin 0. To preserve invariance under $U(1)$, ϕ must have hypercharge $Y_\phi = Y_L - Y_E = +1$. To preserve invariance under $SU(2)$, ϕ must be a doublet:

$$\phi = \begin{pmatrix} \phi^+ \\ \phi^- \end{pmatrix} \tag{2.14}$$

where the superscripts denote the electric charge using relationship $Q = I_3 + Y/2$. This interaction is called a Yukawa interaction, because similar interaction was introduced by Yukawa to describe decay $\pi^+ \to \mu^+ \nu_\mu$, and y is called the Yukawa coupling. At first look, the interaction in Eq. 2.13 seems to be CP violated with phase δ. However, one can change the phases of l_L and e_R to remove it. Thus, the Yukawa interaction conserves CP. The renormalizable interaction for the potential energy of the ϕ field is

$$V(\phi) = -\lambda v^2 \phi^\dagger \phi + \lambda (\phi^\dagger \phi)^2 \tag{2.15}$$

with two parameters, v and λ. The vacuum state with no propagating particles is realized when one minimize $V(\phi)$. Parameter λ must be positive to obtain stable vacuum. If v^2 is negative, there is a single minimum of the potential with vacuum expectation value $\langle \phi \rangle = 0$, which does not interest us here. If v^2 is greater than 0, then $V(\phi)$ takes the shape of a saddle with three-dimensional family of minima:

$$\langle \phi \rangle = e^{i\langle \epsilon^a \rangle \sigma_a / 2v} \begin{pmatrix} 0 \\ v/\sqrt{2} \end{pmatrix} \tag{2.16}$$

One can set $\langle \epsilon^a \rangle$ to 0 by proper $SU(2)$ transformation. Although the full Lagrangian respects $SU(2) \times U(1)$ gauge symmetry, this vacuum solution does not. This is the spontaneous symmetry breaking.

If fluctuation around the expectation value is introduced, physical particles can be obtained, so one writes

$$\phi(x) = e^{i\epsilon^a(x)\sigma_a/2v} \begin{pmatrix} 0 \\ [v + h(x)]/\sqrt{2} \end{pmatrix} \tag{2.17}$$

Masses of the physical particles are found by inserting the above equation into the interactions in the Lagrangian and examining the corresponding quadratic terms. For example, one can obtain the electron masses $m_e = yv/\sqrt{2}$ by comparing the $\bar{e}_R e_L$ terms in L_Y. Similarly, field h (the Higgs field) is found to have a mass $m_h = \sqrt{2\lambda}v$ from $V(\phi)$. By examining the kinetic energy of the scalar field, one obtain masses for three of the gauge bosons: $W^\pm$, Z^0, while photon remains massless [7].

The same doublet as for leptons is used to repeat the construction with $(\bar{u}_L, \bar{d}_L)$ and d_R with hypercharge $Y_Q - Y_D = +1$. But for $(\bar{u}_L, \bar{d}_L)$ and d_R, a doublet with hypercharge $Y_Q - Y_D = +1$ is necessary, so the Standard Model uses the charge-conjugate of the doublet used for leptons:

$$\tilde{\phi} \;=\; i\sigma_2\phi^* = \left(\begin{array}{c} \bar{\phi}^0 \\ -\phi^- \end{array} \right) \qquad (2.18)$$

With three generations of fermions, the full set of Yukawa interaction becomes complicated with different generations interacting with each other as in

$$\mathcal{L}_Y \;=\; -\sum_{i,j=1}^{3} \; [\hat{y}^e_{ij}\bar{\mathbf{L}}^i_L\phi\mathbf{E}^j_R + \hat{y}^d_{ij}\bar{\mathbf{Q}}^i_L\phi\mathbf{D}^j_R + \hat{y}^u_{ij}\bar{\mathbf{Q}}^i_L\tilde{\phi}\mathbf{U}^j_R] \qquad (2.19)$$

The Yukawa couplings y_{ij} could be complex in principle. For the leptons, however, as mentioned above, one can transform the lepton fields while keeping the non-Yukawa part of the Lagrangian invariant:

$$\begin{aligned} \mathbf{E}_R \rightarrow & \quad R\mathbf{E}_R, \quad \bar{\mathbf{E}}_R \rightarrow \quad \bar{\mathbf{E}}_R R^\dagger \\ \mathbf{L}_L \rightarrow & \quad S\mathbf{L}_L, \quad \bar{\mathbf{L}}_L \rightarrow \quad \bar{\mathbf{L}}_L S^\dagger \end{aligned} \qquad (2.20)$$

where $R \in U(3)_{\mathbf{E}_R}$ and $S \in U(3)_{\mathbf{L}_L}$. With these transformations, the new Yukawa matrix will be $y^e = S\hat{y}^e R^\dagger$. It is easy to see that, with the proper choice, y^e can be made diagonal and real. So the lepton Yukawa interactions will conserve CP.

For the quarks, the non-Yukawa part of the Lagrangian is invariant with transformations:

$$\begin{aligned} \mathbf{D}_R \rightarrow & \quad R_d\mathbf{D}_R, \quad \bar{\mathbf{D}}_R \rightarrow \quad \bar{\mathbf{D}}_R R^\dagger_d \\ \mathbf{U}_R \rightarrow & \quad R_u\mathbf{U}_R, \quad \bar{\mathbf{U}}_R \rightarrow \quad \bar{\mathbf{U}}_R R^\dagger_u \\ \mathbf{Q}_L \rightarrow & \quad S_u\mathbf{Q}_L, \quad \bar{\mathbf{Q}}_L \rightarrow \quad \bar{\mathbf{Q}}_L R^\dagger_u \end{aligned} \qquad (2.21)$$

Although we may exploit S_u and R_u to transform Yukawa coupling matrix $\tilde{y}^u$ into a diagonal and real one y^u, coupling matrix $\tilde{y}^d$ cannot be transformed into a diagonal or real one simultaneously in general. Instead, it has the following form:

$$S_u \tilde{y}^d R_d^\dagger = \quad S_u S_d^\dagger S_d \tilde{y}^d R_d^\dagger = \quad V y^d, \tag{2.22}$$

where y^d is real and diagonal with proper choice of S_d, and the matrix

$$V \quad = \quad S_u S_d^\dagger \tag{2.23}$$

is just the Cabibbo-Kobayashi-Maskawa (CKM) matrix [8].
With this basis, the CKM matrix appears in the the charged current interactions (that is the $W^\pm$ interactions) for quarks

$$-\mathcal{L}_{W^\pm} = \quad \frac{g}{\sqrt{2}} \quad (\bar{u} \quad \bar{c} \quad \bar{t})_L \gamma^\mu V_{\text{CKM}} \begin{pmatrix} d \\ s \\ b \end{pmatrix}_L W_\mu^+ + h.c. \tag{2.24}$$

To emphasize the physical transitions associated with the CKM matrix, one can write the explicit form of the CKM matrix as

$$V_{\text{CKM}} \quad = \quad \begin{pmatrix} V_{ud} & V_{us} & V_{ub} \\ V_{cd} & V_{cs} & V_{cb} \\ V_{td} & V_{ts} & V_{tb} \end{pmatrix} \tag{2.25}$$

In principle, the magnitude of all the matrix elements can be measured through the decay with corresponding quarks. For example |Vud| can be determined from nuclear β decay, |Vus| can be measured from semileptonic kaon decays, |Vub| and |Vcb| can be measured from inclusive or exclusive b decay, |Vcd| and |Vcs| can be extracted from semileptonic or leptonic charm decays, |Vtd| and |Vts| can be only accessed through box diagrams or through second order weak interactions such as QCD penguin diagrams, and |Vtb| can be determined from top decays.
To find how many observable parameters the CKM matrix contains, one starts from $2N^2$ free parameters of an arbitrary $N \times N$ complex matrix and reduce that number by applying constraints. Because the CKM matrix is unitary, $|V_{\text{CKM}}|^2 = 1$ gives N^2 constraints, so there are N^2 parameters left. Mathematically, with the unitarity property, one can prove that of the N^2 independent parameters, there are $N(N-1)/2$ real and N(N +1)/2 imaginary components.
One can further change the phase of each of the 2N quark states independently without altering the physics and absorb imaginary parts, but an overall phase change still leaves V_{CKM} invariant, so the number of remaining independent imaginary components is $N(N+1)/2-(2N-1) = (N-1)(N-2)/2$ and the total number of independent parameters is $N^2-(2N-1) = (N-1)^2$.

For three generation of quarks with $N = 3$, the CKM matrix has four observable parameters; of them three are real and one is a phase factor. These four numbers are fundamental constants of nature, just like the Fermi coupling constant, and need to be determined from experiments. So the CKM matrix can be parametrized by four parameters. One parametrization favored by the Particle Data Group uses three rotation angles, $\theta_{12}, \theta_{23}, \theta_{13}$ and one complex phase δ_{13}, such that V_{CKM} is:

$$\begin{pmatrix} c_{12}c_{13} & s_{12}c_{13} & s_{13}e^{-i\delta_{13}} \\ -s_{12}c_{23} - c_{12}s_{23}s_{13}e^{i\delta_{13}} & c_{12}c_{23} - s_{12}s_{23}s_{13}e^{i\delta_{13}} & s_{23}c_{13} \\ s_{12}s_{23} - c_{12}c_{23}s_{13}e^{i\delta_{13}} & -c_{12}s_{23} - s_{12}c_{23}s_{13}e^{i\delta_{13}} & c_{23}c_{13} \end{pmatrix} \quad (2.26)$$

where $s_{ij} = sin(\theta_{ij})$, $c_{ij} = cos(\theta_{ij})$. Another popular approximation of the CKM matrix which emphasizes the hierarchy in the size of the matrix elements is due to Wolfenstein [9]. By introducing

$$\begin{aligned} \lambda &\equiv s_{12} \\ A &\equiv \frac{s_{23}}{s_{12}^2} \\ \rho &\equiv \frac{s_{13}cos(\delta_{13})}{s_{12}s_{12}} \\ \eta &\equiv \frac{s_{13}sin(\delta_{13})}{s_{12}s_{12}} \end{aligned} \quad (2.27)$$

the matrix can be expanded in terms of λ and the we can write V_{CKM} as:

$$\begin{pmatrix} 1 - \frac{1}{2}\lambda^2 - \frac{1}{8}\lambda^4 & \lambda & A\lambda^3(\rho - i\eta) \\ -\lambda + \frac{1}{2}A^2\lambda^5 - A^2\lambda^5(\rho - i\eta) & 1 - \frac{1}{2}\lambda^2 - \frac{1}{8}\lambda^4(1 + 4A^2) & A\lambda^2 \\ A\lambda^3(1 - \bar{\rho} - i\bar{\eta}) & -A\lambda^2 + A\lambda^4(\frac{1}{2} - \rho - i\eta) & 1 - \frac{1}{2}A^2\lambda^4 \end{pmatrix} + \mathcal{O}(\lambda^6) \quad (2.28)$$

Here, λ is also the sine of the Cabibbo angle: $\lambda = sin\theta_c = |V_{us}|$ and the shorthand notation $\bar{\rho} = \rho(1 - \lambda^2/2)$, $\bar{\eta} = \eta(1 - \lambda^2/2)$ is used.
From several experiment measurements we have[10] :

$$\begin{aligned} \lambda &\sim 0.23 \\ A &\sim 0.81 \\ \bar{\rho} &\sim 0.14 \\ \bar{\eta} &\sim 0.34 \end{aligned} \quad (2.29)$$

CP violation arises from the complex phase and the fact that CKM matrix is non Hermitian. For example the $b \to uW$ transition in the Standard Model has coupling

$$\mathcal{L} = -\frac{g}{\sqrt{2}}[V_{ub}\bar{u}_L\gamma^\mu b_L W_\mu^+ + V_{ub}^*\bar{b}_L\gamma^\mu u_L W_\mu^-] \quad (2.30)$$

With a CP transformation, one obtains

$$CP\mathcal{L}(CP)^{-1} = -\frac{g}{\sqrt{2}}[V_{ub}\bar{b}_L\gamma^\mu u_L W_\mu^- + V_{ub}^*\bar{u}_L\gamma^\mu b_L W_\mu^+] \quad (2.31)$$

Clearly, this is equivalent to the previous equation only when $Vub = V^*ub$. As shown already, there is in general no way one can rotate the quark fields to remove the phase in the coupling, so CP is violated in this interaction. Furthermore we can have CP violation only with at least 3 generations of fermions. With only 2 generations the matrix is 2×2 and have only two free parameters, so the matrix can be only real.

One can gauge the size of the CP violation with a quantity (the Jarlskog determinant [11]) defined as

$$J_{CP} = Im(V_{i\alpha}V_{j\beta}V_{iB}^*V_{j\alpha}^*), (i \neq \alpha, j \neq \beta) \tag{2.32}$$

J_{CP} has nine possible combinations arising from the unitarity of the CKM matrix, and all of them are equal up to an overall sign. Using the parametrization of the CKM matrix, J_{CP} can be calculated as $\lambda^6 A^2 \eta \simeq \mathcal{O}(10^{-5})$, meaning that the CP violation is small in the Standard Model.

All the physics from the CKM matrix can be reflected, applying the unitarity constraint to different columns and rows of CKM matrix, in six "unitarity" triangles, (because the sum of three complex number equals to 0 can be plotted as the closed sum of three vectors, so a triangle) For example, if one apply unitarity to the first and third columns, one obtains

$$V_{ud}V_{ub}^* + V_{cd}V_{cb}^* + V_{td}V_{tb}^* = 0 \tag{2.33}$$

The unitarity triangle is just a geometric representation of this equation, which is a triangle in the complex plane known as the "db" triangle (see Fig. 2.2).

One can choose to orient the side $V_{cd}V_{cb}^*$ along the horizontal direction and to normalize it to unit length dividing by the magnitude. In this geometrical representation the angles of the triangle are related to the CP phase according to

$$\begin{aligned}
\alpha &\equiv arg\left(-\frac{V_{td}V_{tb}^*}{V_{ud}V_{ub}^*}\right) \\
\beta &\equiv arg\left(-\frac{V_{cd}V_{cb}^*}{V_{td}V_{tb}^*}\right) \\
\gamma &\equiv arg\left(-\frac{V_{ud}V_{ub}^*}{V_{cd}V_{cb}^*}\right)
\end{aligned} \tag{2.34}$$

These angles can be measured through time-dependent CP asymmetries in exclusive channels; for example, the angle β can be determined from $B_d^0 \rightarrow J/\psi K_s^0$ decays.

Using another unitary relation

$$V_{us}V_{ub}^* + Vcs V_{cb}^* + V_{ts}V_{tb}^* = 0 \tag{2.35}$$

we obtain another "squashed" triangle, which is usually called the "sb" triangle. As shown in Figure 2.4, all the sides of "db" triangle are of order of
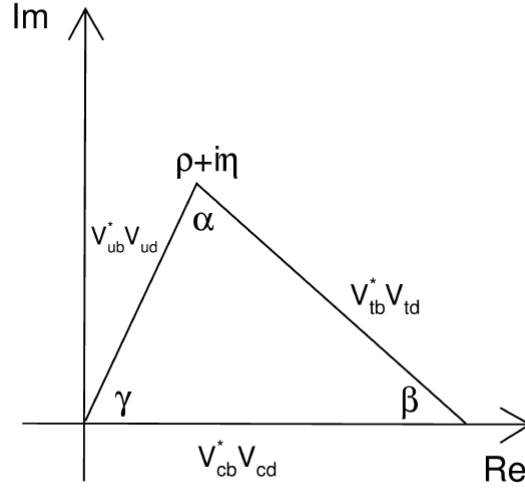
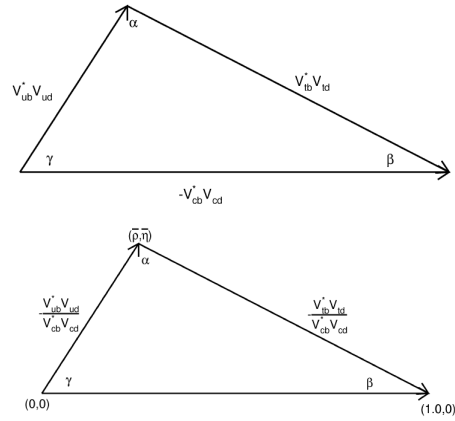Figure 2.2: *The CKM unitarity triangle in the complex plane.*

Figure 2.3: *Illustration of db unitarity triangle (top), and rescaled db unitarity triangle (bottom) with $\bar{\rho}\bar{\eta}$ defined*

λ^3, while for the "sb" triangle, two sides are of order of λ^2, the third one is of order of λ^4. This makes the "db" triangle much higher than the "sb" triangle, but one can easily prove, by using unitarity property of the CKM matrix, all the unitarity triangles have the same area, $J_{CP}/2$.

The smaller angle of the "sb" triangle is defined as

$$\beta_s \equiv arg\left(-\frac{V_{cs}V_{cb}^*}{V_{ts}V_{tb}^*}\right) \tag{2.36}$$

Using the parametrization in eq. 2.28 β_s is calculated to be $\beta_s = \eta\lambda^2 \sim 0.018$. In principle, it can be measured from $B_s^0 \to J/\psi\phi$ decays, and at present it is one of the most important efforts made at Fermilab.
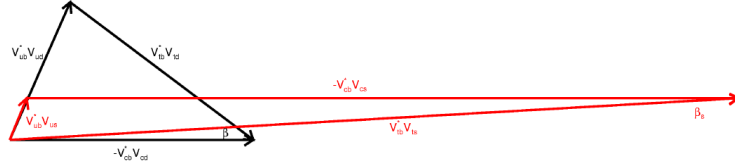

Figure 2.4: *Comparison of sb unitarity triangle (red) and db unitarity triangle. One side of the sb triangle is about 4 times smaller than the side of db triangle, but the other two sides of sb triangle are 4 times bigger than the sides in db triangle.*

2.4   The mixing effect in the neutral mesons

One consequence of the flavor mixing modeling within the framework of the Standard Model is the mixing of neutral mesons B_d and B_s, which arises from box diagrams as shown in Figure 2.5. The process of mixing [14] change the initial state which evolves at time t in a superposition of flavor eigenstates. Flavor eigenstates B_s^0 and $\bar{B}_s^0$ evolves according to the Schrodinger equation:
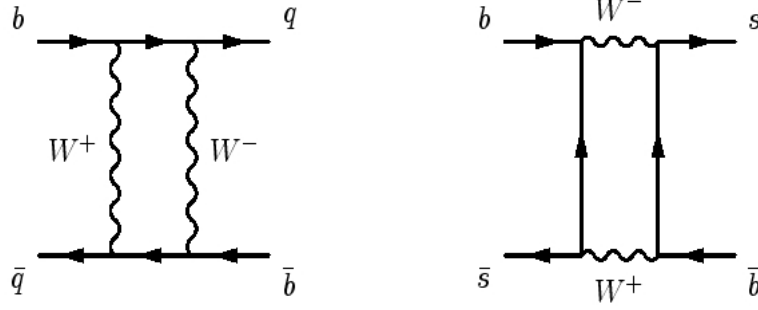
$$\frac{d}{dt}\begin{pmatrix} B_s^0(t) \\ \bar{B}_s^0(t) \end{pmatrix} = \left[\bar{M} - \frac{i}{2}\bar{\Gamma}\right]\begin{pmatrix} B_s^0(t) \\ \bar{B}_s^0(t) \end{pmatrix} \tag{2.37}$$

where $\bar{M}$ and $\bar{\Gamma}$ are the 2×2 mass and decay matrixes.

Solving this equation, we have that the eigenstates of the mass matrix are a linear combination of the flavor eigenstates.

$$\mid B_s^L >= p \mid B_s^0 > -q \mid \bar{B}_s >$$

$$\mid B_s^H >= p \mid B_s^0 > +q \mid \bar{B}_s^0 >$$

15

Figure 2.5: *Box diagrams contributing to $B_q^0 - \bar{B}_q^0$ flavor mixing.*

where $\frac{p}{q} = \sqrt{\frac{M_{12}^* - \frac{i}{2}\Gamma_{12}^*}{M_{12} - \frac{i}{2}\Gamma_{12}}}$.

These two are called respectively *light* (L) and *heavy* (H) eigenstates. Solving the eigenvalue problem we obtain:

$$\lambda_{L,H} = (M - \frac{i}{2}\Gamma) \pm \frac{p}{q}(M_{12} - \frac{i}{2}\Gamma_{12})$$

and the time evolution of the the mass eigenstates is

$$\mid B_s^{H,L}(t) >=\mid B_s^{H,L}(0) > e^{-i\lambda_{L,H}t} =\mid B_s^{H,L}(0) > e^{-iM_{L,H}t - \frac{1}{2}\Gamma_{L,H}t}$$

from this equation we can have that the time evolution of the flavor states is

$$\mid B_s(t) >= g_+(t) \mid B_s^0 > + \frac{q}{p}g_-(t) \mid \bar{B}_s^0 >$$

$$\mid B_s(t) >= g_+(t) \mid \bar{B}_s^0 > + \frac{q}{p}g_-(t) \mid B_s^0 >$$

where

$$g_{\pm}(t) = \frac{1}{2}(e^{-\lambda_L t} \pm e^{-i\lambda_H t})$$

and we can compute the probability that a state with a defined flavor at time $t = 0$ has an equal or different flavor at time $t > 0$. For example we have:

$$\mid < B_s^0 \mid B_s^0(t) > \mid^2 =\mid g_+(t) \mid^2$$

where

$$\mid g_+(t) \mid^2 = \frac{1}{2}[cosh(\frac{\Delta\Gamma_s t}{2}) \pm \cos(\Delta M_s t)]e^{-\Gamma t}$$

$$\Delta M_s = M_H - M_L \qquad \Delta\Gamma_s = \Gamma_L - \Gamma_H$$

The mixing physical observables are ΔM_s, $\Delta\Gamma_s$.

Currently, the experimental values of ΔM_s is evaluated only in CDFII and D0 [?]

$$\Delta M_s = [17.77 \pm 0.12] \ ps^{-1}$$

16

This measurement require a very good resolution in the decay length and the possibility to distinguish between a particle/antiparticle state in the meson B_s^0 production.

Combining the LEP, CDF and $D0$ measurements, we have [12]

$$\Delta\Gamma_s = [0.102 \pm 0.043] \ ps^{-1}$$

This measurement can be performed using decays of the B_s^0 mesons in two vector particles and assuming that with good approximation mass eigenstates are CP eigenstates too [13]. For example in CDFII, $\Delta\Gamma_s$ measurement was made using the $B_s \to J/\psi\phi$ decay [14].

2.5   b quark production

At the Tevatron, b quarks are produced dominantly through QCD processes. Contributions from electroweak processes, such as $W^+ \to c\bar{b}$ and $Z \to b\bar{b}$ are negligible.

The main production mechanism for $b\bar{b}$ pairs is the gluon-gluon fusion process $g + g \to b + \bar{b}$ shown in Fig.2.6. At the lowest order there are 3 processes contributing in QCD to the $b\bar{b}$ production [15]:

1. Flavor Creation (direct production): two gluons from the beam particles interact through hard scattering resulting in two outgoing b quarks (gluon version). At the same lowest order, a quark and antiquark form a $b\bar{b}$ pair through $q\bar{q}$ annihilation.

2. Flavor Excitation: one b quark from the sea of one of the beam particles is scattered from a parton from another beam particle.

3. Gluon Splitting: the $b\bar{b}$ quarks are created from a gluon after the hard scattering.

Once the $b - \bar{b}$ quark pairs are produced, they will radiate gluons through the strong interaction. This process can be calculated perturbatively, because of the high virtuality scale $Q^2 \gg \Lambda_{QCD}^2$ indicating $\alpha_s \ll 1$. When the b and $\bar{b}$ quarks separate, the energy scale will decrease and the color interaction between the quarks will become stronger. At some point, the increasing potential energy between the quarks will be strong enough to create another $q\bar{q}$ pair from the vacuum. This process will repeat until the system creates clusters of quarks and gluons with zero color and low internal momentum. A property of the strong interaction called color confinement binds the quarks to color-neutral hadronic final states. This process is known as hadronization. The probabilities for a b quark to hadronize into a B^-, B_d^0, B_s^0 or b-baryons define the fragmentation fractions f_u, f_d, f_s and $f_{b-baryon}$. The
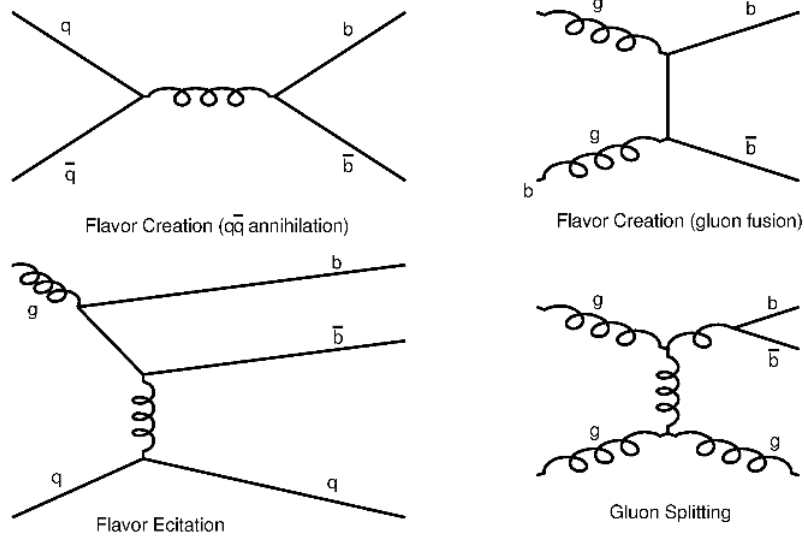
Figure 2.6: $b - \bar{b}$ *production in a hadronic collider*

contribution from excited B hadrons decaying into final states containing a u, d, s or a b-baryon is included in this definition. The latest combined result from the Heavy Flavor Averaging Group (HFAG) is [12]

$$f_u = f_d = 0.401 \pm 0.010, \quad f_s = 0.106 \pm 0.013, \quad f_{b-baryon} = 0.092 \pm 0.018 \tag{2.38}$$

The B hadron production at the Tevatron is copious due to its large $b\bar{b}$ production cross section. QCD calculations determine the single B hadron cross section as [16]

$$\sigma_{|y|<0.6} = 16.8^{+7.0}_{-5.0}\mu b \tag{2.39}$$

CDF measured in 2005 the b production cross section as [17]

$$\sigma[p\bar{p} \rightarrow H_b X, |y| < 0.6] = 17.6 \pm 0.4(stat))^{+2.5}_{-2.3}(syst)\mu b \tag{2.40}$$

which agrees well with the theoretical prediction.

2.6   The B mesons decays

The electroweak decays of B mesons can be distinguished in: leptonic, semileptonic and hadronic decays, in relation to the type of daughters particles. The $B_s \rightarrow \phi\phi$ is an hadronic decay so we will focus on these decays. In general there are two topologies of Feynmann diagram contributing to non-leptonic decay, the tree and a penguin (this can be gluonic or electroweak) as shown in Figure 2.7.
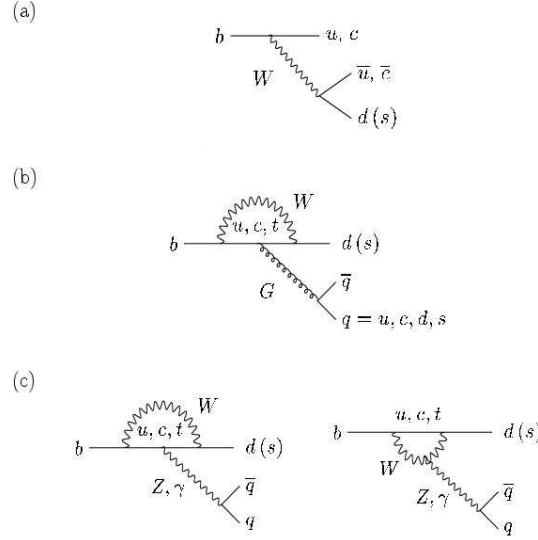

Figure 2.7: *Feynman diagrams of different topologies for the non-leptonic decays of B mesons: tree (a), QCD penguin (b) and electroweak penguin (c).*

To calculate the Branching Ratio and the amplitudes of hadronic decays an effective Hamiltonian at low energy, H_{eff}, is used which can be written using techniques such as *Operator Product Expansion* (OPE) [18] from which we get for example:

$$< f|H_{eff}|i >= \frac{G_F}{\sqrt{2}}\lambda_{CKM} \sum_k C_k(\mu) < f|Q_k|i > \qquad (2.41)$$

where λ_{CKM} is a V_{CKM} matrix element, G_F is the Fermi constant, μ is the renormalization scale and C_k are the Wilson coefficients.

This allow us to decouple the perturbative contributions C_k, from the non-perturbative $< f|Q_k|i >$ (hadronic matrix elements). The Q_k are local operators derived from QCD and electroweak interactions.

In order to evaluate the matrix elements of the non perturbative terms, there are several phenomenological approaches (SCET, QCDp, QCDf etc) which

19

are explained in detail in [19]. In the QCDf framework, explained in [18] we have that the value of the BR for the decay $B_s \rightarrow \phi\phi$ is $= 1.31 \cdot 10^{-5}$.

2.7 Manifestation of new physics

The concept of low-energy effective Hamiltonian allows us to develop a phenomenological treatment of possible manifestations of new physics in B meson decays. These are two-fold.

First, the new physics may modify the action of Standard Model operators through new, short-distance terms depending on new physics parameters, e. g., masses of charginos, squarks, etc. Virtual new physics particles may participate in second-order diagrams (box or penguin topologies) thereby being integrated out as it happens in the SM for the top quark and the W boson in similar loop diagrams. As a consequence, the Wilson coefficient become:

$$C_k \rightarrow C_k^{SM} + C_k^{NP}, \tag{2.42}$$

where C_k^{SM} and C_k^{NP} are the Wilson coefficients associated to the Standard Model and new physics amplitudes, respectively. The new physics-related C_k coefficients may carry new CP-violating phases not related to the CKM matrix.

Secondly, new physics may enlarge the operator basis:

$$\{Q_k\} \rightarrow \{Q_k^{SM}, Q_l^{NP}\}, \tag{2.43}$$

thus enhancing the role of operators otherwise absent or suppressed in the Standard Model. In this case, generally, new sources for flavor or CP violation arise. The opportunity of measuring a relatively small set of CKM-related observables using a rich variety of observables associated to many distinct processes, some of which proceeding through very different dynamics, provides access to the detection of new physics: comparison between values of the same quantities measured through different processes, and experimental verification of the multiple correlations between CKM-parameters prescribed by the Standard Model, are sensitive to the possible virtual contributions of non-Standard Model particles in a large fraction of new physics models. A straightforward evidence for new physics would be obtained, for instance, if decay amplitudes abnormally larger than expected were observed, indicating presence of non-Standard Model particles in penguin, box diagrams, or even tree diagrams.

2.8 The $B_s \rightarrow \phi\phi$ decay

The $B_s \rightarrow \phi\phi$ decay is a a charmless decay of the B_s into two vector mesons characterized by a quark transition $b \rightarrow s$ dominated by a penguin diagram

20

(Figure 2.8).
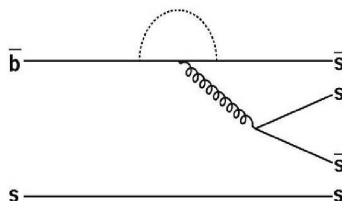

Figure 2.8: *Feynman diagram for a $B_s \to \phi\phi$ penguin decay.*

The polarization of a vector meson is defined, in analogy to that of electromagnetic radiation, with the components of a vector field in a defined reference frame and can be evaluated measuring the angular distributions of final states.

In general, the decays $B \to$ Vector Vector mesons ($B \to VV$) go into three different polarization states, defined by the type of polarization of the system (two longitudinal and one transverse states). Within the Standard Model, the decay widths of transverse processes are suppressed by a factor of m_b/m_t compared to the longitudinal ones. It is expected from theoretical calculations that the transverse polarization should very small [20], but measurements done in the $B_d \to \phi K^*$ [21] and $B_d \to \rho K^*$ shows the opposite [22]. This discrepancy, known as polarization puzzle [23], could be due to imperfect theoretical modeling of the phenomenon (and in particular to the calculation methodology used to simplify perturbative calculations QCD), or to the presence of new physics in penguin diagram, or to the effects of non perturbative rescattering as explained in [20].

For this reason a measurement of the polarization of the decay $B_s \to \phi\phi$ would be very interesting especially compared with the measurement obtained for the $B_d \to \phi K^*$, a very similar topological decay.

Another important peculiarities of the $B_s \to \phi\phi$ decay is that it proceeds through a transition dominated by penguin diagrams, where possible new physics effects due to the contribution of a new particle in the Feynman diagram loop can manifest themselves [24], [25].

In the recent years, some deviations from Standard Model predictions, especially in decays involving $b \to s$ quarks transitions, have been observed. Some theoretical speculations have been provided in order to establish whether these deviations can be an indication of the presence of new physics. Clearly,

an improvement of the currently available measurements and a throughout investigation of this kind of decays are needed.

2.9 Looking for New Physics using the $B_s \to \phi\phi$

From an experimental point of view, the study of the $B_s \to \phi\phi$ channel is a very interesting place to look for evidence of New Physics:

- in the determination of Branching Ratio (BR), if it appears to be very different from the theory estimation;

- in the comparison of amplitudes of polarization measurements with those of the $B_d \to \phi K^*$;

- in the determination of $\Delta\Gamma_s$ of mixing if it is different from that obtained from the $B_s \to J/\psi\phi$;

- in the determination of CKM parameters and studies of CP violation.

Chapter 3

The TeVatron Collider and the CDFII experiment

The Collider Detector at Fermilab (CDFII) is one of the two main experiments at the Tevatron Collider of the Fermi National Accelerator Laboratory (Fermilab) in U.S.A. The Tevatron Collider is currently the world highest energy accelerator system and provides proton-antiproton collisions at a center-of-mass energy of 1.96 TeV.

In this chapter, the production and acceleration of particle and anti-particle beams will be described (see also [28] and [29])and a description of the CDFII [30] experiment is given, with a focus on the detector elements which are relevant for B physics.

3.1   The TeVatron Collider

The Tevatron is the last and highest energy stage of the large accelerator system at Fermilab. The first $p\overline{p}$ collisions have been produced in 1986. Since then, several extensive upgrades have been undertaken leading to major improvements of the overall performances.

The Tevatron is a circular superconducting synchrotron of 1 km radius. While operating in collider mode, the Tevatron collides counter-rotating bunches of protons and antiprotons every 396 ns in two interaction regions along the ring: B0, which is the site of the CDFII experiment, and D0, where the D0 experiment is located. Radio-frequency cavities (RF) are used to accelerate the particles.

A schematic drawing of the Fermilab Accelerator complex is shown in Fig.3.1.
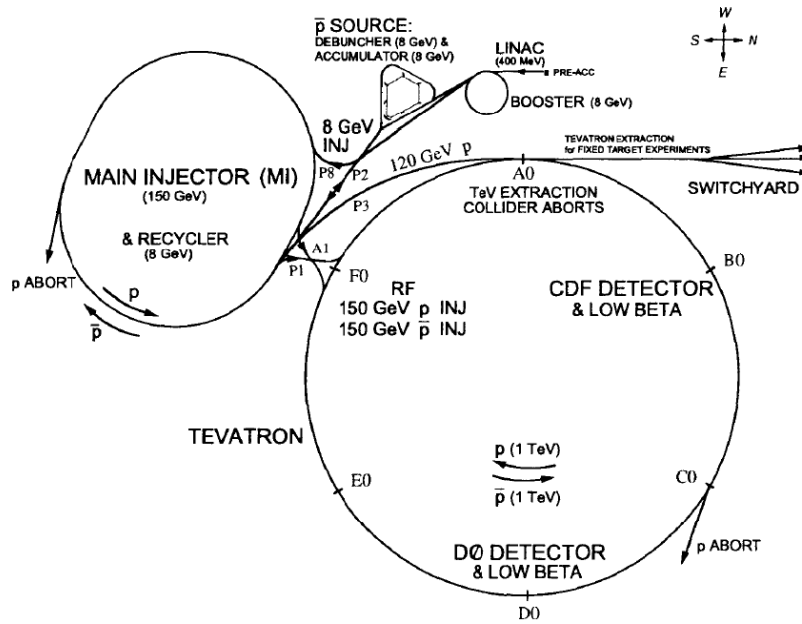
Figure 3.1: *View of the accelerators chain*

3.1.1 Proton and Antiproton Production

The first stage in the acceleration of protons is a commercial Cockcroft-Walton accelerator, which boost to 750 KeV the H$^-$ ions produced by ionization of gaseous hydrogen. The ions are then injected into a 150 m long linear accelerator ("Linac") which increases their energy to 400 MeV. The H$^-$ pass through a carbon foil and this process strips the two electrons from H$^-$ obtaining the protons which are then injected into the "Booster". The Booster is a circular synchrotron with 18 RF cavities distributed around a ring with a 75 m radius. The 201 MHz frequencies of the bunches from Linac do not match the 37.8 MHz frequencies of the RF cavities in the Booster. After the beam has been injected, the protons eventually come into phase with the cavities, and a new 37.8 MHz bunch structure is formed and accelerated to 8 GeV. The protons are then transferred to the "Main Injector" which brings their energies to 150 GeV. The Main Injector is a circular synchrotron with 18 accelerating RF cavities and a circumference of almost 2 miles (completed in 1999), approximately half the circumference of the Tevatron. The final step of the process is the transfer to the Tevatron, a synchrotron which employs superconducting quadrupole magnets with Nb-Ti alloy filaments embedded in copper as magnet coils. The magnetic field of 5.7 T keeps the protons on an approximately circular orbit while they reach the final energy of 980 GeV.

To produce antiprotons, some of the 120 GeV proton bunches of the Main

Injector are slammed into a rotating 7 cm thick nickel or copper target. Antiprotons are produced by the following reaction:

$$p + \binom{n}{p} \qquad \rightarrow \qquad p + p + \binom{n}{p} + \bar{p} \tag{3.1}$$

Before colliding, the protons bunches are rotated by $90°$ in phase space, so that they have a large spread in energy but a small lag in arrival time at the target. A spatially broad beam of particles is produced and then focused using a cylindrical Lithium Lens. This beam, which has a bunch structure similar to the incident proton beam, is passed through a pulsed dipole magnet. The magnetic field selects the negatively charged antiprotons with about 8 GeV of kinetic energy. About 20 antiprotons are produced for every 100 protons on target and then stored into the "Debuncher". The Debuncher is a triangular-shaped synchrotron with mean radius of 90 m. The beam is stochastically cooled [31] and then transferred to the "Accumulator", which is another triangular-shaped synchrotron with a mean radius of 75 m. The Accumulator is a storage ring for the antiprotons; they are stored at an energy of 8 GeV and cooled until needed. The antiprotons are then sent into the Main Injector, where they are accelerated to 150 GeV. Finally, the antiprotons are transferred to the Tevatron, where 36 previously injected bunches of protons are already circulating in opposite direction. Since 2004, an additional Recycler Ring has been added in the same tunnel of the Main Injector and provides additional storage and cooling of the antiprotons.

3.1.2   The Collision and the Luminosity

In order to produce collisions, 36 bunches of protons are injected into Tevatron. Twelve bunches, each separated by 396 ns are grouped together into three trains of bunches. The trains have a larger separation of approximately $2.5\mu sec$ and the gaps provide enough space to insert the next 36 bunches of antiprotons without disturbing the protons. The bunch structure is illustrated in Fig.3.2.

 The antiproton bunch pattern is the same of the protons; $\bar{p}$ circulate in the Tevatron in the opposite direction of the p and within the same magnet and vacuum systems. The energy of p and $\bar{p}$ is increased in about 10 seconds from 150 to 980 GeV. Special quadrupole magnets (low-β squeezers), located close to the CDFII and D0 experiments along the beam pipe, "squeeze" the beam in order to maximize luminosity inside the detectors. A roughly Gaussian distribution of the interaction region along the beam axis is achieved ($\sigma_z \simeq 30$ cm). The transverse shape of the interaction region has an almost circular spatial distribution with a diameter of 30 μm.

The Tevatron performances can be evaluated in terms of two parameters: the center-of-mass energy, $\sqrt{s}$, and the instantaneous luminosity, $\mathcal{L}$.

$\sqrt{s}$ defines the accessible phase space for the production of particles in the
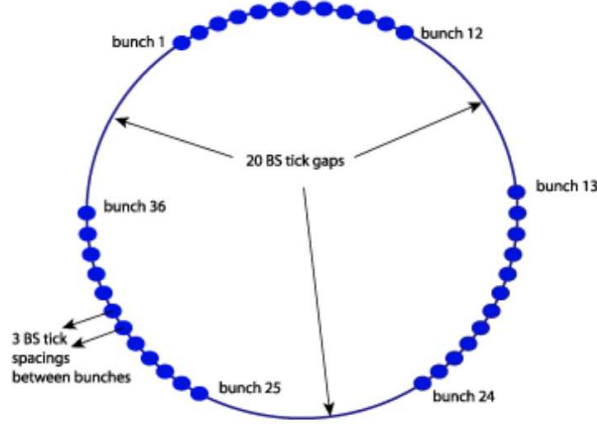
Figure 3.2: *Bunch structure of the Tevatron (BS = beam sync ticks = 132ns).*

final states and $\mathcal{L}$ relates the production rate of a given process and its cross section : rate [events s^{-1}]= $\mathcal{L} \times \sigma$. With ideal head-on $p\bar{p}$ collision, the instantaneous luminosity is given by:

$$\mathcal{L} = \frac{fBN_pN_{\bar{p}}}{2\pi(\sigma_p^2 + \sigma_{\bar{p}}^2)}F(\sigma_l/\beta^*) \tag{3.2}$$

where f is the revolution frequency, B is the number of bunches in each beam, $N_p(N_{\bar{p}})$ is the average number of protons (antiprotons) in each bunch, $\sigma_p(\sigma_{\bar{p}})$ is the proton (antiproton) transverse beam size at the interaction point, and F is a form factor which depends on the ratio of the bunch longitudinal length, σ_l, to the "β^* function" at the interaction point (β^* is an accelerator parameter that depends on the beam optics).

Due to beam-beam interactions and collisions, the instantaneous luminosity decreases exponentially over time. The beam is usually dumped intentionally after 15-20 hours of collisions.

3.2 The CDFII Experiment

The CDFII detector is a large multi-purpose solenoidal magnetic spectrometer. A full description of the detector can be found in the CDFII Technical Design Report [30]. The current detector is the result of a major upgrade which began in 1995 and the start date of the CDFII experiment was June 2001. In this thesis the acronym CDF is often used in place of CDFII.

In this section a brief overview of the detector will be given followed by a description of the subsystems, with more emphasis given to the ones more relevant for B physics, namely the tracking system and the trigger.

26

3.2.1 Detector Overview and Coordinate System

A cut-away view of the CDF detector is shown in Fig.3.3. The detector consists of various tracking systems immersed in a solenoidal magnetic field,
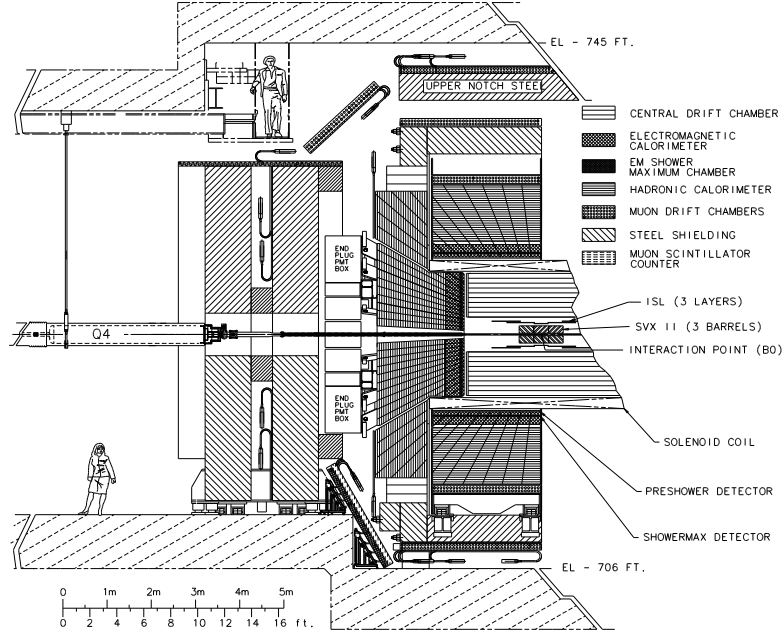

Figure 3.3: *Cut-away view of the CDF detector.*

positioned within the electromagnetic (EM) and hadronic calorimeters, and a muon detection systems which includes several drift chambers and steel shielding. The momentum and impact parameter of charged particles can be measured by the tracking systems, which are not sensitive to the neutral particles. The EM calorimeter measures the energy of photons and electrons and the energy of hadrons is measured in the hadronic calorimeter. Neutrinos are not detected but can be identified indirectly through the transverse energy imbalance as measured by the calorimeters (missing transverse energy). The muons, which are minimum ionizing particles, will be detected by the outer muon detector systems.

CDF adopts a right-handed Cartesian coordinate system with origin at the center of the detector. The z-axis is defined to be parallel to the nominal beamline and in the proton direction, while x-axis is defined as the horizontal axis pointing outwards from the Tevatron ring center, as shown in Fig. 3.4. Due to the symmetry of the detector, a cylindrical system (r, ϕ, z) coordinate system is defined too. The azimuthal angle ϕ is defined relative to the positive x-axis. The polar angle θ is often used as well and is defined relative to the positive z-axis. The direction parallel to the z-axis is usually called "longitudinal" and the plane perpendicular to z-axis is called "transverse" (the
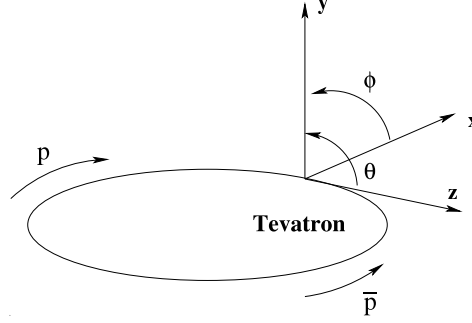
27

Figure 3.4: *CDF coordinate system*

$(x, y) \equiv (r, \phi)$ plane). In hadron collisions, a particularly useful kinematic variable is the rapidity, defined as

$$Y = \frac{1}{2} ln \left[\frac{E + p \cdot cos\theta}{E - p \cdot cos\theta} \right] \tag{3.3}$$

where $(E, \vec{p})$ is the energy-momentum four-vector of the particle. This variable has the virtue of invariance to z boosts. In the ultra-relativistic limit, the rapidity Y is closely approximated by the pseudo-rapidity, related only to the track angle according to

$$\eta = -ln \left[tan(\theta/2) \right] \tag{3.4}$$

One can show that $Y \rightarrow \eta + O(m^2/p^2)$. Other convenient variables include the transverse component of the momentum (p_T), the "transverse energy" E_T , and the approximately Lorentz-invariant angular distance ΔR, defined as:

$$p_T \equiv p sin\theta, \qquad E_T \equiv E sin\theta, \qquad \Delta R \equiv \sqrt{\eta^2 + \phi^2} \tag{3.5}$$

3.2.2 Tracking System

The CDF tracking system is an integrated system including silicon tracking detectors and a large outer drift-chamber [32]. Together, they provide three-dimensional particle tracking with excellent transverse momentum resolution and precise impact parameter measurement. All the tracking systems up to 1.4 m are immersed in a 1.4 T magnetic field which curves the charged particle, providing momentum information. As shown in Fig.3.5, the inner silicon detector consists of three sub-detectors that extend from radius of r = 1.35 cm to r = 28 cm and cover the range range of $|\eta| < 2$. Surrounding the silicon detector is the Central Outer Tracker (COT) which covers the region of radius from 44 cm to 132 cm and of 310 cm in length along the z direction.

The accurate measurement of tracks close to the beamline is essential for
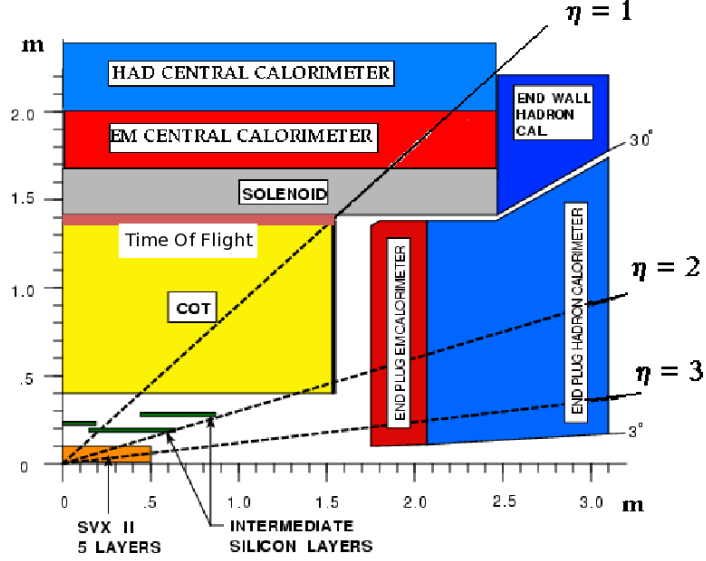
28

Figure 3.5: *One quadrant of the CDF detector tracking layout.*

CDF physics analysis including B physics. The silicon detectors used at CDF were introduced into the experiment for the first time in Run I and significantly upgraded for Run II. Silicon detectors close to the beamline are ideal for precision impact parameter measurement, thanks to their excellent spatial resolution. The width of each silicon strip is about $60\mu m$, which gives a resolution of $60\mu m/\sqrt{12} \sim 17\mu m$. The main silicon detector is the Silicon Vertex Detector II (SVXII). The outer extension, the Intermediate Silicon Layers (ISL), links the tracks reconstructed in the chamber and hits detected in the SVXII, and helps in extending track reconstruction for $1 < |\eta| < 2$ where the COT coverage is marginal. The inner extension, Layer 00 (L00), is a light-weight silicon layer placed on the beam-pipe. It recovers the resolution degradation of the reconstructed vertex position due to multiple scattering particularly in the SVXII read-out electronics and cooling systems.

Layer 00

The innermost layer of the silicon detector at a radius of 1.35 cm consists of one layer of single sided AC-coupled silicon sensors which cover the beryllium beam pipe over 80 cm longitudinal distance [33]. The 7.85 cm long silicon sensors can be biased to very high voltages allowing a good signal-to-noise ratio. The strips are parallel to the beam axis giving the first sampling of a track in the (r,ϕ) plane. Signals from more than 13000 channels are fed via special optical fiber cables placed in a region separated from sensors and less exposed to the radiation. A flux of gas through tiny aluminum pipes installed between the sensor and the beam pipe keeps the operation temper-

29

ature around 0 $C°$. The pressure of the gas is below atmospheric pressure to avoid leaks of fluid in case of damaged cooling pipe.

Silicon Vertex Detector II (SVXII)

The Silicon Vertex Detector is built in three cylindrical barrels, each 29 cm long and segmented into twelve wedges in the ϕ direction (see Fig.3.6 and 3.7). Each barrel is made of five concentric layers of double-sided silicon
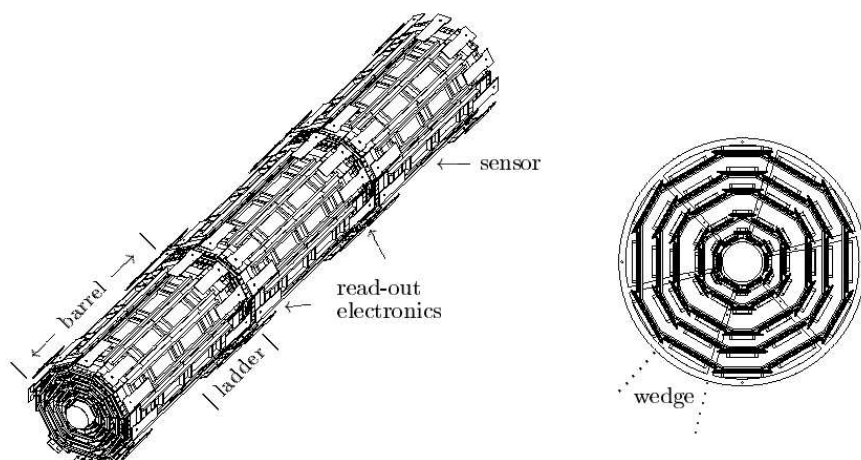

Figure 3.6: *SVXII: view of the three barrels (left) and the $x - y$ plane section (right).*

sensors at radii from 2.5 cm to 10.6 cm. Each layer of a barrel is comprised by two independent readout units, called "ladders". Each ladder consists of two double sided rectangular 7.5 cm long sensors and the "hybrid", a multilayer board containing the frond end electronics, biasing circuits and fanouts. The ladders of each barrel are longitudinally juxtaposed head-to-head within a barrel's layer to leave the two hybrids at the two outside extremities of the barrel. The AC-coupled silicon sensors consist of microstrips implanted on a 300 μm bulk.

Bias is applied through integrated polysilicon resistors. Three types of strip orientations are used: $r - \phi$ (axial) strips oriented parallel to the beam axis, small angle stereo (SAS) strips tilted by 1.2° with respect to the beam axis and the 90° strips which lie in the transverse plane. All of the five layers have axial strips on one side, three of the other sides have 90° strips and two have SAS strips. The measured average signal-to-noise ratio $S/N \geq 10$, with a single hit efficiency greater than 99%.

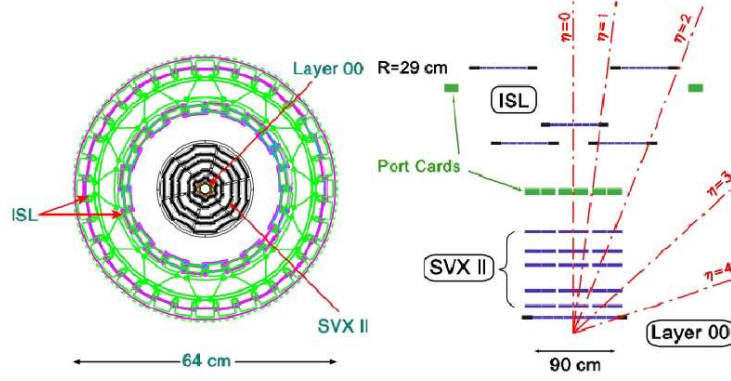A water-glycol system cools the whole SVXII at a temperature of about

30

Figure 3.7: *Silicon Detectors:: $x - y$ and $z - y$ plane views.*

10-15 $C°$.

Intermediate Silicon Layers (ISL)

The Intermediate Silicon Layers detector [34] is a silicon tracker placed at intermediate radial distance between the SVXII and the drift chamber (see Fig.3.8. It has a cylindrical geometry and it is segmented into twelve wedges like SVXII. It has a single layer of silicon in the central region at radius of 22 cm and two layers of silicon in the forward region at radius of 20 cm and 28 cm. ISL employs double sided AC-coupled 300 μm thick sensors; each sensor has axial strips on one side and SAS strips on the other.
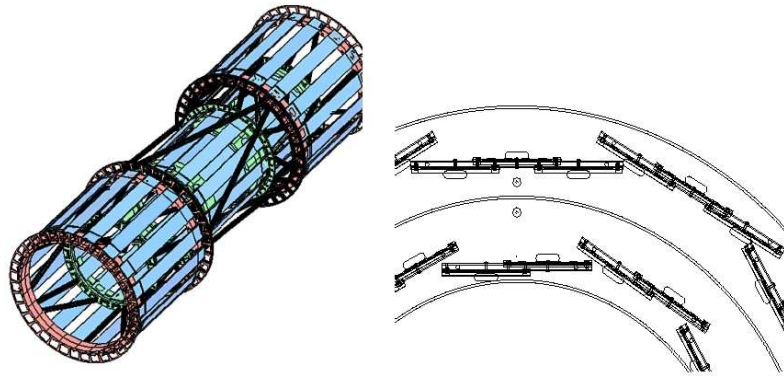
Figure 3.8: *ISL*

Central Outer Tracker (COT)

The Central Outer Tracker is a cylindrical open-cell drift chamber and its active volume spans from 43.4 to 132.3 cm in radius and 310 cm in the axial direction [35]. The COT contains 96 sense wire layers in the radial direction which are arranged into eight superlayers as shown in Fig.3.9. The maximum drift distance is approximately the same for all superlayers. Superlayers 1,
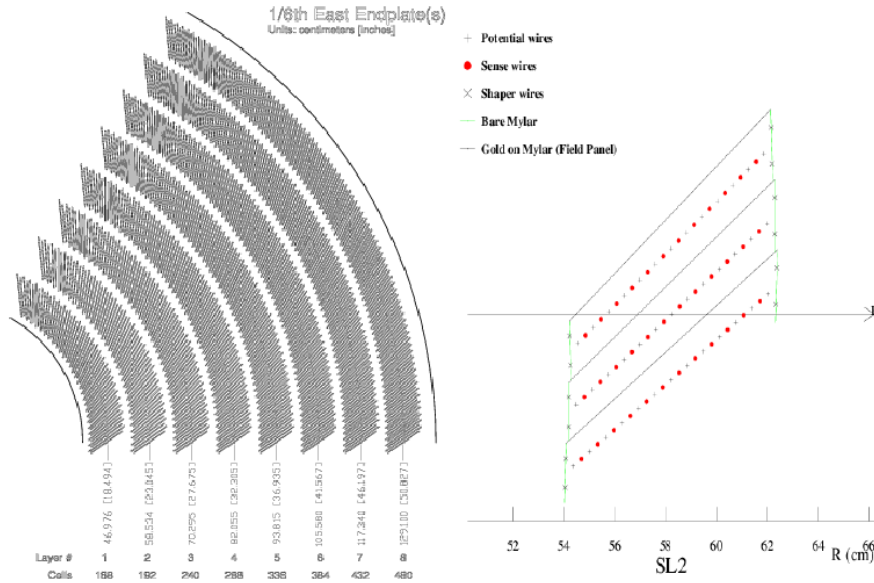
Figure 3.9: *COT: $x - y$ plane section (left) and transverse view of 3 cells (right).*

3, 5, 7 have the sense wires oriented parallel to the beam axis ("axial") to measure hit positions in $r - \phi$ plane; the other superlayers have the sense wires tilted $+3°$ or $-3°$ with respect to the beam axis ("stereo"). Combined readout of axial and stereo superlayers give r-z position information. Each superlayer is divided in ϕ into open drift cells. Fig.3.9 (right) shows the transverse view of 3 cells. Each cell has 12 sense wires and 17 potential wires that are closed by the Mylar gold cathodes on either sides along the azimuthal direction. The potential wires help to shape the electric field near the sense wires.

The COT is filled with a 50:50 Argon-Ethane gas mixture which functions as an active medium. Charged particles that travel through the chamber will leave a trail of ionization in the gas. Electrons drift, in crossed electric and magnetic fields, toward the sense wires at a Lorentz angle of $35°$. For this reason the cells in each superlayer are not aligned along $\hat{r}$ but a $35°$ azimuthal tilt is provided instead. The tilt also helps the high p_T (radial)

32

tracks to go through the full range of the drift distance in each superlayer. Electrons travel with a drift speed around 100 $\mu m/ns$, so the maximum drift time is about 100 ns for a distance of 1 cm between wires. The drift time is small compared with the inter-bunch spacing time of 396 ns to provide enough time for processing data from COT.

Tracking Performances

The trajectory of a charged particle which moves in a homogeneous magnetic field ($B = (0, 0, -1)$) is described by a helix. The projection of the helix on the $r - \phi$ plane is a circle. To parametrize this helix uniquely, five parameters are used : $C, cot\theta, d_0, \phi_0$ and z_0. C is the signed curvature of the circle defined as $C = \frac{1}{2\rho Q}$, where ρ is the radius of the circle and Q is sign of the charge. So the positive charged tracks curve counter-clockwise in the $r - \phi$ plane when looking in the negative z direction, while negative charge tracks curve the other way. θ is the polar angle of the particle momentum at the point of its closest approach to the z axis. $cot\theta$ is the helix pitch, which is related to the longitudinal component of the momentum: $p_Z = p_T cot\theta$. ϕ_0 is the azimuthal angle of the particle at the point of closest approach to the z axis. z_0 is the z coordinate of the point of closest approach to the z axis. d_0 is the signed impact parameter, i.e. the distance of closest approach to the z axis defined as $d_0 = Q\sqrt{x_0^2 + y_0^2} - \rho$, where (x_0, y_0) is the center of the helix circle. The transverse momentum of the track can be calculated from the equation $p_T = Q\frac{1.49896*10^{-4}B_{magnet}}{C}$, where the unit of the magnetic field, B_{magnet}, is Gauss.

Initially, track reconstruction is performed using the COT information only. The algorithm looks for a circular path in the axial superlayers of the COT. Four or more hits in each axial superlayer are used to form a straight line or "segments". Then two approaches can be used for finding tracks. One way is to perform a χ^2-fit to all hits belonging to matching segments among different super-layers. The other way is to constrain the circular fit to the beamline; then hits which are consistent with this path are added. Once a circular track in the $r - \phi$ plane is found, segments in the stereo superlayers can be added in a three dimensional track fit. Once a track is constructed in the COT, it is extrapolated into the SVXII detector. A three dimensional "road map" is formed based on the estimated errors on the track parameters. Starting from the outermost layer and working inward, silicon clusters found along the road are added to the track. For every added cluster, the track fit is updated, modifying the estimated track parameters and their errors, and generally narrowing the search 'road'. In the first pass, only r-ϕ clusters are used. Then stereo clusters are added. If there is more than one track with different combinations of SVXII hits associated with the same COT track, the track with the maximum number of SVXII hits is chosen. The transverse momentum resolution of the reconstructed track is very good.

33

The COT alone can provide a resolution of $\sigma_{p_T}/p_T^2 \approx 0.15\%(GeV/c)^{-1}$ and $\sigma_{d_0} \approx 250 \ \mu m$. With SVXII information added a great improvement on the d_0 resolution is achieved: $\sigma_{d_0} \approx 20 \ \mu m$.

3.2.3 Particle Identification Systems

Two sub-detectors at CDF provide information for particle identification: COT and Time of Flight detector.

Particle identification in the COT

The first system is based on ionization energy loss dE/dx measured in the COT. When a charged particle traverses the gas volume of the drift chamber, it leaves a trail of ionization along its path. The energy loss is proportional to the amount of ionization. The average energy loss per unit length for relativistic charge particles (heavier than the electron) can be described by the Bethe-Bloch equation:

$$\frac{dE}{dx} = \frac{4\pi Ne^4}{mc^2\beta^2} z^2 (ln\frac{2mc^2\beta^2\gamma^2}{I} - \beta^2 - \frac{\delta(\beta)}{2}) \tag{3.6}$$

where N is the electron density in the material, m (e) is the electron mass (charge), z is the incident particle charge, I is the mean excitation energy of the material atoms, β= v/c and v is the particle velocity, $\gamma^2 = 1/(1 - \beta^2)$, and $\delta(\beta)$ is a correction needed for the density effect at high β. According to this equation, for a given drift chamber, dE/dx only depends on particle velocity, so it can be used to distinguish particles of different mass when combined with momentum measurement.

The Time Of Flight Detector

The Time of Flight (TOF) detector was added in 2001 to improve the particle identification capability. It is a cylindrical array made of 216 bars of Bicron BC-408 scintillator with dimensions $4 \times 4 \times 279 \ cm^3$ located between the external surface of the COT and the cryostat of the super-conducting solenoid at a mean radius of 140 cm. The pseudo-rapidity coverage of the system is about $|\eta| < 1$. Both ends of each bar collect the light pulse using photomultiplier tubes and measure accurately the timing of the two pulses. The time of flight t is obtained by measuring the time of arrival of a particle at the scintillator with respect to the collision time. With momentum information from the track, the particle mass m can be determined by:

$$m = \frac{p}{c}\sqrt{\frac{c^2t^2}{L^2} - 1} \tag{3.7}$$

where L is the path length measured by the tracking system. With a time-of-flight resolution around 110 ps, the TOF system can provide at least

34

a two standard deviation separation between charged kaons and charged pions for momentum p < 1.6 GeV, an information complementary to the dE/dx measurement from COT. A separation power plot for TOF is shown in Fig.3.10 together with the dE/dx separation power superimposed.
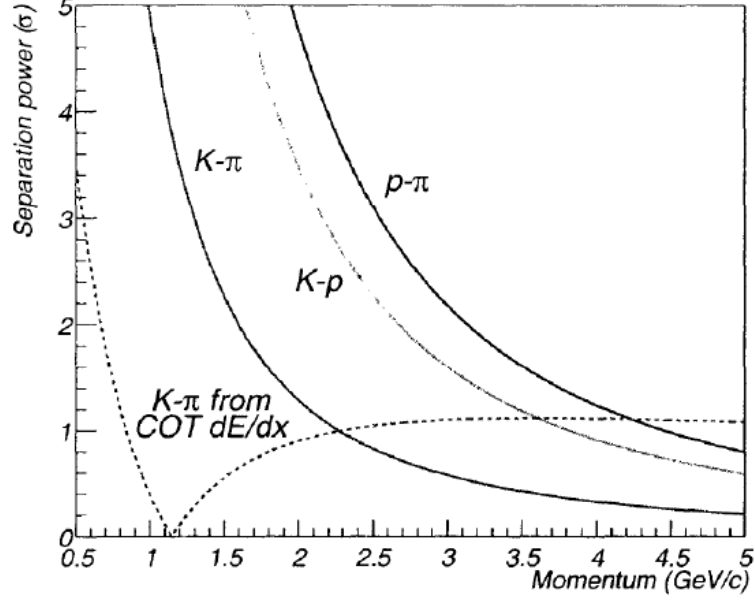

Figure 3.10: *Separation power of TOF for different particles at CDF, with dE/dx separation power for kaon and pion from COT superimposed.*

3.2.4   Calorimeter System

The CDF calorimeter system is located outside the solenoid and composed of electromagnetic (EM) and hadronic scintillator sampling calorimeters. As shown in Fig.3.11, the calorimetry includes several different systems: Central Electromagnetic (CEM), Central Hadron (CHA) and Wall Hadron (WHA) [36], Plug Electromagnetic (PEM) and Plug Hadron (PHA). Together they cover the pseudo-rapidity region $|\eta| < 3.6$. They are segmented in solid angle around the CDF detector nominal center and organized in projective towers. Each tower comprises two compartment: the innermost is the electromagnetic calorimeter followed by the hadronic calorimeter. The main task of the calorimeter system is the measurement of energy deposition of photons, electrons and hadrons. The basic structure of the calorimeters is alternating layers of passive absorbers and plastic scintillators. CEM and PEM use lead sheets for absorber material, while CHA and WHA use steel, and the PHA uses iron. Particles with transverse momentum greater than about 350 MeV and $|\eta| < 1$ can reach the central calorimeters, where they will undergo en-

35
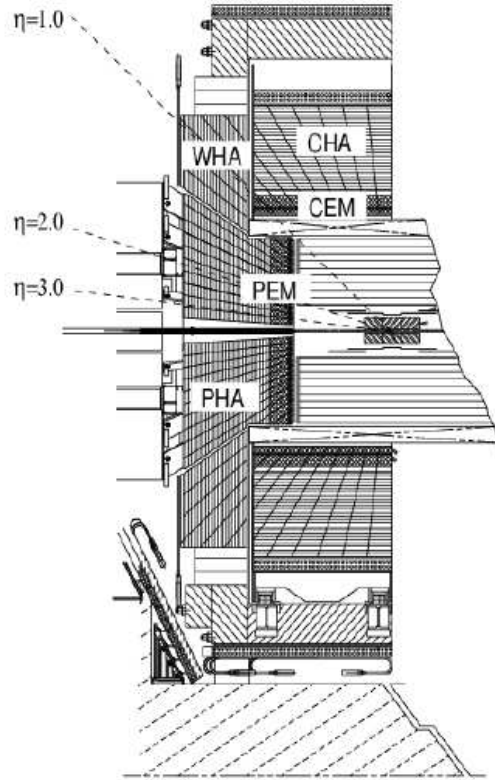
Figure 3.11: *Overview of the different calorimeters.*

ergy loss, striking the absorber materials and producing daughter particles which interact in a cascade process, giving rise to a 'shower' of particles. The showers propagate through many layers of absorbers and generate a detectable signal before they exhaust their energy. The sum of the signals collected by all the sampling active layers is proportional to the energy of the incident particle.

3.2.5 The Muon System

Muons are over 200 times more massive than electrons, so bremsstrahlung radiation, inversely proportional to the mass squared of the incident particle, is suppressed by a factor of $4 \cdot 10^4$ with respect to electrons. Muons do not interact via strong interaction with nuclei in matter either. Therefore, a muon with enough energy will pass through the calorimeter systems

releasing only a small amount of its energy. At CDF the minimum muon energy required to reach the muon detectors, placed radially outside of the calorimeters, is 1.4 GeV. In addition to the calorimeters, steel absorbers are placed upstream of the muon systems to reduce punch-through hadrons. The CDF muon system consists of 4 independent subsystems of scintillators and drift chambers [37]: Central Muon (CMU), Central Muon uPgrade (CMP), Central Muon eXtension (CMX) and Intermediate MUon (IMU). Fig.3.12
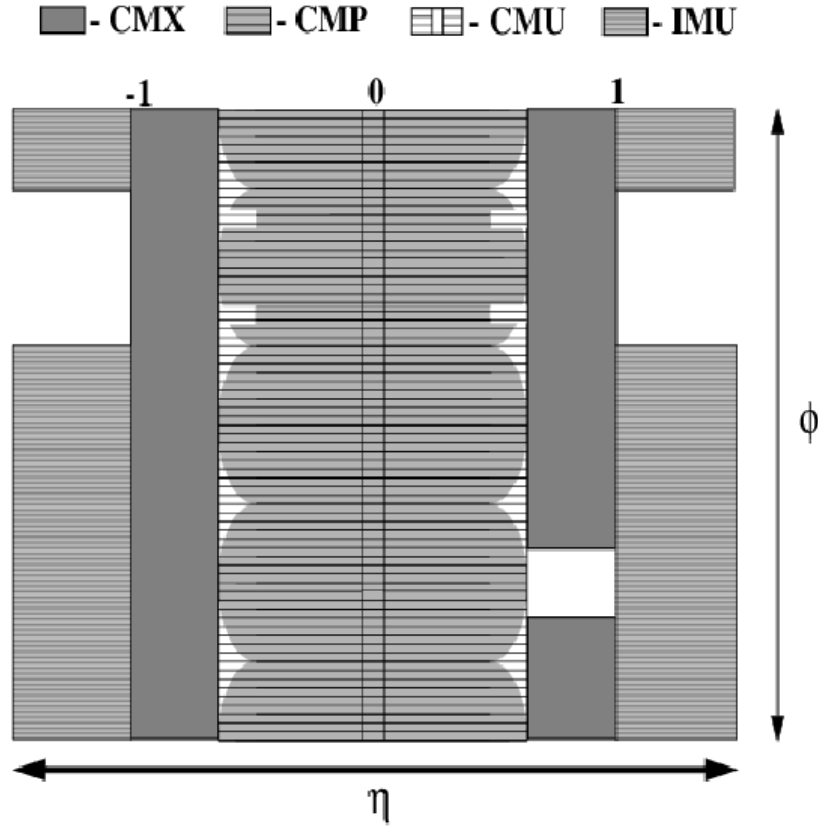
Figure 3.12: *Muon detectors coverage in the* $\eta - \phi$ *plane.*

shows the coverage of the muon systems. The muon chambers employ sense wires parallel to the beamline and are filled with a 50:50 Argon-Ethane gas mixture. Muon candidates identified as track segments in the chambers are called muon stubs. A muon stub is matched with a track measured by the COT to reduce background from noise in the electronics and punch-through hadrons.

CMU

The Central MUon detector (CMU) is located outside of the hadronic calorimeter at a radius of 347 cm from the beamline with coverage $|\eta| < 0.6$. The CMU is segmented into 24 wedges of 15° , but only 12.6° of each wedge is active, resulting in an overall azimuthal acceptance of 84%. Each wedge is further segmented into three 4.2° modules each containing four layers of four drift cells.

CMP

The Central Muon uPgrade (CMP) is a second set of muon drift chambers outside of CMU with an additional 60 cm of steel absorbers between them. The material further reduces the probability of hadronic punch-through to the CMP. Muons need a transverse momentum of about 2.2 GeV to reach the CMP. The CMP system is arranged in a box shape of similar acceptance as the CMU and conventionally serves as a confirmation of CMU for higher momentum muons. A layer of scintillation counters (CSP) is mounted on the outer surfaces of the CMP. The CMP and CMU have a large overlap in coverage and are often used together. CMP helps to cover CMU ϕ gaps and the CMU covers the CMP η gaps. Muon candidates which have both CMU and CMP stubs are the least contaminated by fake muons.

CMX

The Central Muon eXtension (CMX) consists of drift tubes and scintillation counters (CSX) assembled in conically arranged sections. The CMX extends the pseudo-rapidity coverage to $0.6 < |\eta| < 1.0$. There are 8 layers of drift chambers in total with a small stereo angle between layers.

IMU

The Intermediate MUon (IMU) extends the pseudo-rapidity coverage even further to $1.0 < |\eta| < 1.5$. The IMU is mounted on the toroid magnets which provide shielding and consists of Barrel MUon chambers (BMU), Barrel (BSU) and Toroid (TSU) scintillation counters.

3.2.6   The Trigger System

The overwhelming background in a hadron collider environment requires a highly performing trigger system, able to extract the tiny fraction of interesting events. For example, the total $b\bar{b}$ cross section over the total inelastic cross section is of order 1/1000. The Tevatron is running at a luminosity around $3 \cdot 10^{32} s^{-1} cm^{-2}$, and there are millions of interactions per second to be compare with the maximum capacity for CDF to record events of about

150 Hz. In order to achieve the required reduction in rate and record only the events of physical interest, the CDF trigger has been designed as a three-level system. Each level receives the data event from the previous level and, using more accurate detector information and more time for processing, makes a decision to reject or accept the event. Level 1 takes input from only a subset of the detector components. Signals from the front-end electronics are fed to Level 1, which has 5.5 μs to make its decision. The rate of events passed to Level 2 is typically about 25 KHz and it is limited to about 50 KHz. At Level 2 additional information, including $r - \phi$ hits from the SVXII, is incorporated. The events rate is reduced to 600-900 Hz. Level 3 performs a full reconstruction of the event in a similar, even if simplified, way as the offline program. Level 1 and 2 are hardware based systems that use custom electronics. Level 3 is a software based trigger system implemented on a farm of about 500 commercial computers which accepts events at a rate of 100-150 Hz. A schematic diagram of the trigger system is shown in Fig.3.13.
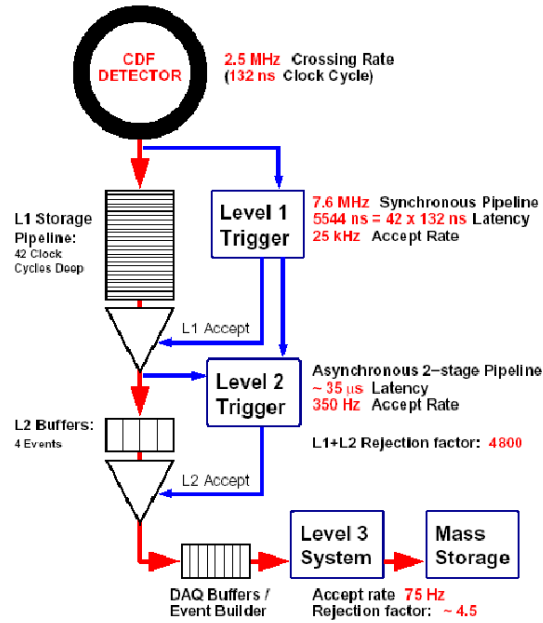
Figure 3.13: *CDF Trigger decisions tree flow.*

Level 1

Level 1 is a synchronous system of custom-designed hardware which reconstructs information from three parallel streams : the calorimeter (total energy and single tower information), the COT (only 4 axial superlayers are used for two-dimensional tracks) and the muon systems (stubs in the CMU,

CMP and CMX). The eXtremely Fast Tracker (XFT) is a custom processor used to identify two-dimensional tracks in the (r,ϕ) plane in the COT. The XFT is capable of reconstructing tracks with $p_T > 1.5$ GeV with an efficiency of about 95% and a fake rate of a few percent. The XFT has an angular segmentation of 1.25°, and an angular resolution of 0.3°. The momentum resolution is $\sigma_{p_T}/p_T^2 \equiv 1.7\%/$GeV/c. XFT sends the tracks to the extrapolation unit (XTRP) which feeds three L1 elements: L1 CAL, L1 TRACK, and L1 MUON. L1 CAL and L1 MUON use extrapolated tracks and information from the calorimetry and muon systems respectively to search for possible electron, photon, jets and muon candidates. All three systems report decisions to the Global Level 1 system. The accepted events are buffered for Level 2 analysis.

RUN II TRIGGER SYSTEM
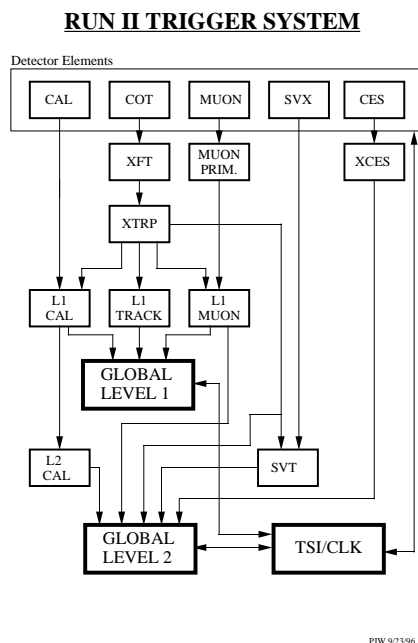
Figure 3.14: *CDFII Trigger structure.*

Level 2

Level 2 is an asynchronous system of custom-designed hardware and processes events from Level 1 in the order they are accepted. It incorporates additional information from the shower-max drift chambers in the central EM calorimeter and the axial hits from the SVXII detector. An approximate energy clustering in the calorimeters is performed. An especially powerful Level 2 trigger processor is the Silicon Vertex Trigger (SVT). The SVT combines data from the XTRP and the SVXII detector to compute track parameters with resolution similar to the one achieved by the offline recon-

struction program. SVT is then used to select events containing displaced tracks, essential to identify B hadrons decays. The Level 2 output rate is around 900 Hz.

A diagram of the decision process from the detector to Level 2 is shown in Fig.3.14.

Level 3

The final level of the CDF trigger is implemented exclusively in software on 500 commercial processors running in parallel. The output for each event passing the Level 2 trigger is read via optical fibers from all the sub-detectors and sent to the processors for a full event reconstruction. About 140 trigger paths are implemented at this level and the available output rate is around 150 Hz.

3.3   Organization of a Trigger Table

The trigger system described above is able to use the information of almost all the detector subsystem. Combining all the measurements of the various subsystems it is possible to efficiently record, at the same time, events characterized by different signatures. Indeed the data collected by CDF II can be used to study the properties of the top quark and weak bosons as well as the decays of b and c hadrons, or to search evidence of physics beyond the Standard Model.

Each signature requires certain selections at each trigger level, to efficiently collect the data. The combination of these selections define a Trigger Path. All the Trigger Paths are listed in the Trigger Table. The Trigger table is changed time by time acording to the accelerator performance, detector status, and scientific goals.

3.4   Special Hardware Trigger for B Physics: SVT

The main advantage of investigating B physics in an hadronic environment like the Tevatron is the very large ($\mathcal{O}\left(50\mu b\right)$), to be compared with $\mathcal{O}\left(1nb\right)$ b-flavor production cross section at the e^+e^- machines. However the large b-cross-section has to be compared with the total inelastic $p\bar{p}$ cross section section which is about 1,000 times larger. This means that b events are overwhelmed by an amount of uninteresting background events larger by three orders of magnitude. A further complication is that the b production cross section is a steep exponentially decreasing function of the p_T of the produced B. This results in b events populating mainly the soft region of the p_T spectrum (4-5 GeV/c) which is the region where also most of the background is distributed. In the CDF II case, this problem is enhanced by

the characteristics of the detector which was originally designed to optimize its performances in the central region where high-p_T decay products of particles such as $W^{\pm}$ and Z^0, top are searched.

The task of improving the unfavorable ratio between b events and background is two-fold. An on-line selection is in charge to select samples enriched in b-flavors. Once this is done, sophisticated off-line algorithms allow to further purify the sample from the background events. CDF trigger strategy in Run I was to take advantage of the excellent lepton identification capabilities to implement lepton-based triggers able to select semileptonic B decays and $B \rightarrow J/\psi + X \rightarrow [l^+ l^-] + X$ decays. At off-line level CDF used the silicon vertex detectors to reconstruct secondary vertexes allowing further skimming of b-enriched samples. This was possible because b-hadrons produced at Tevatron have enough high p_T to travel several hundredths of microns ($\sim 450\mu m$ for a B meson) through the detector before the decay. It results in large mean valued distributions of their impact parameters with respect to the beam axis. However such a lepton based trigger is not very efficient and excludes a whole bunch of rarer hadronic decays, such as $B_s^0 \rightarrow h^+ h^-$ ($h =$ hadron), $B_s^0 \rightarrow D_s^- \pi^+$, etc. which are among the most promising for CP violation measurements. To overcome this problem, in RunII a specialized trigger system, called Silicon Vertex Trigger (SVT), has been designed and implemented in the trigger system. The basic purpose of SVT is to anticipate the step of secondary vertexes identification from the off-line to the trigger level. This allows the on-line selection of b-events over the short-lived background with larger yield than by using only the leptonic triggers. In order to achieve this it is necessary to measure the impact parameter on-line. SVT performs this task reaching a resolution on fitted track parameter comparable to the off-line resolution and with a processing time of $\sim 15\mu s$. A brief description of the SVT architecture is given in the following section [38].

3.4.1 SVT at work

Reconstructing decay vertexes on-line is technically challenging and it requires the reconstruction of high resolution tracks at high event-rates. SVT measures the impact parameters of the charged particles, which is faster than reconstructing their decay vertexes, and provides information on the lifetime of the decaying particle as well. The COT tracks are not measured with the desired resolution, therefore SVT needs in input all the SVXII data. Due to this need, its natural location within the trigger chain is at Level-2. At this stage, the 2D COT tracks previously reconstructed by XFT are available and the event rate is sufficiently low to allow the readout of the silicon detector. XFT tracks are provided together with the silicon hit information

coming from SVXII front-end electronics. The design of a silicon front-end electronics capable to readout the more than 400,000 SVXII channels within the time constraint of the Level-2 trigger was a challenging task which turned out to be successful.
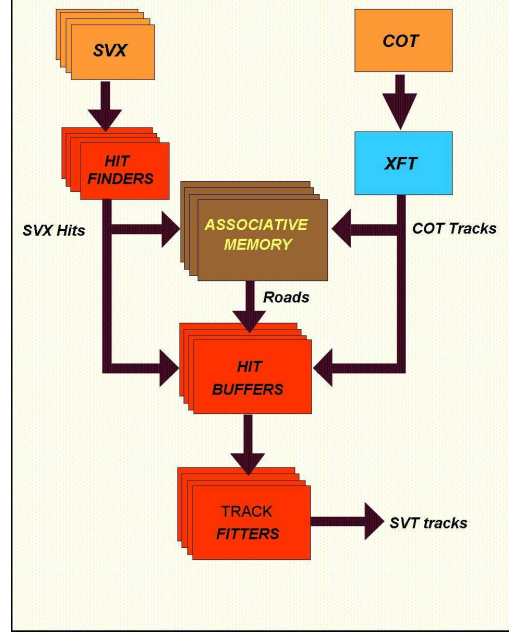

Figure 3.15: *SVT architecture.*

The output of SVXII is fed to the Hit Finder board (HF). This set of processors reconstructs the hit clusters on SVXII layers and calculates the coordinates of the charge center of gravity in each cluster. Hit Finder processing speed sustains the output rate of the SVXII front-end and calculated hit coordinates are sent in parallel to the Hit Buffer board (HB) and to the Associative Memory (AM++) located into the Associative Memory/Road Warrior board (AMS+RW). Simultaneously, XFT track parameters are transmitted both to the HB board and the Associative Memory. AM++ is the device devoted to pattern recognition. The Level-2 latency time does not allow SVT to adopt the off-line-like pattern recognition strategy based upon solving the whole system of constrained equations. AM++ uses instead a technique based on highly parallelized comparison between XFT-SVXII data and preselected patterns. The channels of each silicon layer are grouped into superstrips. A typical superstrip size for the silicon detector is $\sim 250\mu m$, while the detector typical full resolution is about $25\mu m$. The task of the AM++ is then reduced to perform pattern recognition using a coarser spatial resolution. A road is defined as one possible combination of superstrips (one per layer). An SVT track is identified when the matching of a pre-stored

43
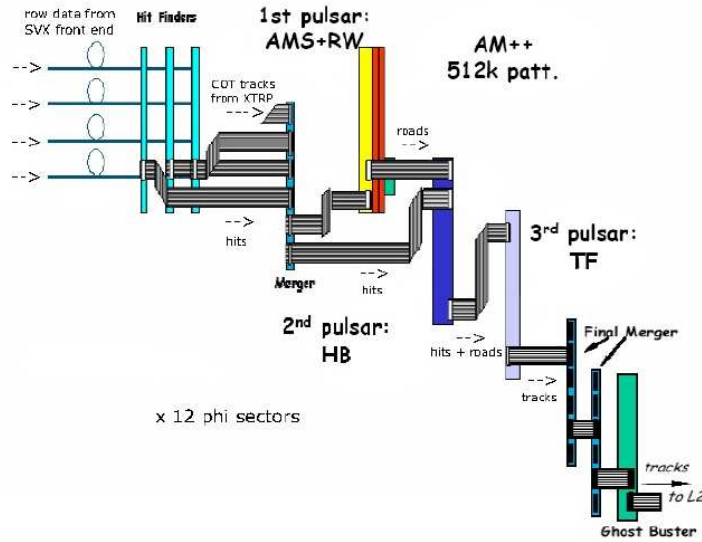
Figure 3.16: *SVT boards connections for a single wedge.*

road with the hit list occurs. In principle, it would be possible to store in the AM++ all possible roads for whatever configuration of real tracks, then compare them to the sequence of hits coming from the Hit Finder and to the 2D tracks reconstructed by XFT. In practice, due to the limit in memory size of the AM++ system, an efficiency $\epsilon \sim 95\%$ is achieved storing in the AM only a subset ($\approx 512K$ roads) of the all possible patterns. The AM++ performes the comparison with each road in parallel. The maximum output of the AM is 64 roads per event, each one having a maximum of 8 hits per superstrip.

This HB device is a buffer which stores the XFT track and the Hit Finder information during the AM++ processing. When AM++ comparison is completed the Hit Buffer sends to the Track Fitters (TF) only the stored data corresponding to the roads matched by the AM++. The Track Fitters are a system of processors operating in parallel devoted to fit tracks parameter with final resolution. Each processor receives the roads found by the AM++, the hit coordinates and the XFT parameters from the Hit Buffer. It combines the information and reconstructs one or more tracks within the same road performing a linearized fit procedure.

44

The SVT outputs are the reconstructed parameters of the two-dimensional tracks in the transverse plane: ϕ_0, p_T, and the impact parameter, d_0 . The list of parameters for all found tracks is sent to Level-2 for trigger decision. The SVT measures the impact parameter with $\sigma_{d_0}^{SVT} \approx 35\mu m$ r.m.s. width. This resolution is comparable with the off-line performance for tracks not
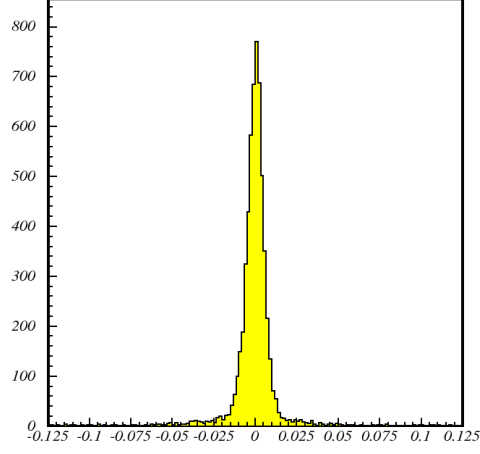
Figure 3.17: *Impact parameter resolution.*

using Layer00 hits, and yields a distribution of impact parameter of prompt tracks with respect to the z axis with $\sigma_{d_0} \sim 47\mu m$ (see Fig.3.17) when combined with the transverse beam-spot size. The SVT efficiency is higher than 85%. This efficiency is defined as the ratio between the number of tracks reconstructed by SVT and all XFT-matched off-line silicon tracks that are of physics analysis quality.

3.5   Trigger selections for B physics

Three types of dedicated triggers select events containing B mesons decays from QCD background events at CDF:

1. di-muon trigger

2. semileptonic trigger

3. hadronic track trigger.

The di-muon trigger selects muon pairs with a minimum transverse momentum cut of 1.5 GeV/c per muon. The semileptonic trigger selects events with a lepton (e or μ) with $p_T > 4GeV/c$ and an SVT track with $p_T > 2GeV/c$, in addition the impact parameter of the SVT track must be greater than $200\mu m$. The hadronic trigger is also usually called Two

45

Track Trigger. It selects two SVT tracks which satisfy the following requirements: sum of transverse momentum $p_{T1} + p_{T2} > 5.5 GeV/c$, opening angle $2° < \delta\phi < 90°$, impact parameter d_0 with respect to the primary vertex $120\mu m < d_0 < 1mm$, and decay length greater than $200\mu m$.

Chapter 4

Data Sample And Trigger Selection

4.1 Characteristic topology of B decays

After a B^0 meson is produced, it will decay with an average lifetime $\tau \approx 1.5ps$ in the rest frame of the B^0 meson. The typical proper decay length can be estimated from $c\tau \approx 450\mu m$, where c is the speed of light. This implies that the decay vertex is well separated from the collision point and this is a distinctive feature of the B meson decays.

The topology of the decay chains $B^0_s \rightarrow \phi\phi$ and $B^0_s \rightarrow J/\psi\phi$ with $\phi \rightarrow K^+K^-$ and $J/\psi\phi \rightarrow \mu\mu$ is shown in Fig.4.1 and 4.2.

The decay length L of a B meson is the distance between its production vertex, the primary vertex (PV), and the decay point in the laboratory frame, the secondary vertex. The parameters of the B meson daughter tracks and
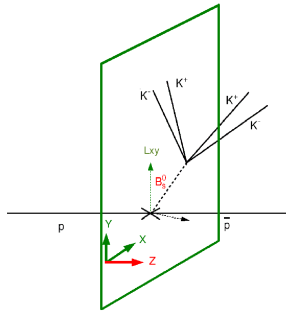
Figure 4.1: *Sketch of the $B^0_s \rightarrow \phi\phi$ decay.*

the primary vertex coordinates are needed to measure this quantity. The former are used to reconstruct the four-momentum and the decay vertex of the B meson. The latter gives its production space-point. The decay length
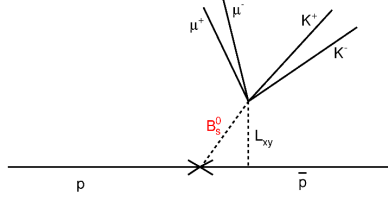
Figure 4.2: *Sketch of the $B_s^0 \to J\psi\phi$ decay in the $Z - Y$ plane.*

L is determined in the following manner:

$$
\begin{aligned}
ct &= ct_{lab}/\gamma \\[2ex]
&= c\frac{L_{xy}/(sin\theta \cdot v)}{\gamma} \\[2ex]
&= c\frac{L_{xy}M_B}{p_T}
\end{aligned}
$$

where L_{xy} is the transverse decay length defined as

$$
L_{xy} = \frac{\vec{V} \cdot \vec{p_T}}{|\vec{p_T}|} \tag{4.1}
$$

and $\vec{V}$ is the vector pointing from the primary to the secondary vertex position. Both vectors $\vec{V}$ and $\vec{p_T}$ are two-dimensional vectors, defined in the $r - \phi$ plane.

L_{xy} is one of the basic quantity used in the event selection for this analysis.

4.2 The Two Track Trigger

We describe the Two Track Trigger (TTT) path that is used in our analysis. The term Two Track Trigger (TTT) is used within CDF to indicate two kind of triggers that require at least two charged tracks in the event, with some kinematic constraint that we are going to describe in the following. These triggers are able to extract fully hadronic decays from a large background of tracks, just using the tracks reconstructed by SVT. The two triggers differ by the fact that one is meant to collect two-body decays, like $B^0 \to \pi\pi$, $B_s^0 \to kk$ (B_PIPI), while the other (B_CHARM) is sensitive to multi-body decays, like $B_s^0 \to \phi\phi$. The analysis described in this thesis will use the data sample collected using the B_CHARM section of the TTT.

More specifically we use the following trigger-paths:

- B_CHARM_LOWPT

- B_CHARM_L1

- B_CHARM_HIGHPT

- B_CHARM_PHI

Due to some processing problem of the `B_CHARM_PHI` trigger-path, the data acquired with this trigger were not used for the final analysis.

4.2.1   B_CHARM_LOWPT Trigger Path

This sequence was designed to maintain a high rate of selected events when the store has a low luminosity. The trigger path is variously prescaled during the store and activated only below a certain luminosity threshold (this is called a *lumienable* trigger-path). In the last period of the data taking it was never active because the store was dropped before reaching the threshold in question.
The Level 1 requirements are:

- two tracks with $p_T > 2.04$ GeV/c, as measured by XFT;

- each of the two tracks must have *hits* in at least 4 COT *layers*;

- $\Delta\phi < 90°$, where $\Delta\phi$ is the distance in ϕ angle between the two tracks;

The two tracks are not required to have opposite charge.

The Level 2 requirements are:

- two tracks with:

    - $\chi^2_{SVT} < 15$, where χ^2_{SVT} is the χ^2 of the track fit performed by SVT;
    - $120\ \mu m < d_0^{SVT} < 1$ mm, where d_0^{SVT} is the impact parameter of the track as computed by SVT;
    - $p_T > 2$ GeV/c;

- the couple of tracks must satisfy:

    - $2° < \Delta\phi < 90°$ [1];
    - $L_{xy} > 200\ \mu m$;

Finally, at Level 3 the requirements are:

---

[1]This cut in $\Delta\phi$ is used to select B meson decays into more than two bodies. For decays into two bodies, the condition $\Delta\phi > 20°$ is imposed because the opening angle of the tracks cannot be very narrow due to the kinematics and the relatively high mass of the B meson. In the presence of more than two bodies instead, the $\Delta\phi$ cut cannot exclude small angular separations between tracks.

49

- two tracks, each of which must satisfy:

  - $p_T > 2$ GeV/c;
  - $80\mu m < d_0 < 1$ mm;
  - $|\eta| < 1.2$;

- the couple of tracks with:

  - $2° < \Delta\phi < 90°$;
  - $\sum p_T > 4$ GeV/c;
  - $|\Delta z_0| < 5$ cm, where z_0 is the z coordinate of the point of closest approach to the z axis of the track.
  - $L_{xy} > 200$ μm.

It is interesting to observe that even at Level 3 no condition on the charge of the tracks is required.

There are other *trigger-paths* which, in addition to the requirements listed above, ask at Level 1 the presence of track segments in the muon detectors at a position estimated from the extrapolation of the XFT track. These *trigger-path* are used in this analysis as well.

4.2.2   B_CHARM_L1 Trigger Path or Scenario A

Scenario A is the trigger-path which collected more data due to the trigger selection cuts which allow us to acquire a significant rate of events at low instantaneous luminosity while maintaining trigger rates at a sustainable level at moderate high values of the luminosity.

At Level 1 the requirements are:

- two XFT tracks with opposite charge and $p_T > 2.04$ GeV/c;

- each of the two tracks must have *hits* in at least 4 COT *layers*;

- $\Delta\phi < 135°$

- $\sum p_T > 5.5$ GeV/c.

At Level 2:

- two tracks with opposite charge;

- each track must satisfy the following conditions:

  - $\chi^2_{SVT} < 15$;
  - 120 μm $< d_0^{SVT} < 1$ mm;

50

$\quad$ – $p_T > 2.0$ GeV/c;

- the couple of tracks must satisfy:

  – $2° < \Delta\phi < 90°$;
  – $\sum p_T > 5.5$ GeV/c;
  – $L_{xy} > 200\ \mu$m;

Finally at Level 3:

- two tracks with:

  – $p_T > 2$ GeV/c;
  – $80\ \mu$m $< d_0 < 1$ mm;
  – $|\eta| < 1.2$;

- the couple of tracks must satisfy the following conditions:

  – $2° < \Delta\phi < 90°$;
  – $\sum p_T > 5.5$ GeV/c;
  – $|\Delta z_0| < 5$ cm;

4.2.3   B_CHARM_HIGHPT Trigger Path

Initially, this trigger was conceived as a not prescaled trigger with tighten condition on the selections rules in order to allow us to acquire B physics data at high luminosity. Currently, the rate conditions at high luminosity are very severe and B_CHARM_HIGHPT has a dynamic prescale as well.

At Level 1:

- two XFT tracks with opposite charge and $p_T > 2.46$ GeV/c;

- each of the two tracks must have *hits* in at least 4 COT *layers*;

- $\Delta\phi < 135°$

- $\sum p_T > 6.5$ GeV/c.

At Level 2:

- two tracks with opposite charge;

- each track must satisfy the following conditions:

  – $\chi^2_{SVT} < 15$;
  – $120\ \mu$m $< d_0^{SVT} < 1$ mm;

51

- $p_T > 2.5$ GeV/c;

- the couple of tracks must satisfy:

  - $2° < \Delta\phi < 90°$;
  - $\sum p_T > 6.5$ GeV/c;
  - $L_{xy} > 200 \ \mu$m ;

Finally at Level 3:

- two tracks with:

  - $p_T > 2$ GeV/c;
  - $80 \ \mu$m $< d_0 < 1$ mm;
  - $|\eta| < 1.2$;

- the couple of tracks must satisfy the following conditions:

  - $2° < \Delta\phi < 90°$;
  - $\sum p_T > 5.5$ GeV/c;
  - $|\Delta z_0| < 5$ cm;

This trigger-path is mainly characterized by more selective requirements on p_T and $\sum p_T$.

4.2.4   B_CHARM_PHI Trigger Path

The trigger-path is very different from the others in the selection strategy, which is not only based on requirements on the p_T and d_0 of the tracks and on the topology of the event, but also on the request that two track invariant mass, M_{inv}, is within an interval around the ϕ mass. The motivation of this trigger is to improve the CDF trigger ability to select B decays containing a ϕ between their decay products; these decays are considered among the more important channels to be studied at CDFII.
Again, this trigger is prescaled and enabled only under a fixed value in luminosity.
This trigger-path was inserted into the CDF trigger table at a later stage.

At Level 1 the requirements are:

- two XFT tracks with opposite charge and $p_T > 2.04$ GeV/c

- each of the two tracks must have *hits* in at least 4 COT *layers*;

- $\Delta\phi < 90°$

52

Note the difference in the $\Delta\phi$ cut compared to the trigger-paths described in the previous sections and the absence of requirements on $\sum p_T$.

At Level 2:

- two tracks with opposite charge;

- each track must satisfy the following conditions:

  - $\chi^2_{SVT} < 15$;
  - $100 \ \mu\text{m} \ < d_0^{SVT} < 1 \ \text{mm}$;
  - $p_T > 2.0 \ \text{GeV/c}$;

- the couple of tracks must satisfy:

  - $0° < \Delta\phi < 6°$;

The $\Delta\phi$ angular selection is tighten compared to the other trigger-paths and no cut is applied on L_{xy}. The requirements on the impact parameter is less stringent instead.

Finally at Level 3:

- two tracks, each of which must satisfy:

  - $p_T > 2 \ \text{GeV/c}$;
  - $50 \ \mu\text{m} \ < d_0 < 1 \ \text{mm}$;
  - $|\eta| < 1.2$;
  - $0 < M_{inv} < 1.04 \ \text{GeV/}c^2$;

- the couple of tracks must satisfy the following conditions:

  - $0° < \Delta\phi < 6°$;
  - $|\Delta z_0| < 5 \ \text{cm}$;

The selections specific of this trigger-path are the $\Delta\phi$, the impact parameter and the invariant mass cuts.

4.3   Data Sample

The data used for the analysis of the $B_s \rightarrow \phi\phi$ decay described in this thesis were collected between March 2002 and April 2008. They correspond to an integrated luminosity of 2.9 fb^{-1}. Only *runs* which satisfy a set of requests on data quality are retained and define the so called 'goodrun list'. In CDF, the quality of the data are verified offline by a team of physicist and

53

the conditions of the various parts of the detector are asserted by detector experts.

In particular, data quality criteria are:

- a minimum integrated luminosity during the run;

- reliability of the trigger tables;

- no problems in data storage;

- consistency in the observed number of events for several particles and decay channels easy to analyze;

- status of various parts of the detector.

These quality selections are also important to obtain a reliable simulation of the CDFII detector via Monte Carlo simulation.

In particular, in our analysis a quality check is required for:

- Trigger, SVT, SVXII and COT.

The subdivision of the events used in this analysis between the different trigger-paths are summarized in Table 4.1 and 4.2 (the events are selected with the criteria that will be explained in Chap.6). They are selected using: `B_CHARM_HIGHPT` (HIGHPT); `B_CHARM_`$L1$ and removing the events triggered by `B_CHARM_HIGHPT` as well (ScAnoHIGHPT); `B_CHARM_LOWPT` and removing the events triggered by `B_CHARM_HIGHPT` and `B_CHARM_`$L1$ as well (LOWPTnoScAnoHIGHPT). In what follows, these three classes of trigger requirements are referred as 'exclusive triggers'.

Trigger path	Fractions
HIGHPT	0.394 ± 0.048
ScAnoHIGHPT	0.377 ± 0.048
LOWPTnoScAnoHIGHPT	0.223 ± 0.037

Table 4.1: *Fractions of events between exclusive triggers for* $B_s \to \phi\phi$ *decays.*

4.4 The data format and the analysis software

After the acquisition and storage of data to tape, the data are analyzed by the reconstruction program of CDFII and the output data are divided into different datasets, available to users. At this point, the groups involved in data analysis in specific areas of physics have developed different software

Trigger path	Fractions
HIGHPT	0.416 ± 0.021
ScAnoHIGHPT	0.326 ± 0.018
LOWPTnoScAnoHIGHPT	0.259 ± 0.016

Table 4.2: *Fractions of events between exclusive triggers for $B_s \rightarrow J/\psi\phi$ decays.*

programs aimed to process data and obtain all the relevant information for the analysis of interest. For the study and analysis of B candidates a special software package was developed. This software is able to perform the reconstruction of several B mesons decays applying some minimal selection criteria on the characteristics of the decays. The result is saved in a particular software framework which is called 'Bstntuple'. It is essentially a modified version of the more general 'Stntuple' package developed and used in CDF. Bstntuple is a more sophisticated ROOT ntuple [39] with the addition of tools, functions and classes useful for the analysis of the B mesons decays. The Bstntuple contains structures to hold all the relevant informations of the various reconstructed B mesons decays. They contains as well the variables used for the identification of particles (dE/dx, TOF, μ and electrons quantities) and the result of the algorithms used to determine the flavor of the B at the moment of its production.

Finally, it should be highlighted that the Bstntuples framework has been an efficient tool in terms of CPU usage time and of data uniformity, that allowed us an easier production of the different decays and data samples used in our analysis. On the other hand, the Bstntuples are an analysis tool which has been available only by about 2-3 years. This means that not all the reconstructed decays have been fully tested and the analysis undertaken in this thesis is actually the first work on the B decays with a ϕ in the final state in the TTT that employs the Bstntuples.

4.5   Offline Reconstruction

In this section some details of the offline reconstruction relevant to our analysis are presented.

4.5.1   Primary Vertex Reconstruction

Two methods of estimating the primary vertex are commonly used. The first method uses the time-dependent average beamline, which determines

the beamspot with a lateral error of about 30 μm [43]. The second method uses the event-by-event primary vertex reconstructed from tracks in the event which do not belong to the reconstructed B mesons [44, 45]. The event-by-event primary vertex obtains a more accurate primary vertex position, and thus a more accurate estimate of the proper decay length.

4.5.2 Track Quality Cuts

To ensure the use of high quality tracks, a candidate track is required to have at least 5 COT hits from at least 2 axial and 2 stereo COT super-layers. For the tracks corresponding to the muons from $J/\psi \to \mu\mu$ and the kaons of the $\phi \to K^+K^-$ at least 3 $r - \phi$ silicon hits, which can include ISL and L00 hits, are also required.

4.5.3 The $\phi \to K^+K^-$ reconstruction

To search for a ϕ candidate, we examine pairs of oppositely charged, non-muon tracks among particles that originate from a common displaced vertex. For the mass reconstruction, the two tracks are assumed to be kaons. The pair is kept if its invariant mass is within $1.008 < m(K^+K^-) < 1.032 GeV/c^2$.

4.5.4 Muon Identification and Selection

A muon candidate is formed by a muon hit cluster (stub) in the muon chamber position-matched to a single track in the tracking system. A cut on the χ^2 of the position match between track segments in the CMU or CMX and the extrapolated track in the $r - \phi$ plane is applied. Should a muon stub be matched to more than one track, the ensemble with the minimum χ^2 is selected as the muon candidate. The muon tracks used are of any of the following types: CMU, CMP, CMUP and CMX with the requirement of $p_T > 1.5$ GeV/c.

4.5.5 $J/\psi \to \mu\mu$ reconstruction

J/ψ candidates are formed from pairs of oppositely charged muons in the events of the sample. The two muons are fitted to a common vertex using the kinematic fitting program called CTVMFT [46] via the C++ wrapper VertexFit at CDFII. The fit returns a χ^2 as well as an estimated vertex position, and refitted vertex-constrained tracks. The refitted tracks are used to estimate the relevant quantities like p_T and fitted J/ψ invariant mass. The $\mu\mu$ pair is considered as a J/ψ candidate if it has a vertex χ^2 probability > 0.001 and the fitted mass is within the range $3.014 < m(\mu\mu) < 3.174 GeV/c^2$.

Chapter 5

Monte Carlo Simulation

5.1 The simulation

A simulation of the events using Monte Carlo method is required in this analysis to evaluate different aspects: the estimation of physical background, the optimization of the cuts for the selection of the signal, the determination of trigger efficiencies for the calculation of the Branching Ratio. Thus it is important to understand when the simulation is reliable and when it is not. The process of simulation, which is used, occurs in the following steps:

- simulation of production and decay of quarks via:

  - b quark production;
  - fragmentation, hadronization and B mesons production;
  - B mesons decays.

- simulation of the interaction of the particles with the detector

- simulation of the trigger effects on the selection of the events.

The first point is implemented through two programs called BGenerator [40] and EvtGen [41].

BGenerator is able to simulate the production of individual b quark or $b\bar{b}$ pairs, then their hadronization into B mesons of the desired type and in the desired proportions, with the kinematic quantities associated with them.

EvtGen simulates the decays of the B mesons.

The simulation of the interactions of the final state particles with the detector is realized, using a software (*cdfsim*) that implements a full simulation of the CDFII detector using the package *GEANT 3* [42], which allows us to model precisely the response of the interaction of the various elements of the detectors with the particles.

Finally the last point, namely the simulation of the trigger, is made using a software package called *TrigSim* [44] that is able to reproduce the behavior

of most of the trigger hardware elements. Actually, only the first two levels of the trigger are simulated; the third level is not simulated, but only the confirmation of the cuts applied at level 2 is required.

Finally the data output of the Monte Carlo simulation is in the same format as the real data, allowing an easier comparison between Monte Carlo and data for the validation of the simulation.

Now we describe in more detail the implementation of the different parts of our Monte Carlo simulation.

5.1.1 Triggers prescale configurations

The detector and trigger configurations have undergone several variations during RunII. Minor variations may occur between runs, while larger variations occur, for instance, after major hardware improvements, or Tevatron shut-down periods. For a more detailed simulation of the actual experimental conditions, the simulation has been interfaced with the off-line database that reports, on a run-by-run basis, all known changes in configuration (position and slope of the beam line, relative mis-alignments between subdetectors, used trigger-table, set of SVT parameters) and local or temporary inefficiencies in the silicon tracker (active coverage, noisy channels, etc.) and other detectors. This allows us to simulate the detailed configuration of any set of real data-taking runs for modeling the realistic detector response in any given subset of data.

Anyway it is important to underline that one information that is not stored is the instantaneous luminosity event by event (the value of the instantaneous luminosity is stored a certain number of times during the run). This implies that we are not able to reproduce exacly the full trigger behavior of some specific trigger-paths which have a built-in dependance on the instantaneous luminosity. This dependance is of different kinds, i.e.:

- Lumienable Trigger (LUMIENABLE)

- Dynamical Prescaled Trigger (DPS)

- Fractional Prescaled Trigger (FPS)

- Uber Prescale Trigger (UPS)

- Fractional Uber Prescale trigger (FUPS).

All this kind of triggers were introduced to use at best the Level1 and Level2 trigger bandwidths in order to store as much interesting data as possible. A trigger system which can make use non only of specific physics channel cuts but on the istantaneous luminosity as well is clearly more powerfull in achieving this task.

We use two types of prescaled triggers. Static prescales and dynamic prescales. Static prescales are fixed during the duration of a run: if a trigger is prescaled by a factor of N this means we will only accept one out of every N events that would have passed the trigger criteria.

LUMIENABLE triggers

This trigger-path is activated only when the istantaneous luminosity become lower than a fixed threshold.

DPS triggers

For DPS triggers the fraction of accepted events is not fixed but it changes during the run according to the instantaneous luminosity and the total trigger rates. Combining dynamic prescales and static prescales allows us to use the full data-taking bandwidth to accept as many events as possible and to give rare events high priority.

FPS triggers

It is similar to the previous one (DPS) but the fraction of events accepted instead of being $1/N$ $(1/10, 1/5 ...)$ could be a fraction such as $193/256$, $71/256$ etc. This is accomplished setting a register in a special board. It works well in data taking but it is difficult to simulate its behaviour in Monte Carlo.

UPS triggers

It is a "switch on-off" trigger like the LumiEnable ones. It is turned on after all the DPS triggers are at their minimum prescale values and the L1 rate is below a certain value.
It accepts the event if at that moment there are three or four free Level 2 memory buffers.

FUPS triggers

It is the 'fractional' version of the UPS trigger. There can be a maximun of 4 FUPS triggers, that will be turned on sequentially according to a 'priority' parameter assigned to them. It has not been used for data taking yet [46].

In order to solve the problem of the simulation of this kind of triggers some variables of the Monte Carlo output are compared with the same variables in data, and the fraction of the different triggers in Monte Carlo are

59

re-weighted according to the measured fraction of the triggers in data.

5.1.2 The generation of events

The first step in the simulation is implemented using BGenerator and consists in the production of b quarks that come from the primary proton-antiproton interaction, according to a certain momentum distribution, followed by the stage of fragmentation. The user can act both on the fragmentation and on the generation phase modifying some parameters (for example, fractions of the different kinds of B mesons).

The admixture of different hadrons containing a b quark is defined using several measurements reported by the Particle Data Group (PDG) [47], or may be imposed by the user in order to produce unique samples targeted to the study of a single channel.

This type of generator, unlike other more complex as Pythia [45], does not simulate all the aspects of the QCD $p\bar{p}$ interaction but it has the advantage to work much faster. The use of BGenerator is well suited for the simulation results needed for our analysis.

5.1.3 EvtGen

The decay of B mesons, on the other hand, is simulated using the program EvtGen. This simulation package is based on the amplitudes of decay and it is able to take into account the effects of the interference between amplitudes. The simulation uses decays tables in which the user must set the type of initial particles, the final branching fractions and the decay model to follow. In the literature [41] there is a substantial number of models that can satisfy most of the requirements for simulation of B physics processes.

One important feature of this package is that the transition probability from the initial state to the final state and through all the intermediate states is evaluated not as the product of each single step transition probability, but at first the amplitude of the transition along all the decay chain is evaluated, and only at this point the square module is computed. This is important because taking care of the effect of the phases in different transitions allow us to test different transition hypothesis.

5.1.4 The simulation of the detector and the trigger

As mentioned before, the simulation of the detector is performed through *cdfsim*, which is a package that contains all the information specific to the different elements of the detector, all the information on the position of the elements, and reproduces the interactions between different parts of the detector and the particles.

At the end, the response of detectors to particles that interact is described

60

in terms of hits or released energy. It essentially reproduces the real output of the detector.

For more details on this item, see [42].

For the simulation of the trigger there is a dedicated software, TrigSim, which simulates the operation of the boards of the first two trigger levels, the resulting output is stored in databases, known as banks trigger, allowing to emulate the algorithms of the various trigger levels. The decision process is achieved using a filter that reads the trigger banks and perform a selection of events following the requests of the available triggers. In this analysis only the Two Track Trigger is considered.

In an analysis performed on data collected in several different period of data acquisition, the data will be the result of specific and different configurations of the detector and the trigger. The Monte Carlo program should reliably reproduce all these configurations and this is achieved by imposing the settings and the conditions of each run using the informations stored in the databases. On the other hand, TrigSim is not able to simulate all the effects on all the system that determine the different types of trigger prescale. This means that the trigger-paths that depends on the instantaneous luminosity cannot be correctly simulated. For this reason it was important to evaluate the fractions of the different triggers in the different periods of data taking, and to provide them in input to the Monte Carlo (Tables 4.1 and 4.2).

The events generated in this way are then processed using the same software that produces the Bstntuples in order to obtain an output format equal to that of the data. This allows us to use the same program that selects the decays of our interest both on the data and on the Monte Carlo generated events.

5.2   The Monte Carlo validation

The validation of our Monte Carlo program consists in a test of reliability of our simulation using a comparison with the signal candidate events selected in the data. Furthermore, as explained before, in our Monte Carlo the trigger prescale cannot be simulated; so in order to make it more truthful we use a Monte Carlo with the same fractions of exclusive trigger as measured in data. For fraction of exclusive trigger we means the events fraction that is selected only by a particular trigger-path and not by the others. In principle a single event can fire many different trigger-paths, but if we want to re-weight the event fractions we have to have subsets of not-overlapping events. Afterwords, we can test the agreement of our Monte Carlo with real data comparing the distributions of several variables. The variables that are used for this purpose are the most significant for the selection and optimization procedure, such as:

- transverse momentum of the B meson: p_T^B;

- transverse decay length of the B meson: L_{xy};

- impact parameter of the B meson: d_0^B;

- impact parameter of the more energetic ϕ: $d_0{}_{max}^\phi$;

- transverse momentum of the J/ψ: $p_T^{J/\psi}$;

- transverse momentum of the less energetic kaon from ϕ decay: p_T^K;

- the bi-dimensional χ^2 of the primary vertex fit: χ^2_{xy}.

In Figures 5.1 and 5.2, 5.3 and 5.4 the histograms of the comparison of Monte Carlo versus data and of not-reweighted Monte Carlo versus reweighted Monte-Carlo are shown for the $B_s \to \phi\phi$ and $B_s \to J/\psi\phi$ channels.
In both cases optimized selection cuts were used (see section 6.3).
The comparison of data versus Monte Carlo has been made comparing the histograms of some variables for the Monte Carlo signal events with data where the background is subtracted. The subtraction of the background from the data (known as *sideband subtraction*) is performed subtracting from the events, in a window around the signal, in the invariant mass histogram of the B_s candidate, those events which are located in the same histograms in an area far from the signal peak (sideband).
We have neglected other types of background due for example to reflections of other B decays. In the following histograms, the probability obtained from a Kolmogorov test between the weighted Monte Carlo events and the data is reported. The test results show no significant discrepancies between distributions. This means that we are performing a good selection of exclusive triggers and the configurations we are using for the Monte Carlo simulation reproduce well the situation of the detector.
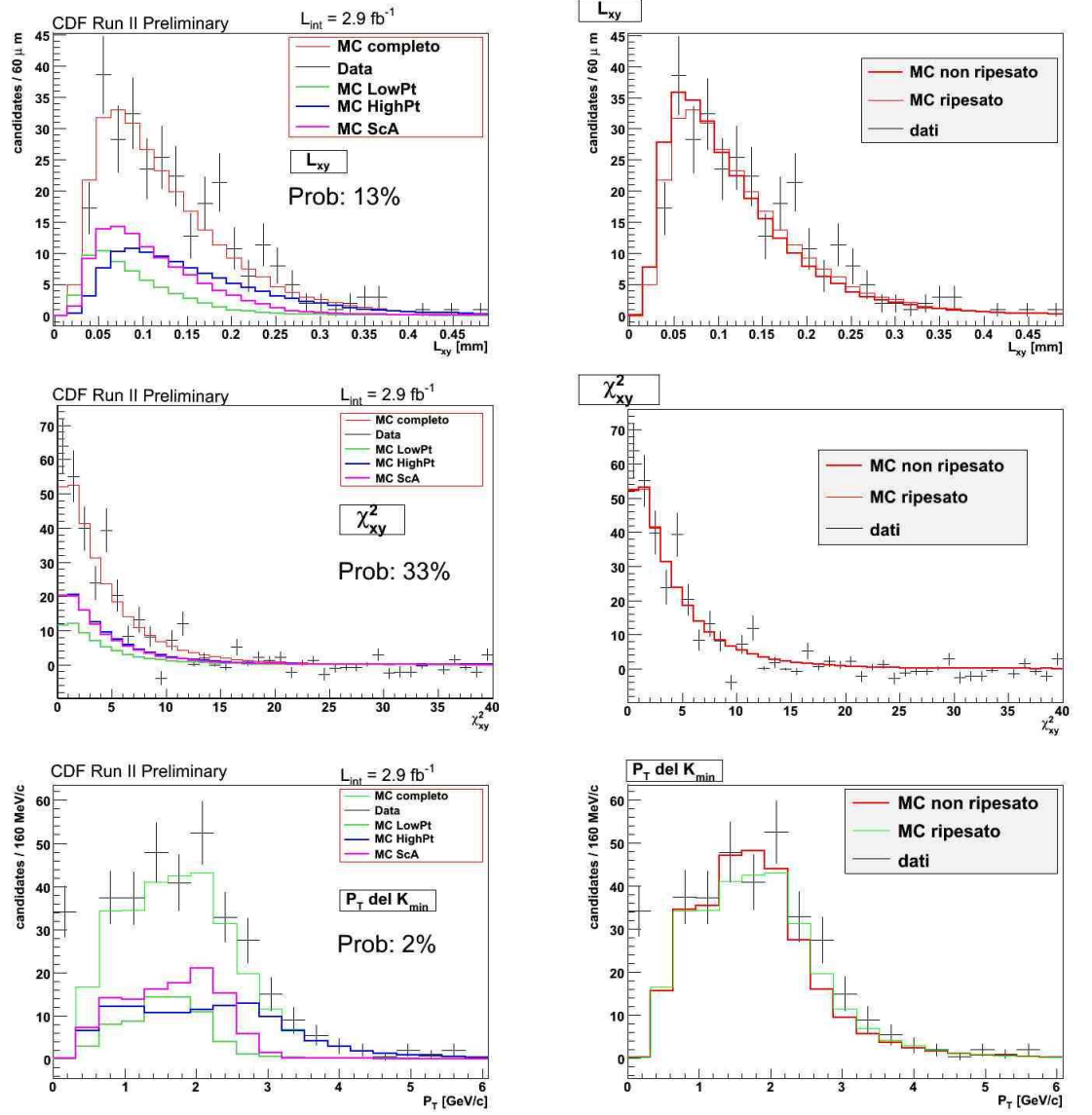
Figure 5.1: *Data-Monte Carlo comparison for $B_s \to \phi\phi$. On the left the data, total events and divided according to different trigger-path, compared with the weighted MC; on the right comparison between weighted and not-weighted Monte Carlo events. Using the Kolmogorov test a better agreement between data and weighted Monte Carlo is observed. The reported variables, proceeding from top to bottom, are: L_{xy} of the B meson decay, the χ^2_{xy} of the fit of the primary vertex and the transverse momentum of the kaon with less energy.*
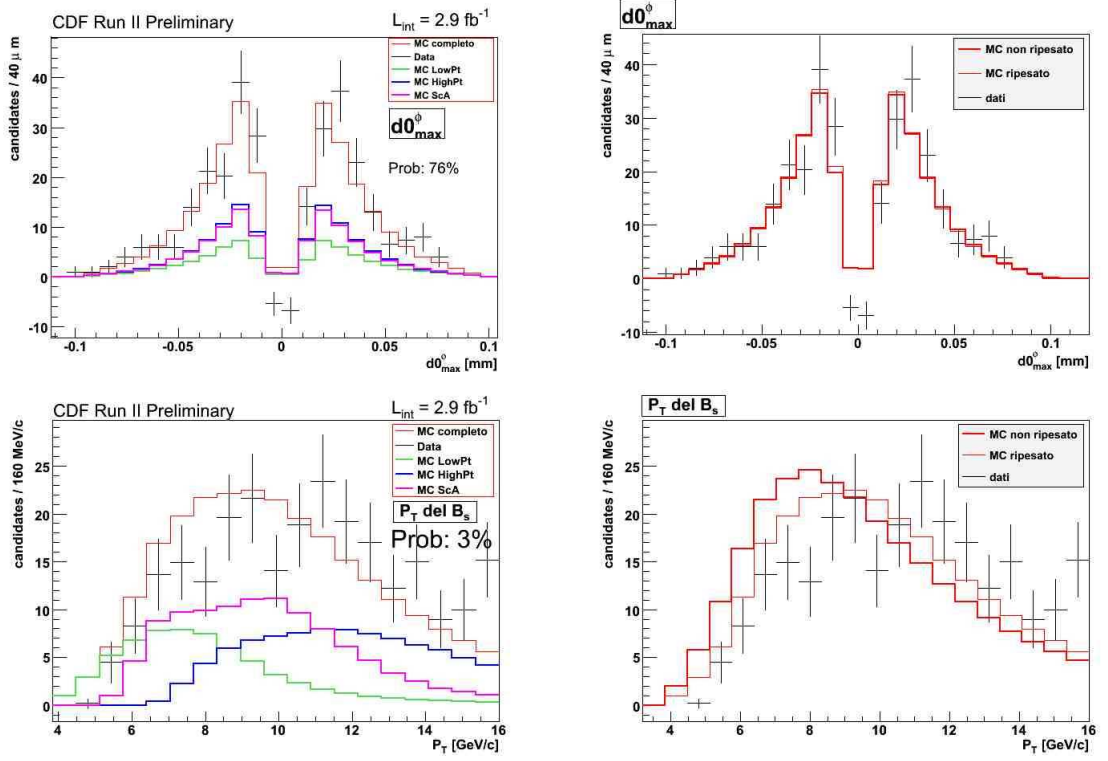
Figure 5.2: *Data-Monte Carlo comparison similar to that of Figure 5.1, for the distributions of the impact parameter of ϕ with higher energy and of the p_T of B.*
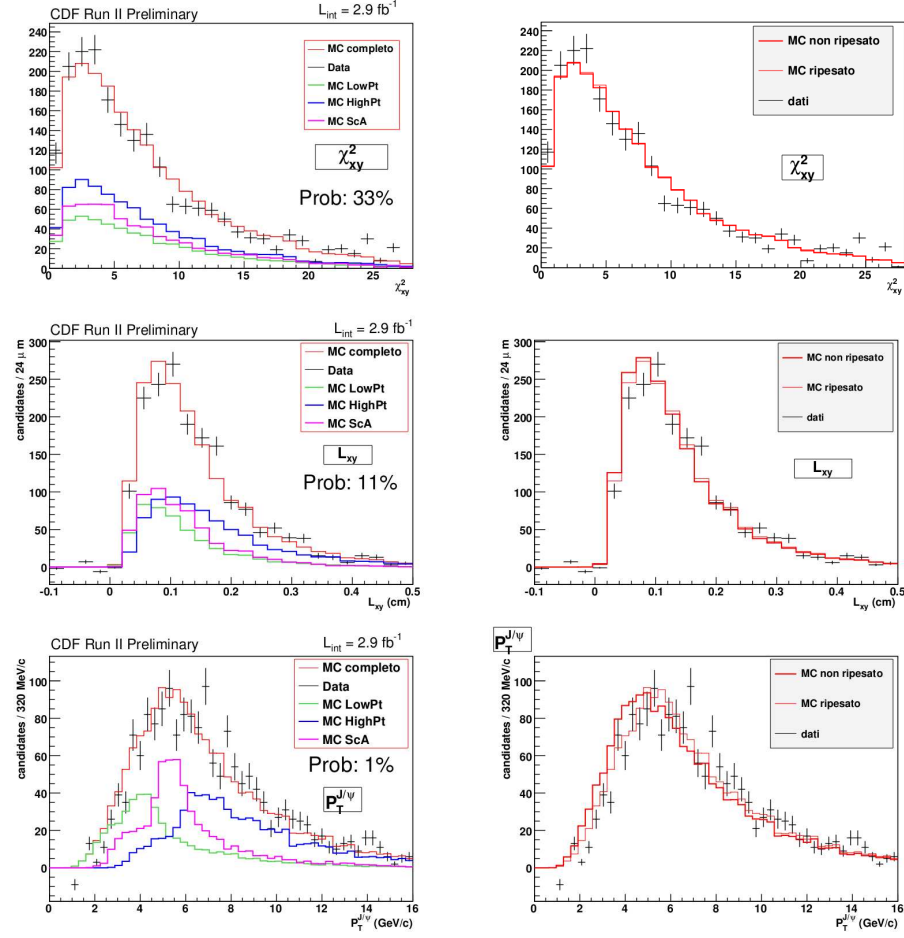
Figure 5.3: *Data-Monte Carlo comparison for $B_s \to J/\psi\phi$. From top to bottom the variables are: χ^2_{xy} of the fit on the primary vertex, the transverse decay length of the B_s, L_{xy}, and the transverse momentum of J/ψ.*

65
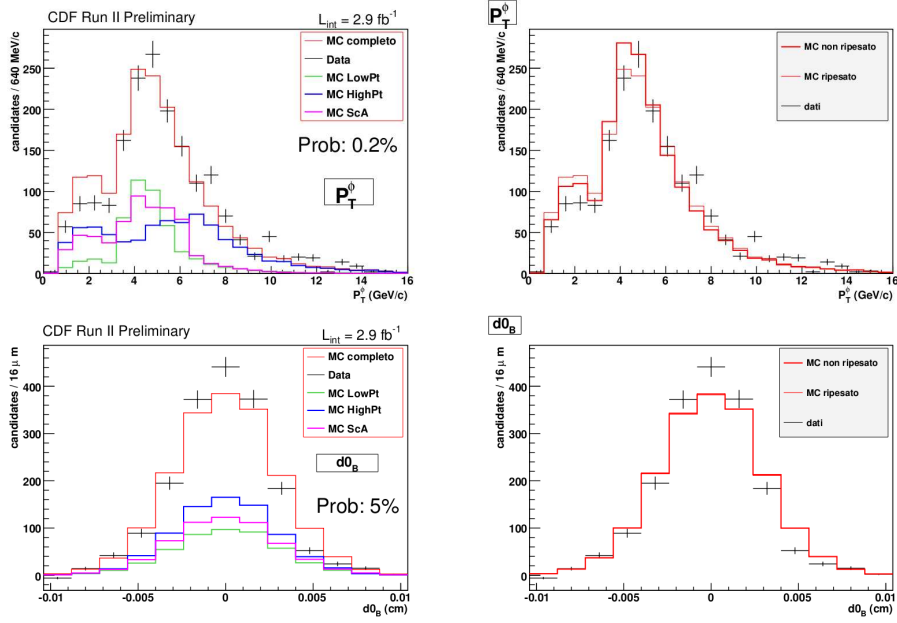
Figure 5.4: *Data-Monte Carlo comparison similar to that of the previous page, for the distributions of the transverse momentum of the ϕ and of the impact parameter of the B_s.*

Chapter 6

Analysis strategy and signal selection

The strategy followed in the signal selection and in the measurement of the Branching Ratio and the optimization procedure for the signals selection are reported in this chapter.

In section 6.4, we present the study on the number of the $B_s \rightarrow J/\psi\phi$ decays not selected using the DI_MUON trigger but using the TTT. This sample is useful to evaluate the statistic that could be gained in the measurement of this important decay channel using the TTT as well.

6.1 Strategy of the measurement of the Branching Ratio

Both the decays of our interest, i.e. the $B_s \rightarrow \phi\phi$ and $B_s \rightarrow J/\psi\phi$, have four charged tracks in their final state: respectively four kaons and two kaons with two muons. The Branching Ratio (BR) of the decay $B_s \rightarrow \phi\phi$, normalized to the already measured $B_s \rightarrow J/\psi\phi$, can be evaluated using the following formula:

$$\frac{BR(B_s \rightarrow \phi\phi)}{BR(B_s \rightarrow J/\psi\ \phi)} = \frac{N_{\phi\phi}}{N_{J/\psi\phi}} \cdot \frac{\epsilon_{TOT}^{J/\psi\phi}}{\epsilon_{TOT}^{\phi\phi}} \cdot \frac{BR(J/\psi \rightarrow \mu\mu)}{BR(\phi \longrightarrow KK)} \tag{6.1}$$

where $N_{J/\psi\phi}$ and $N_{\phi\phi}$ are respectively the number of events containing the decay $B_s \rightarrow J/\psi\phi$ and $B_s \rightarrow \phi\phi$ in our sample (corresponding to 2.9 fb^{-1} of data), while $\epsilon_{TOT}^{J/\psi\phi}$ and $\epsilon_{TOT}^{\phi\phi}$ are the trigger and reconstruction efficiencies for the two channels.

As a basic reference for the strategies and for the comparison with the results on the first 180 pb^{-1}, the analysis made by CDF in 2004 [1] is used; eight $B_s \rightarrow \phi\phi$ decays had been observed and a first measurement of the Branching Ratio was performed.

67

In the ratio of Eq.6.1 the uncertainties in the cross section of B mesons hadronic production cancel out as well as several systematic effects due to the detector, allowing us to reduce the error on the measurement of the BR. The $B_s \rightarrow J/\psi\phi$ decay is used in Eq.6.1 because it has a similar topology of the $B_s \rightarrow \phi\phi$ one, in particular it is characterized by the same number of decay vertexes and of charged tracks in the final state. The choice of the $B_s \rightarrow J/\psi\phi$ decay instead of the even more similar $B_d \rightarrow \phi K^*$ decay, is motivated by the fact that in this way the uncertainties in the ratio of the production cross section of B_s and B_d do not enter in our formula.

The ratio of the reconstruction and the trigger efficiencies that enters in the measurement is estimated using events simulated by Monte Carlo. The efficiency is obtained by applying to the MC events the same triggers configurations and the same cuts used in the reconstruction and signal selection on data. These efficiencies are calculated taking into account the prescale of the various triggers used in data analysis.

The reconstruction of the signal starts from the selection of the four tracks present in the final state through the identification of the secondary and the primary vertex.
The choice of the variables used for the selection of signals is based on a careful study of the kinematic characteristics of the two channels. In particular the B_s meson decay is characterized by a large transverse decay length and a small impact parameter.
The signal selection criteria are the result of a procedure for the optimization of the analysis cuts based on the maximization of the function $\frac{S}{\sqrt{S+B}}$, where S is the signal, simulated using Monte Carlo, and B is the background estimated from the data. This optimization has the advantage of minimizing the statistical error on the number of selected events [48].
In addition, to obtain a sample with a good signal to background ratio, J/ψ decays into two muons are selected with the request that at least one of the two muons is associated with a stub of the muon detectors. In this way the contribution of the $J/\psi \rightarrow ee$ decay is excluded from our sample. Furthermore the presence of muon stubs on both muons are not required to increases the statistics of the selected data. The efficiency of this selection is evaluated directly from the data.

6.2 The reconstruction of the $B_s \rightarrow \phi\phi$ and $B_s \rightarrow J/\psi\phi$ decays

The reconstruction of the decays is carried out using C++ programs which perform the following four steps:

- a first decay reconstruction through the Bstntuples software;

- preselection or *preskimming*;

- specific decay selection.

While the first two are independent of the selected decay and implemented broadly to select B meson events, the last one were designed, optimized and used in order to select these two particular decay channels.

An initial reconstruction of the decay, as mentioned in Sec.4.4, occurs via the software that produces the Bstntuples. The various B decays are reconstructed using the offline tracks and the information from the tracking system. Starting from the tracks we can obtain information on secondary vertexes and thus reconstruct the topology of the interesting decays. The algorithms for the reconstruction of B events performs a cycle on all the track candidates that meet the quality criteria (explained in section 4.5.2) and reconstruct all the decay products of unstable particles (in our case J/ψ and ϕ) doing the fit of the vertex from which we obtain the invariant mass and the vertex coordinates where the two tracks originate. Then two ϕ candidates (or a J/ψ candidate and a ϕ candidate) are considered together in order to perform a four tracks fit for a B candidate. In this way we can obtain for example χ^2_{xy}, L_{xy} and the invariant mass of the B meson candidate. When the decay involves the J/ψ, in the fit on the four tracks of the candidate to reconstruct the secondary vertex, one additional constraint is imposed: the invariant mass of the daughters tracks of the J/ψ have to be exactly the nominal mass [47] of the J/ψ. This condition, called *mass constraint*, improves the resolution on the B invariant mass. In fact, its resolution is around 10 MeV/c^2, while for the $B_s \to \phi\phi$ decay the resolution is about 20 MeV/c^2, as shown in Figure 6.1.
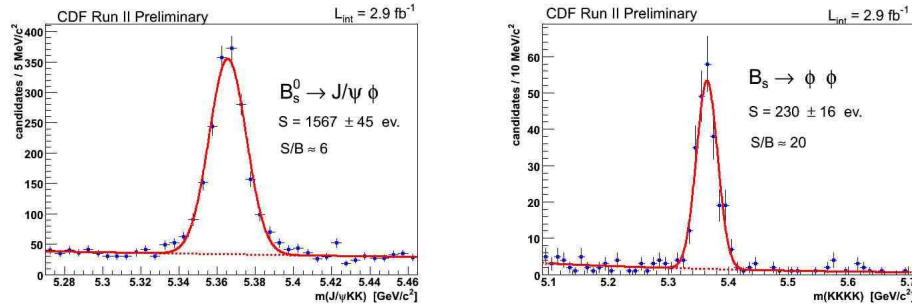
Figure 6.1: *Comparison of resolutions of the two decays. The graphs are obtained with non-optimized preliminary selections.*

Another important aspect concerning the reconstruction of the decays is the request that at least two of the four tracks match the SVT tracks, and these two tracks have to satisfy the trigger criteria of B_CHARM_LOWPT (trigger confirmation).

69

Despite these selections, there is a high combinatorial background. Each selected event has N_T tracks and combining them we look for combinations that are compatible with the decay that we want to study. The number of candidates expected for the reconstruction of a decay to n bodies using the N_T tracks, is given by:

$$N_C = \left(\begin{array}{c} N_T \\ n \end{array} \right) = \frac{N_T!}{n!(N_T-n)!} \tag{6.2}$$

For a large n, the number of candidates is growing considerably and the selections previously made are not sufficient to discriminate satisfactorily the signal from background, given the enormous number of possible combinations.

Thus we have to perform a selection based on the characteristics of the specific decay channels.

6.2.1   Preselection

The preselection is performed to reduce the huge combinatorial background in this sample and to get as small as possible and more manageable Bstntuples.

The cuts used are the following:

- $L_{xy} > 200\ \mu m$;

- $p_T^B > 5$ GeV/c .

The values of these cuts are chosen in order to make a selection only on the combinatorial background without virtually eliminating any signal event. As shown in Figure 5.3 the signal does not start before $L_{xy} > 200 \mu m$ due to the trigger cuts.

6.2.2   Selection

Despite these efforts for the discrimination of the signal, the combinatorial background is so huge that the discrimination of the signal is still impossible as shown in Figure 6.2. We need to optimize our selection criteria in order to maximize the signal to background ratio.

6.3   Selection optimization

6.3.1   Selection of the $B_s \rightarrow \phi\phi$ signal

What we want to get is a set of cuts that will increase the number of $B_s \rightarrow \phi\phi$ in the sample of analyzed data. One possible method is to look for the cuts

70
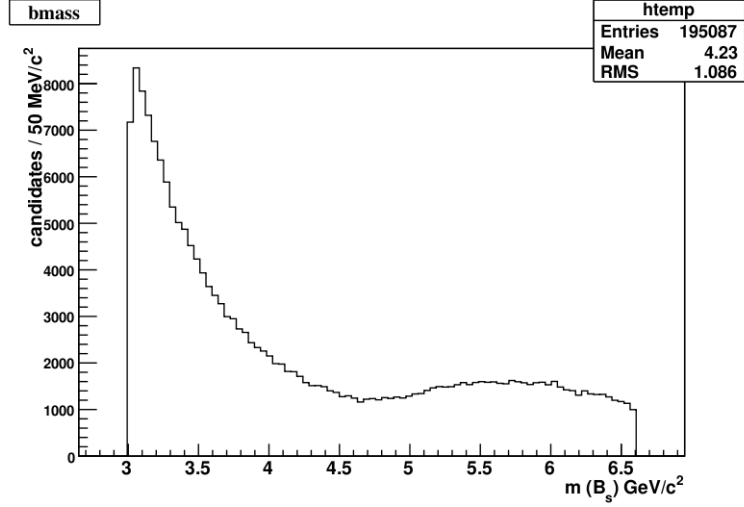
Figure 6.2: *B_s invariant mass distribution after the preselection.*

selection that maximizes the function (*score-function*) $\frac{S}{\sqrt{S+B}}$, where S is the signal, while B is the background in the invariant mass window of the B_s. The signal S is defined by the number of MC events that pass the selections and belong to a mass window of approximately $\pm 3\sigma$, around the B_s mass peak, i.e. [5.319, 5.419] GeV/c^2. The background is determined by the number of events in the *sideband* (SB), defined as the reconstructed B_s mass window of [5.52, 5.72] GeV/c^2.

For this channel, several sets of possible variables were considered starting from those used for the $B_s \rightarrow \phi\phi$ discovery [1]. Comparing the events of the sideband with sideband-subtracted signal and with the Monte Carlo events (Fig.6.3), we define the range within which we vary the variables values. Table 6.1 shows the different sets of variables that have been tested with the corresponding score-function value. At the end, the group of variables with the greater score-function is chosen.

We consider all the combinations within the selected N-dimensional space range (where N is the number of variables we are considering; in our case N = 5), then we choose the one for which we reach a maximum for the score-function. The $N-1$ plots that shows this procedure (Fig.6.4 and Fig.6.5) represent the value of the score-function as a function of the cuts of one certain variable and keeping at a fixed value all the other $N-1$ variables. The final cuts are reported in Table 6.2.

Concerning these optimized cuts it should be noticed that the most selective cut is the one on the transverse momentum of the kaon with less energy.
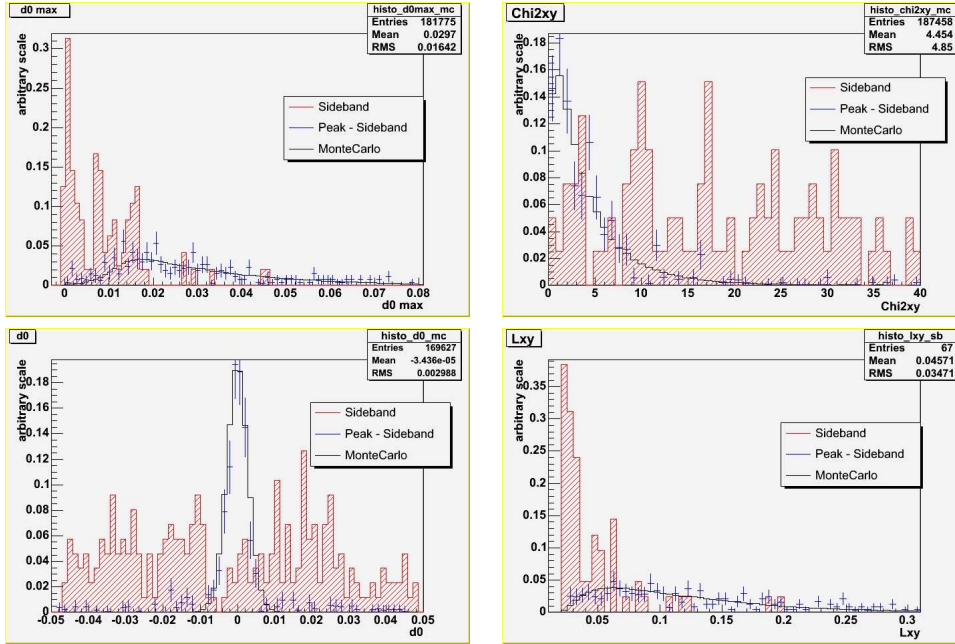
Figure 6.3: *Comparison of the events of sideband with sideband subtracted signal and the Monte Carlo for some distributions used in optimizing the $B_s \rightarrow \phi\phi$ signal.*
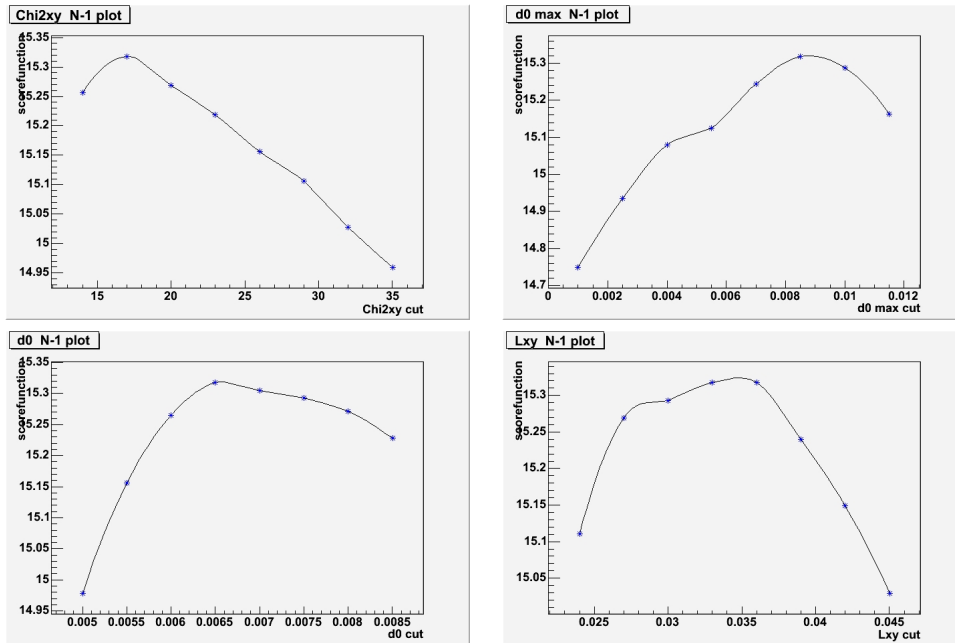
Figure 6.4: *Graphs that represent the value of the score-function as function of the cuts in the $B_s \rightarrow \phi\phi$ decay study.*

72

Variables	score-function
$d_0{}^B$, d_{0max}^{ϕ}, L_{xy}, χ_{xy}^2, $P_T^{\phi\ max}$	16.8 ± 0.5
$d_0{}^B$, ΔR, L_{xy}, χ^2, $P_T^{K\ min}$	16.5 ± 0.5
$d_0{}^B$, d_{0max}^{ϕ}, L_{xy}, χ_{xy}^2, $P_T^{K\ min}$	17.2 ± 0.6
$d_0{}^B$, d_{0max}^{ϕ}, L_{xy}, χ^2, $P_T^{\phi\ max}$	16.5 ± 0.5
$d_0{}^B$, d_{0max}^{ϕ}, L_{xy}, χ^2, $P_T^{K\ min}$	16.3 ± 0.5

Table 6.1: *Set of variables used in the score-function. $d_0{}^B$ is the impact parameter of the B meson, d_{0max}^{ϕ} is the impact parameter of the ϕ with highest energy, $p_T^{K\ min}$ is the transverse momentum of the kaon with lowest energy*
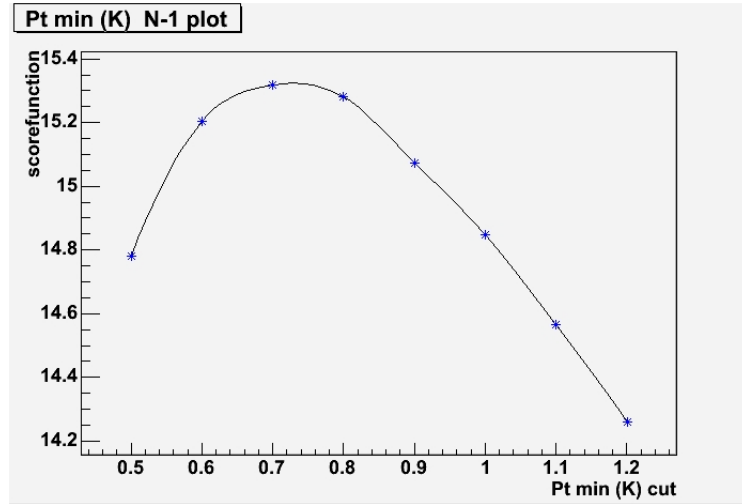
Figure 6.5: *Score-function as function of the transverse momentum of the kaon with lowest energy.*

Variable	Cut
L_{xy}	$> 330~\mu\text{m}$
$\text{P}_T^{K~min}$	$> 0.7~\text{GeV}/c$
χ_{xy}^2	< 17
d_0^B	$< 65~\mu\text{m}$
$d_0^{\phi}{}_{max}$	$> 85~\mu\text{m}$

Table 6.2: *Values of the final cuts obtained for the $B_s \to \phi\phi$ signal optimization.*

6.3.2 Selection of the signal for $B_s \to J/\psi\phi$

The cuts selection used to study this decay in [50] was optimized for a polarization measurement using a different score-function from $\frac{S}{\sqrt{S+B}}$. We decided to use the same variables of this previous analysis because they are very similar or related to those used in $B_s \to \phi\phi$.

On the other hand, to avoid possible systematic errors we perform an optimization procedure for the selection of the $B_s \to J/\psi\phi$ decay using the same score-function of the cuts optimization procedure used for the $B_s \to \phi\phi$ decay. In Figure 6.6 the $N-1$ plots for the $B_s \to J/\psi\phi$ decay are shown. The
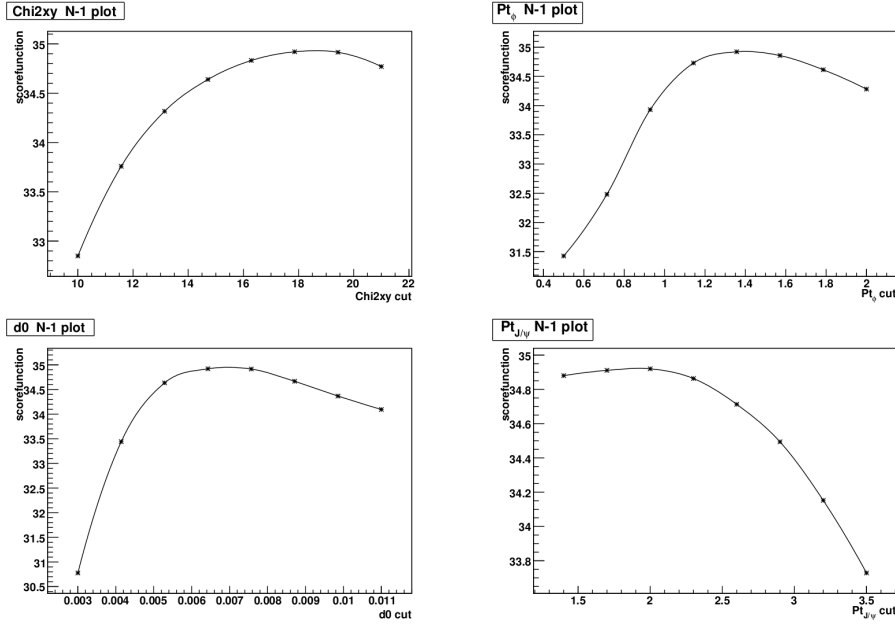
Figure 6.6: $N-1$ *plots of the score-functions as a function of the variable cuts for the $B_s \to J/\psi\phi$ decay. From top to bottom, left to right the variables are: the B_s meson χ_{xy}^2, the ϕ the transverse momentum, the B_s meson impact parameter, the J/ψ transverse momentum.*

74

final results are summarized in Tab.6.3.

Variable	Cut
L_{xy}	$> 290~\mu m$
P_T^ϕ	$> 1.36~\mathrm{GeV}/c$
$P_T^{J/\psi}$	$> 2.0~\mathrm{GeV}/c$
χ_{xy}^2	< 18
d_0^B	$< 65~\mu m$
confirmation of 1 muon	

Table 6.3: *Final decay cuts for $B_s \to J/\psi\phi$.*

The selection was optimized starting from the request of the identification of at least one muon in the $J/\psi \to \mu\mu$ decay. The choice to apply this cut allow us to obtain the best solution about the signal-to-background ratio and to exclude the background arising from the $J/\psi \to ee$ decay.
Without this request we obtained a substantial background component from $J/\psi \to ee$, while requiring a full identification for both the muons would have enabled us to get a signal with a very high purity but a relatively low number of selected events, as shown by Figure 6.7 and 6.8.
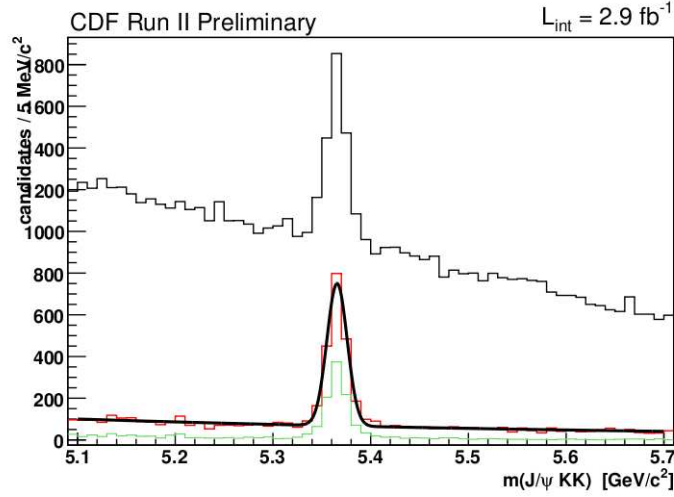
Figure 6.7: *Comparison of the B_s invariant mass distributions obtained requiring the identification of 0 (black), 1 (red) or 2 (green) muons.*

The optimization procedure was not as complete as the one for the $B_s \to \phi\phi$, because other possible sets of variables have not been evaluated. The events selected with the optimized cuts are shown in Figure 6.9. A clear signal is visible for both decay channels.
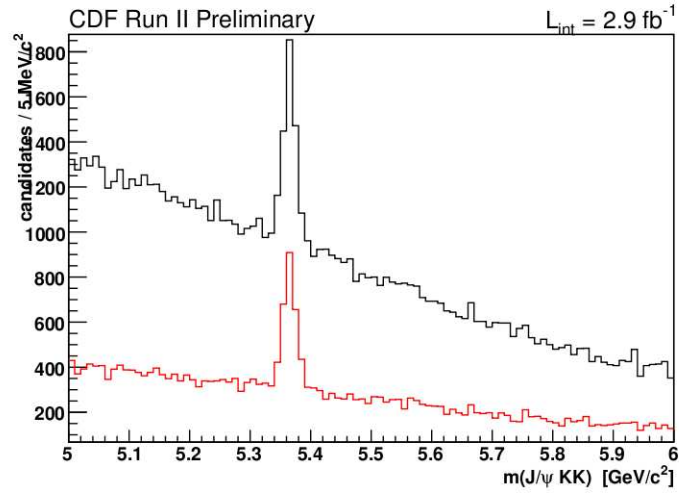
Figure 6.8: $J/\psi \to ee$ decays present in our sample, compared with the distribution without any lepton identification.
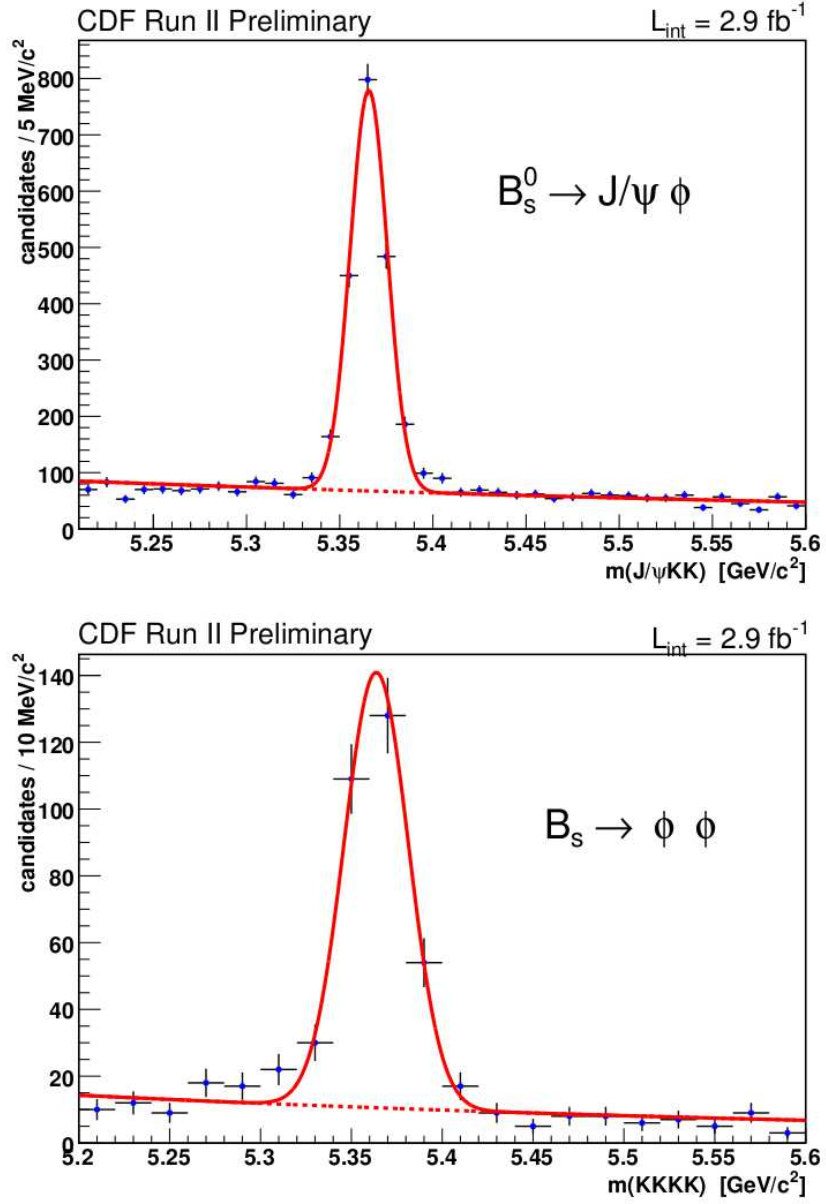
Figure 6.9: *Signals obtained with the optimized selections.*

6.4 The $B_s \to J/\psi\phi$ signal in the Two Tracks Trigger

The analysis of the $B_s \to J/\psi\phi$ channel at CDFII is performed using the trigger based on the request of two muons: the DI_MUON trigger. We want to investigate the overlap of the $B_s \to J/\psi\phi$ sample reconstructed in the TTT and the one using the DI_MUON trigger.
We add in the selection the request that events do not fire the DI_MUON trigger and use the same procedure that was used to determine the number of $B_s \to J/\psi\phi$ in our TTT sample.
The result is shown in Figure 6.10. Integrating the fitted gaussian function that parametrize the signal, we extract the number of $J/\psi\phi$ events:

$$N_{J/\psi\phi} = 1210 \pm 40 \tag{6.3}$$

The evaluation of this sample is particularly important as it could allows to increase the data sample used to perform some important analysis, such as the determination of the angles of unitary triangles or the $\Delta\Gamma_s$ measurement.
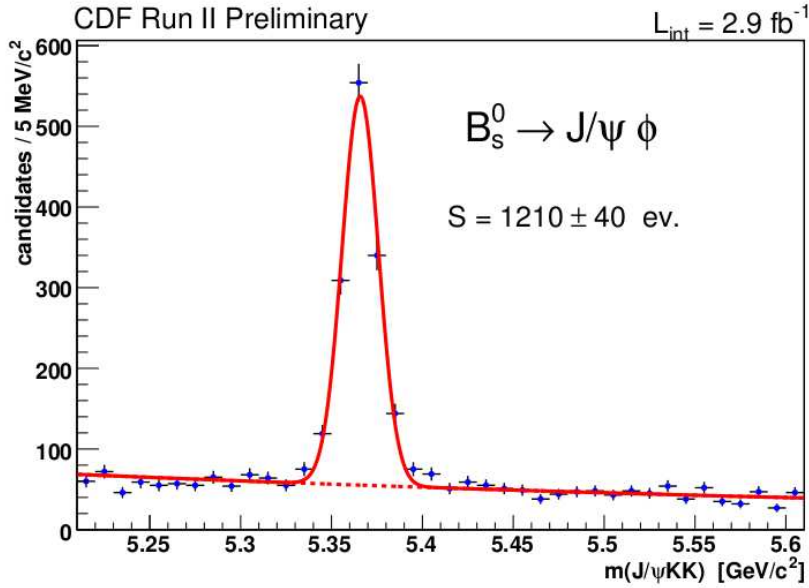
Figure 6.10: $B_s \to J/\psi\phi$ *events not triggered by the trigger-path* DI_MUON *but present in the TTT trigger-path*

Chapter 7

Branching Ratio measurement

This chapter presents the measurement of the Branching Ratio of $B_s \rightarrow \phi\phi$. Each variable present in the formula 6.1 is evaluated, namely the yield of the two signals and the trigger and selection efficiencies. In addition, all main systematic errors of this measurement are estimated.

7.1 Determination of the signal yields

The events number of the two signals $B_s \rightarrow \phi\phi$ and $B_s \rightarrow J/\psi\phi$ is extracted from the invariant mass distribution of reconstructed B_s meson distribution, obtained after applying the optimized selections and shown in Figure 7.7 and Figure 7.3 respectively.
In these distributions at least 3 components can be clearly recognized:

- **combinatorial background**. These are random combinations that produce a continuous invariant B_s mass distribution and are due to an incorrect assignment of tracks to the decay particles;

- **reflections of other decays**. Other B mesons decays can be reconstructed in a wrong way, and because of this they enter the B meson invariant mass distribution inside the mass window of the signal;

- **the signal** itself.

We evaluated the best parametrization of each component in the observed invariant mass distribution using the Monte Carlo simulation. Finally, a fit on the data was performed taking into account all the identified components. This allowed us to fix some parameters in the signal parametrization and then to make a global fit with a limited number of free parameters.
The measurement of the reconstructed number of signal events is performed by integrating the gaussian function used to parametrize the signal in the

mass window.

7.1.1 $B_s \to J/\psi\phi$ events

The combinatorial background and the reflections

The combinatorial background is certainly the most important contribution in this analysis within the considered mass window and its invariant mass distribution follows, with a good approximation, an exponentially decreasing behavior. In this case, we didn't perform a Monte Carlo study but a simple parametrization has been used instead.

The reflections are due to signal events reconstructed with a wrong mass assignment to one or two daughters particles of the B mesons. The more frequent decay that enters as a reflection in the invariant mass window of the $B_s \to J/\psi\phi$ decay is the $B_d \to J/\psi K^{*0}$ decay. It occurs when in the reconstruction of the $B_s \to J/\psi\phi$ decay, the daughter tracks of the $K^* \to K\pi$ decay are assumed to be two kaons and an incorrect invariant mass is computed.

Its distribution in the invariant mass of the $B_s \to J/\psi\phi$ can be parametrized in the Monte Carlo simulation using an asymmetric Gaussian and a decreasing exponential function expressed by:

for $x > \mu$:

$$
\begin{aligned}
R(x) = \quad & C \cdot \left(\frac{2}{1 + [(f_G \cdot \frac{1}{\sqrt{2\pi}\sigma_2} + (1 - f_G) \cdot \frac{b}{2}) \cdot \sqrt{2\pi}\sigma_1]} \right) \cdot \\
& \cdot \left(f_G \cdot \frac{1}{\sqrt{2\pi}\sigma_2} \cdot e^{-\frac{(x-\mu)^2}{2\sigma_2^2}} + (1 - f_G)\frac{b}{2} \cdot e^{-b(x-\mu)} \right)
\end{aligned} \tag{7.1}
$$

and for $x < \mu$:

$$
\begin{aligned}
R(x) = \quad & C \cdot \left((f_G \cdot \frac{1}{\sqrt{2\pi}\sigma_2} + (1 - f_G) \cdot \frac{b}{2}) \cdot \sqrt{2\pi}\sigma_1 \right) \cdot \\
& \cdot \left(\frac{2}{1 + [(f_G \cdot \frac{1}{\sqrt{2\pi}\sigma_2} + (1 - f_G) \cdot \frac{b}{2}) \cdot \sqrt{2\pi}\sigma_1]} \cdot \frac{1}{\sqrt{2\pi}\sigma_1} e^{-\frac{(x-\mu)^2}{2\sigma_1^2}} \right)
\end{aligned} \tag{7.2}
$$

The values obtained from the fit are presented in Table 7.1.

Figure 7.1 shows a comparison of the signal reflection and the $B_s \to J/\psi\phi$ decay, both simulated using Monte Carlo method, using an arbitrary normalization. The parameters of the fit show that this reflection has a distribution centered just below our signal.

The fraction of reflection with respect to the signal events, $f_{J/\psi K^*}$, is given by the following formula:

$$
f_{J/\psi K^*} = \frac{N(B_d \longrightarrow J/\psi K^{*0})}{N(B_s \longrightarrow J/\psi\phi)} =
$$
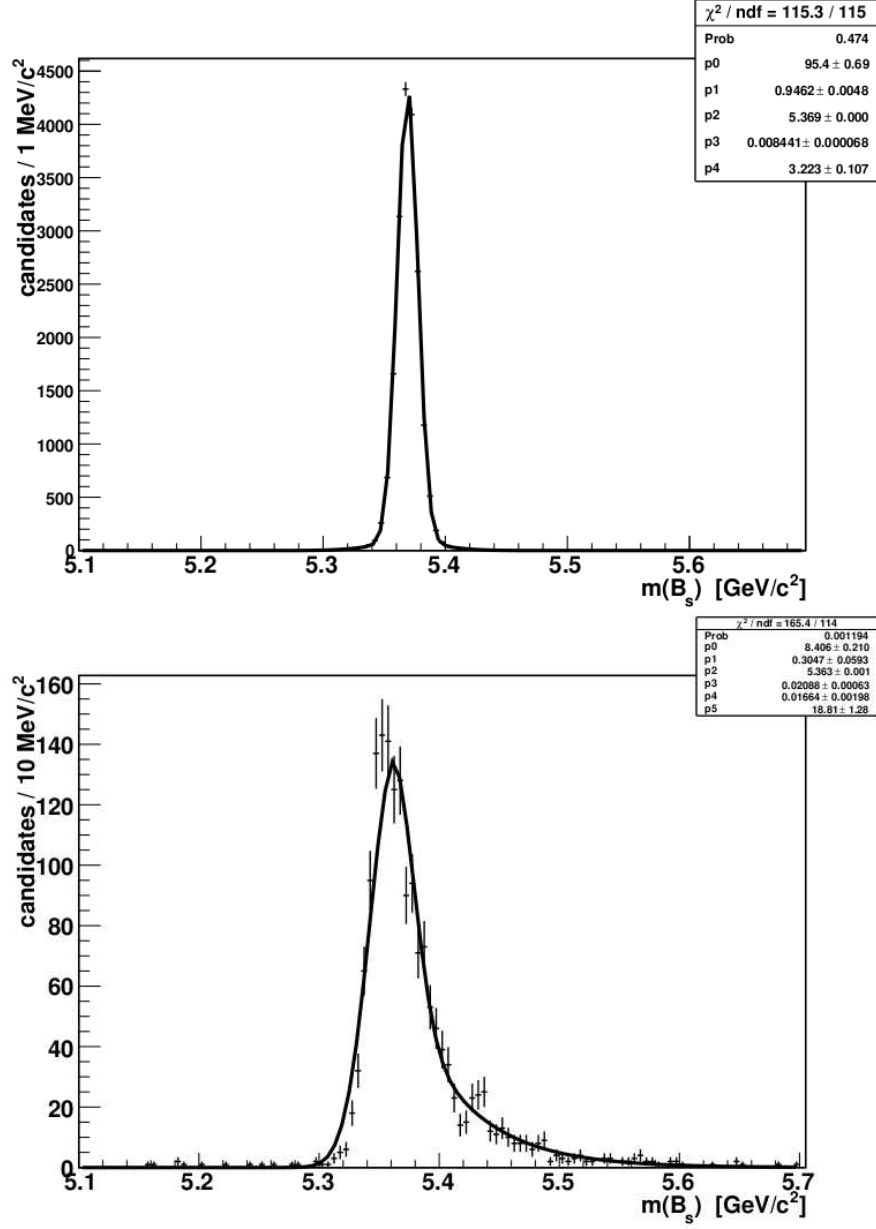
Figure 7.1: *Comparison between the simulated signal and the reflection. The signal is parametrized by two gaussians with different resolution; the reflection with an asymmetric Gaussian.*

parameter	value	error
C	8.41	0.20
f_G	0.305	0.058
μ	5.363	0.0014
σ_1	0.0209	0.0009
σ_2	0.016	0.002
b	18.8	1.2

Table 7.1: *Values of the fit for the reflection $B_d \rightarrow J/\psi K^*$ simulated with Monte Carlo, where C is the normalization constant, f_G the fraction of the Gaussian compared to the exponential, μ is the average of the distribution and σ_1, σ_2 are the two resolutions. b is the exponential parameter.*

$$= \frac{f_d}{f_s} \frac{BR(B_d \longrightarrow J/\psi K^{*0})}{BR(B_s \longrightarrow J/\psi \phi)} \frac{BR(K^* \longrightarrow K\pi)}{BR(\phi \longrightarrow K^+K^-)} \frac{\epsilon_{TOT}^{J/\psi K^*}(J/\psi\phi)}{\epsilon_{TOT}^{J/\psi\phi}} \qquad (7.3)$$

where $\epsilon_{TOT}^{J/\psi K^*}(J/\psi\phi)$ is the total efficiency of the $B_d \rightarrow J/\psi K^{*0}$ decays reconstructed as a $B_s \rightarrow J/\psi\phi$ one. The other parameters are extracted from the PDG [47] and f_d and f_s are the production fractions of the B_d and B_s mesons.
We obtain:

$$f_{J/\psi K^*} = 0.0419 \pm 0.0093$$

and it will be fixed in the global fit of our distribution.

The signal

The signal has a width of around 10 MeV and it is parametrized with two gaussian having the same average value but a different resolution (Figure 7.2). This choice is fairly standard and takes into account the detector effects that determines an additional spread in the tail distributions.
The function used to parametrize the distribution is the following:

$$G(x) = C_G \cdot f \frac{1}{\sqrt{2\pi}\sigma_1} \cdot e^{-\frac{(x-\mu)^2}{2\sigma_1^2}} + (1-f) \cdot \frac{1}{\sqrt{2\pi}\sigma_1 k} \cdot e^{-\frac{(x-\mu)^2}{2\sigma_1^2 k^2}} \qquad (7.4)$$

where C_G is a multiplicative normalization constant, f is the fraction of one gaussian component with respect to the other and k is a multiplicative factor of the resolution in the second Gaussian.
Fitting the Monte Carlo events of Figure 7.2 we obtained the parameters in Table 7.2.
In the fit of our data, the multiplicative factor k and the fraction f are fixed, while the mean value, the resolution, and the normalization constant are free parameters of the fit. A global maximum likelihood fit is then performed
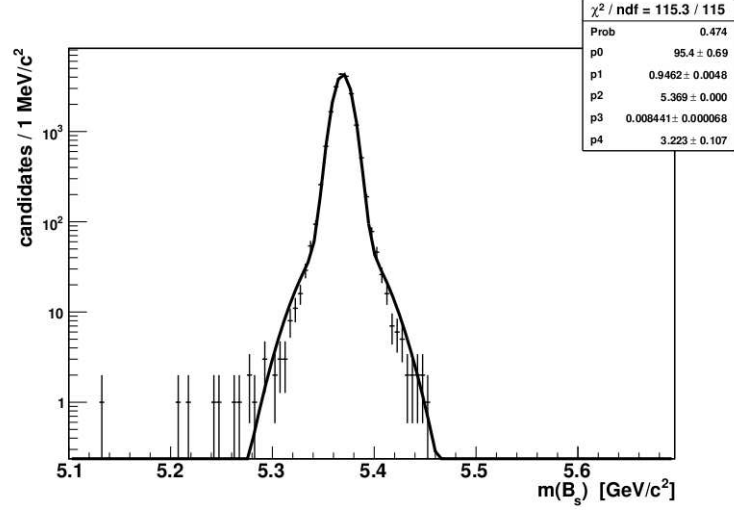
Figure 7.2: *Signal obtained with Monte Carlo simulation. The y axis is in logarithmic scale.*

parameter	value	error
C_G	95.40	0.70
f	0.9462	0.00486
μ	5.36913	0.00007
σ_1	0.00844	0.00007
k	3.22	0.11

Table 7.2: *Summary of the values obtained in the fit performed on the simulated signal.*

taking into account all the components described above; the function used to perform this fit is the following:

$$F(x) = C_{TOT}[\cdot frac \cdot \left(f \frac{1}{\sqrt{2\pi}\sigma_1} \cdot e^{-\frac{(x-\mu)^2}{2\sigma_1^2}} + (1-f) \cdot \frac{1}{\sqrt{2\pi}\sigma_1 3.2} \cdot e^{-\frac{(x-\mu)^2)}{2\sigma_1^2 * 10.24}} \right) +$$
$$(1 - frac) \cdot (1 - f_k) \frac{b}{e^{-bx}{}_{MAX} - e^{-bx}{}_{MIN}} e^{-bx} + (1 - frac) \cdot f_k \cdot R(x)]$$

where $R(x)$ is the function defined in equation 7.1 and 7.2, without the initial multiplicative factor C and where all other parameters are fixed. We have $f_k = \frac{frac \cdot f_{J/\psi K^*}}{1 - frac}$, where $frac$ is the fraction of signal events compared to the total number of events N_{TOT} present in the histogram of Figure 7.3.

The number of events are:

$$N_{B_s \rightarrow J/\psi\phi} = frac \cdot n_{TOT} = 1766 \pm 39(stat) \tag{7.5}$$
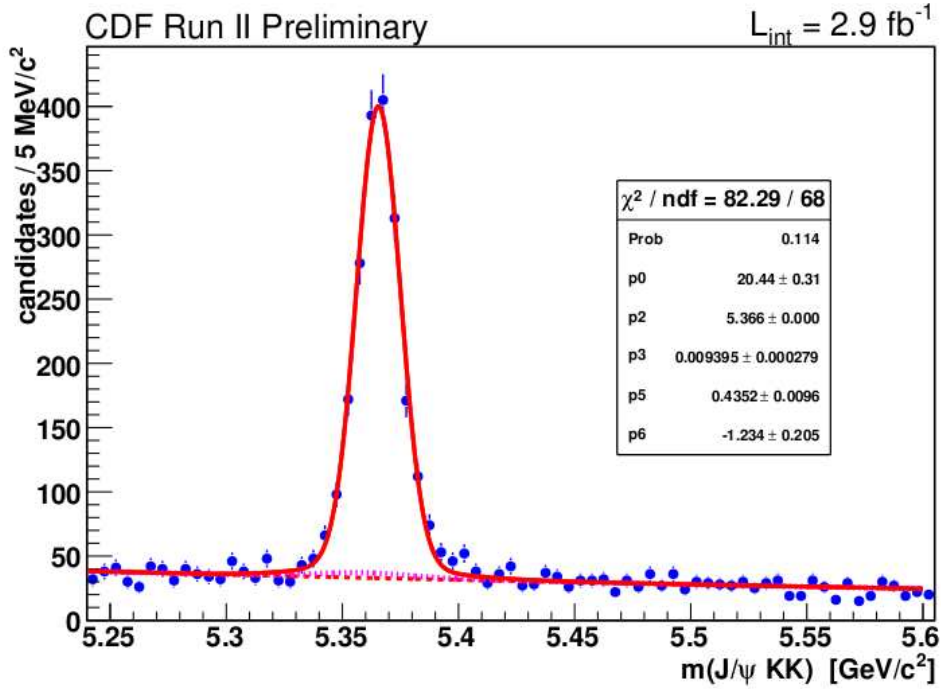
Figure 7.3: *Overall fit of the $B_s \rightarrow J/\psi\phi$ signal. Red dashed: parametrization of the combinatorial background with a decreasing exponential. Pink dashed: the reflection of the $B_d \rightarrow J/\psi K^*$ decay. The signal is parametrized with two gaussian having the same mean value but different resolutions.*

7.1.2 $B_s \to \phi\phi$ events

The combinatorial background and the reflections

As for the $B_s \to J/\psi\phi$ decay, in this case the combinatorial background is certainly the most important background inside the mass window and is well parametrized using a decreasing exponential function.

In this case, the decays that could create reflections in the B_s mass window are:

$$B_d \to \phi K^* \to KKK\pi$$
$$B_s \to \bar{K}^* K^* \to \bar{K}\pi^- K\pi^+$$

These are due to the incorrect reconstruction of a K^* as a ϕ, because as shown in Figure 7.4 a tail of the invariant mass distribution of tracks of the K^* decay, reconstructed as m_{KK}, is present within the ϕ invariant mass window. This implies the presence of a contribution of the $B_d \to \phi K^*$ signal in the region $m_{B_s} \pm 3\sigma_{B_s}$. We can estimate their contributions using the following formulas:

$$N(B_d \to \phi K^*) = \frac{f_d}{f_s} \frac{BR(B_d \to \phi K^*)}{BR(B_s \to J/\psi\phi)} \frac{BR(K^* \to K\pi)}{BR(J/\psi \to \mu\mu)} \frac{\epsilon_{TOT}^{\phi K^*}(\phi\phi)}{\epsilon_{TOT}^{J/\psi\phi}} N(B_s \to J/\psi\phi)$$
(7.6)

$$N(B_s \to \overline{K^*}K^*) = \frac{BR(B_s \to \overline{K^*}K^*)}{BR(B_s \to J/\psi\phi)} \frac{BR(K^* \to K\pi)}{BR(J/\psi \to \mu\mu)} \frac{BR(K^* \to K\pi)}{BR(\phi \to KK)}$$

$$\cdot \frac{\epsilon_{TOT}^{\overline{K^*}K^*}(\phi\phi)}{\epsilon_{TOT}^{J/\psi\phi}} N(B_s \to J/\psi\phi)$$
(7.7)

where $\epsilon_{TOT}^{\phi K^*}(\phi\phi)$ and $\epsilon_{TOT}^{\bar{K}^*K^*}(\phi\phi)$ are respectively the total efficiency of the $B_d \to \phi K^*$ decay and of the $B_s \to \bar{K}^* K^*$ decay reconstructed as $B_s \to \phi\phi$. These efficiencies are estimated using the Monte Carlo simulation.

The number of $B_s \to J/\psi\phi$ events is taken from the calculation made in 7.5 that is $N(B_s \to J/\psi\phi) = 1766 \pm 39$.

The fraction of events is calculated with respect to the number of events of $B_s \to J/\psi\phi$, and not using explicitly the number of $B_s \to \phi\phi$ events. Otherwise, we would need to use the Branching Ratio of $B_s \to \phi\phi$ in the formula, which is actually the aim of our measurement.

The number of reflections events is obtained by the relations 7.6 and 7.7 and it is shown in Table 7.3. The errors on the number of events were obtained by summing in quadrature the errors of all the contributions.

Since the reconstruction efficiency of the $B_s \to \bar{K}^* K^*$ as a $B_s \to \phi\phi$ is very low in the B_s mass window, we neglected its contribution in our analysis. The parametrization of the $B_d \to \phi K^*$ reflection has been studied with the
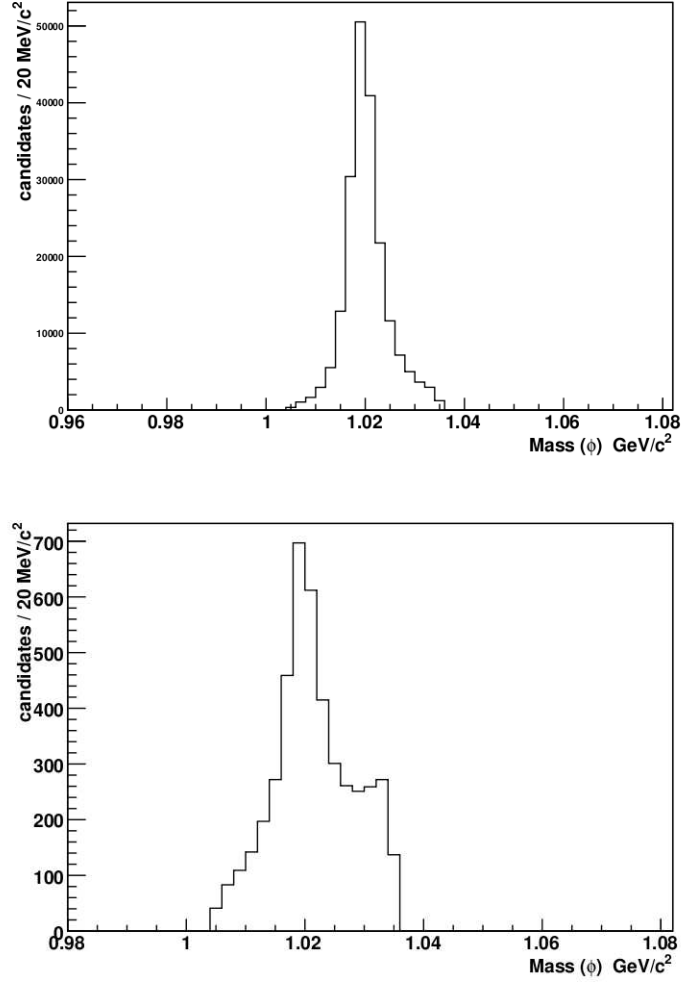
Figure 7.4: *On bottom: the invariant mass distribution of the ϕ reconstructed from the $B_d \to \phi K^*$ decays. On top: mass distribution of the ϕ of $B_s \to \phi\phi$ decays. In both graphs, the events are taken in the peak region of the B meson and are simulated using Monte Carlo.*

Reflection	total efficiency	total number of events
$B_s \to \bar{K}^* K^*$	$\sim 10^{-6}$	0
$B_d \to \phi K^*$	0.000134 ± 0.000002	8 ± 3

Table 7.3: *Number of events and efficiencies of the reflections for the $B_s \to \phi\phi$ decay in the data sample. Because the reflection $B_s \to \bar{K}^* K^*$ have a negligible efficiency it is not considered in our analysis.*

86

Monte Carlo simulation. We implement a fit with an asymmetrical gaussian and an exponentially decreasing function given by equation 7.1 and 7.2. The fit is shown in Fig.7.5 and its parameters are summarized in Table 7.4.
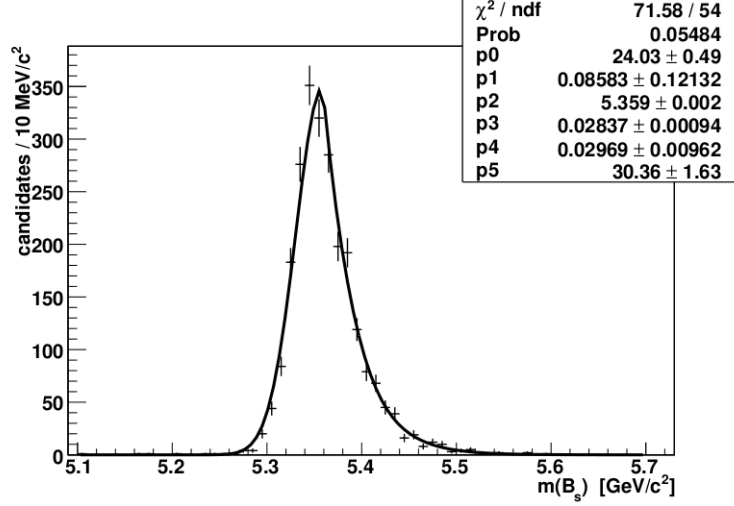
Figure 7.5: *Distribution of events of $B_d \to \phi K^*$ which pass the selection for the reconstruction of the decay $B_s \to \phi\phi$.*

parameter	value	error
C	24.03	0.49
f_G	0.086	0.121
μ	5.359	0.002
σ_1	0.0284	0.0009
σ_2	0.030	0.010
b	30.4	1.6

Table 7.4: *Values obtained performing the fit of the reflection $B_d \to \phi K^*$.*

The signal

The signal has a width of around 20 MeV and, as for the $B_s \to J/\psi\phi$, it was parametrized using two gaussian having the same mean value but different resolutions (equation 7.4). The fit parameters obtained on the Monte Carlo sample (Figure 7.6) are presented in Table 7.5.

In the overall fit, the relative fractions of events in one gaussian with respect to the other and the multiplicative factor of the second Gaussian resolution is fixed.

χ^2 / ndf	1245 / 295
Prob	0
p0	456.5 ± 1.0
p1	0.9429 ± 0.0014
p2	5.37 ± 0.00
p3	0.01594 ± 0.00004
p4	3.126 ± 0.029

χ^2 / ndf	1245 / 295
Prob	0
p0	456.5 ± 1.0
p1	0.9429 ± 0.0014
p2	5.37 ± 0.00
p3	0.01594 ± 0.00004
p4	3.126 ± 0.029
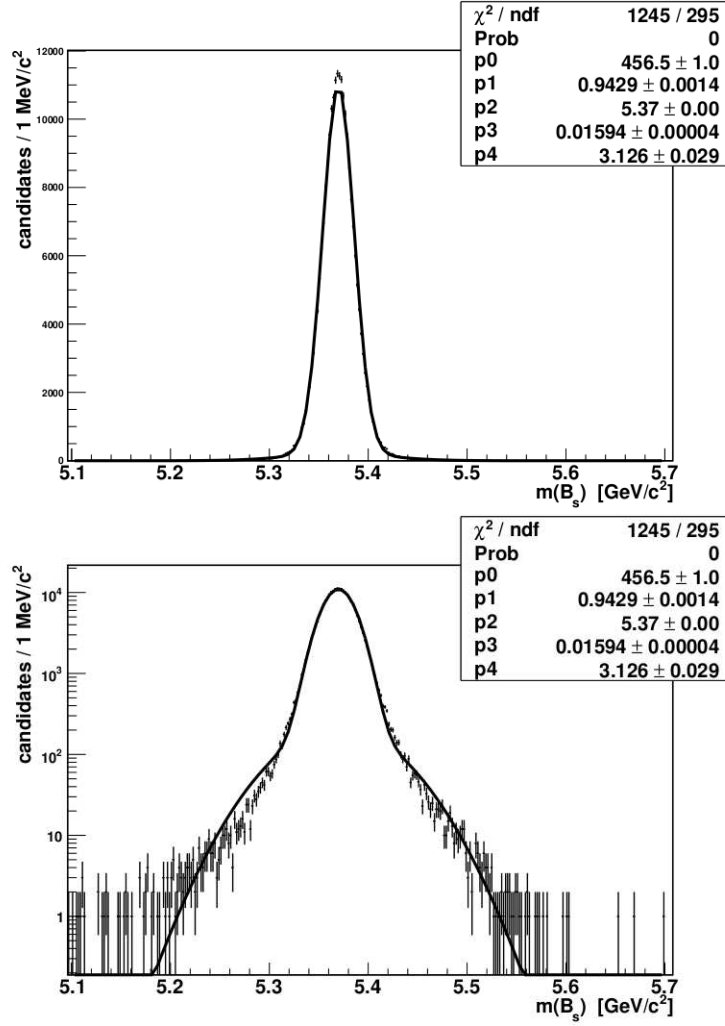
Figure 7.6: *Invariant mass distribution of the $B_s \to \phi\phi$ simulated with Monte Carlo, in linear (top) and logarithmic scale(bottom).*

Parameter	value	error
C_G	456.5	1.0
f	0.9429	0.0014
μ	5.36994	0.00004
σ_1	0.015941	0.00004
k	3.13	0.03

Table 7.5: *Summary of the values of the fit performed on the $B_s \to \phi\phi$ signal simulated using Monte Carlo methods.*

We performed a global maximum likelihood fit that takes into account all the signal and background components (equation 7.1.1). Since it is a maximum likelihood fit on a low statistics set, to avoid to underestimate the errors, the number of signal events is extracted from the fraction $frac$, multiplying it by the total number of events present in the histogram of Figure 7.7.
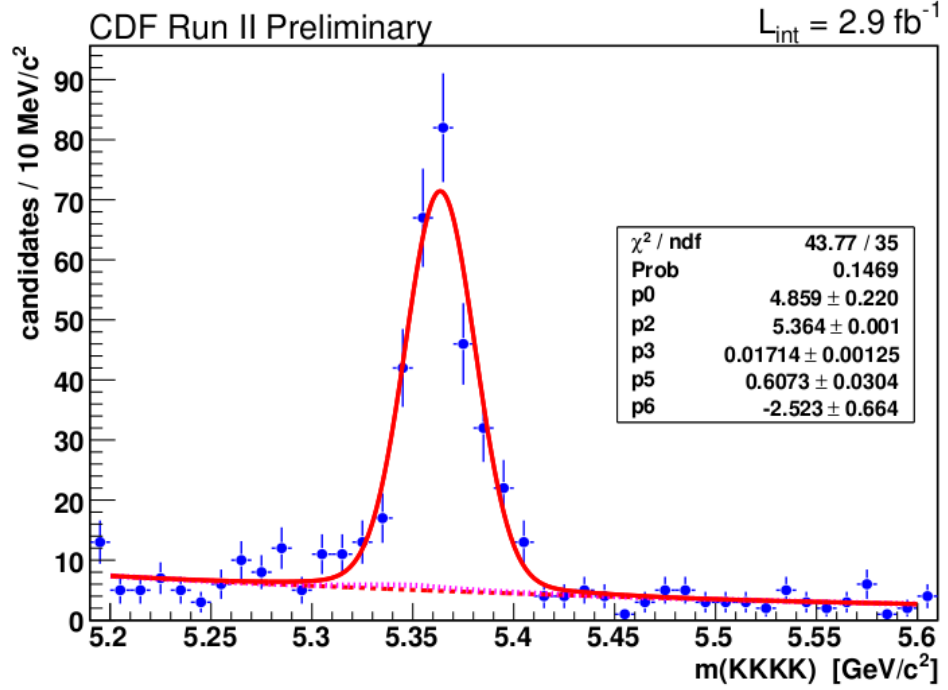
Figure 7.7: *Global fit which takes into account all the identified signal and background elements. The red dashed line is the parametrization of the combinatorial background; the pink dashed line shows instead the small contribution (8 events) of the $B_s \rightarrow \phi K^*$ reflection. The signal was parametrized using two gaussian having the same average but a different resolution.*

So we obtain that the number of signal events in the $B_s \rightarrow \phi\phi$ decay are:

$$N_{B_s \rightarrow \phi\phi} = 295 \pm 15(stat) \tag{7.8}$$

7.2 Trigger and selection efficiencies

The trigger and selection efficiencies are determined using the Monte Carlo simulation and evaluating the ratio between the number of generated events and the number of events that satisfy the various trigger and selection criteria, with the same set of cuts used for the signal selection in the data.
Because the Monte Carlo is not able to simulate the various prescale factors of the different triggers, we have to weight the efficiencies by a factor that takes this effect into account. Thus, the total efficiency is given by the relation:

$$\epsilon_{TOT} = \sum_i p_i \epsilon_i \tag{7.9}$$

where p_i and ϵ_i are, respectively, the prescale factor and the efficiencies of each exclusive trigger (in our case of $HIGHPT$, $ScAnoHIGHPT$ and $LOWPTnoScAnoHIGHPT$). The fraction of data selected by a particular trigger is computed by $f_i = \frac{p_i \epsilon_i}{\epsilon_{TOT}}$.

The prescale factors p_i (which are the same for the two decays because we study them on the same data sample) are determined using the trigger fractions f_i and the trigger efficiencies evaluated using the sample $B_s \rightarrow J/\psi\phi$. This procedure reduces the error on the efficiencies ratio that would otherwise be dominated from the error on the fraction of $B_s \rightarrow \phi\phi$ events, due to the low statistics of this decay in our sample.

For what concerns the total efficiency of the selection of $B_s \rightarrow J/\psi\phi$, the Monte Carlo is not reliable for the simulation of the muon efficiency. The systematic effects associated with the triggers and the decay selection as simulated by the Monte Carlo cancel out in the ratio with those for the $B_s \rightarrow \phi\phi$, while this does not happen for the muon systematics. Furthermore the Monte Carlo contains no details on the status of the muon chambers such as the status of active detectors or dead channels present during the data acquisition. For this reason we evaluate the total efficiency for the $B_S \rightarrow J/\psi\phi$ as the product of an efficiency, evaluated with the Monte Carlo, and another one for the muon request that is evaluated separately on the data, i.e.

$$\epsilon_{TOT}^{J/\psi\phi} = \epsilon_{RIC}^{J/\psi\phi} \cdot \epsilon_\mu$$

The fractions of the different triggers are presented in Tables 4.1 and 4.2. The results of the trigger and selection efficiencies for exclusive triggers are summarized in Tables 7.6 and 7.7. The error in this case is computed as the error of a binomial function.

The final relation used to evaluate the efficiencies of $B_s \rightarrow J/\psi\phi$ is:

$$\epsilon_{RIC}^{J/\psi\phi} = p_{HIGHPT} \cdot \frac{\epsilon_{HIGHPT}^{J/\psi\phi}}{f_{HIGHPT}^{J/\psi\phi}} \tag{7.10}$$

Exclusive trigger	ϵ_i
$HIGHPT$	0.003500 ± 0.000042
$ScAnoHIGHPT$	0.002533 ± 0.000036
$LOWPTnoScAnoHIGHPT$	0.004238 ± 0.000046
All	0.010271 ± 0.000071

Table 7.6: *Trigger efficiencies of the $B_s \to J/\psi\phi$ decay divided by the different exclusive triggers.*

Exclusive trigger	ϵ_i
$HIGHPT$	0.003632 ± 0.000013
$ScAnoHIGHPT$	0.002857 ± 0.000012
$LOWPTnoScAnoHIGHPT$	0.004980 ± 0.000016
All	0.011468 ± 0.000024

Table 7.7: *Trigger efficiencies for $B_s \to \phi\phi$ decay divided by the different exclusive triggers.*

and the one used for $B_s \to \phi\phi$ can be extracted from 7.9 and it is

$$\epsilon_{TOT}^{\phi\phi} = p_{HIGHPT} \cdot \sum_i \frac{p_i}{p_{HIGHPT}} \epsilon_i \tag{7.11}$$

where $\frac{p_i}{p_{HIGHPT}}$ are extracted from the $J/\psi\phi$ sample using the following relation:

$$\frac{p_i}{p_{HIGHPT}} = \frac{\epsilon_{HIGHPT}^{J/\psi\phi} \cdot f_i^{J/\psi\phi}}{\epsilon_i^{J/\psi\phi} \cdot f_{HIGHPT}^{J/\psi\phi}}$$

The final result of the ratio of the efficiencies is

$$\frac{\epsilon_{RIC}^{J/\psi\phi}}{\epsilon_{TOT}^{\phi\phi}} = \frac{\frac{\epsilon_{HIGHPT}^{J/\psi\phi}}{f_{HIGHPT}^{J/\psi\phi}}}{\epsilon_{HIGHPT}^{\phi\phi} + \frac{\epsilon_{HIGHPT}^{J/\psi\phi} \cdot f_{LOWPT}^{J/\psi\phi}}{\epsilon_{LOWPT}^{J/\psi\phi} \cdot f_{HIGHPT}^{J/\psi\phi}} \cdot \epsilon_{LOWPT}^{\phi\phi} + \frac{\epsilon_{HIGHPT}^{J/\psi\phi} \cdot f_{ScA}^{J/\psi\phi}}{\epsilon_{ScA}^{J/\psi\phi} \cdot f_{HIGHPT}^{J/\psi\phi}} \cdot \epsilon_{ScA}^{\phi\phi}}$$

$$= 0.906 \pm 0.030$$

The efficiency for the $B_s \to \phi\phi$ decay is greater than the $B_s \to J/\psi\phi$ one.

7.3   Muon efficiency

As explained in the previous paragraph, the efficiency of the signal selection for $B_s \to J/\psi\phi$ was divided into a trigger and selection efficiency (implemented with the Monte Carlo) and the efficiency on the request of the presence of the muon, which is estimated on the data.

The request on the muons for the channel $B_s \to J/\psi\phi$ is that the J/ψ candidates have at least one of the two tracks with a match in the muon detectors.

This was implemented using the *HasMuon* flag of the Bstntuples. For this reason, it is necessary to estimate the efficiency of this request, ϵ_{mu}^{TOT}, which is a fundamental ingredient in the estimate of the total efficiency for the decay $B_s \rightarrow J/\psi\phi$.

The efficiency of the muon selection must be weighted with the p_T muon spectrum, simulated by the Monte Carlo and with no request for the identification of muons.

Efficiency of requiring the *HasMuon* flag

We choose to evaluate the efficiency on a sample of $J/\psi \rightarrow \mu\mu$ collected with the Two Tracks Trigger and originating from the primary vertex to avoid effects due to the reconstruction of the $B_s \rightarrow J/\psi\phi$. Using data from the TTT guarantees to be under the same trigger prescale conditions and to use the same goodrun list as the one used for our measurement (these conditions would not be satisfied using the *DI_MUON* trigger).

First, we have imposed a cut on the transverse decay length ($L_{xy} > 200\mu m$) in order to reduce the huge combinatorial background. The plot of the J/ψ invariant mass obtained after this selection is shown in Figure 7.8.
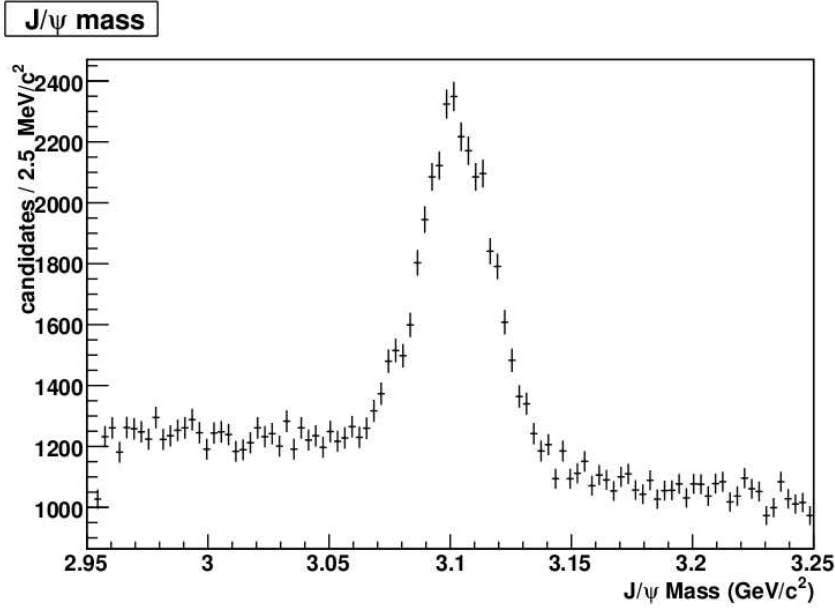
Figure 7.8: *Invariant mass distribution of the J/ψ after preliminary cuts.*

The efficiency of the request of at least one muon, ϵ_μ, was studied as a function of the muon p_T and in two ranges of pseudorapidity η. We obtained two histograms showing the efficiency ϵ_μ as a function of the muon p_T, one for CMU ($0.6 < | \eta | < 1.0$) and the other for CMX ($0.6 < | \eta | < 1.0$). In this way, we can estimate the efficiency as a function of p_T and η of the muon.

The efficiency as a function of p_T was calculated by dividing, bin by bin, two histograms of the p_T distribution for muon events with the request of at least one muon or two muons detected and using the following formula [51]:

$$\epsilon_\mu = \frac{N_{2\mu}}{N_{2\mu} + N_{1\mu}} \qquad (7.12)$$

where $N_{1\mu}$ and $N_{2\mu}$ are, respectively, the number of events that have only one muon and two muons.

The formula used to evaluate the error is:

$$\sigma_\epsilon = \frac{[\sigma_{N_{2\mu}}^2 (1 - \epsilon)^2 + \sigma_{N_{1\mu}}^2 \cdot \epsilon^2]^{1/2}}{N_{2\mu} + N_{1\mu}} \qquad (7.13)$$

where $\sigma_{N_{2\mu}}$ and $\sigma_{N_{1\mu}}$ are the errors evaluated from the sum in quadrature of the errors of the sidebands region and the peak region.

Actually, the used histograms are sideband subtracted. We use as sidebands the interval $[2.985, 3.015] \cup [3.185, 3.215]$ GeV/c^2 of the invariant J/ψ mass and for the peak region we considere the range of $\pm 3\sigma$ around the signal, i.e. $[3.072, 3.132]$ GeV/c^2. Then we parametrize the efficiency as a function of p_T for the distributions obtained for the CMU and CMX detectors (see Figure 7.9) with a sigmoid function:

$$\epsilon = \frac{A}{1 + e^{B(p_T + C)}} \qquad (7.14)$$

The values of the parameters extracted from the fit are presented in Tab.7.8.

parameters for CMU	
A	0.7534 ± 0.0034
B	3.762 ± 0.149
C	-1.86 ± 0.01
parameters for CMX	
A	0.6242 ± 0.00063
B	3.134 ± 0.188
C	-2.142 ± 0.020
average parameters	
A	0.7162 ± 0.0030
B	3.581 ± 0.112
C	-1.942 ± 0.011

Table 7.8: *Parameters values of the sigmoid evaluated performing the fit of the efficiencies distributions as a function of p_T.*
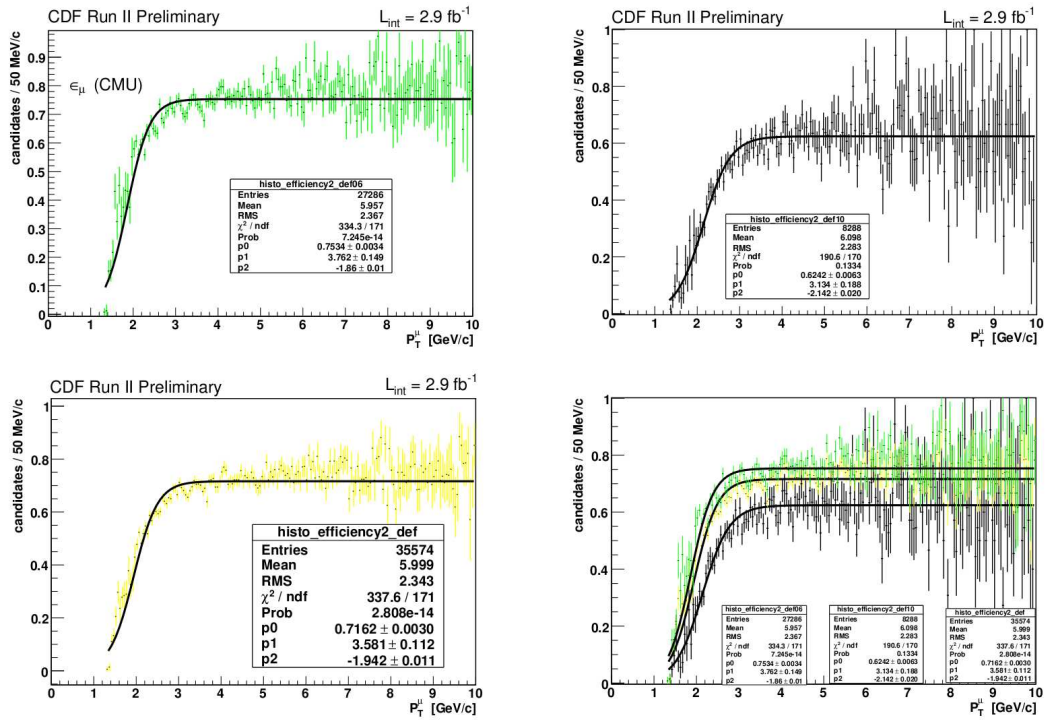
Figure 7.9: *Efficiencies as a function of the transverse momentum of the muon. Top: the distributions for CMU and CMX. Bottom left: the average on the two detectors. Bottom right: comparison between the three distributions (divided by muon detector and the mean value). These distributions are all fitted using a sigmoid function.*

The total efficiency

We are interested in estimating the overall efficiency of the muon request. For this reason, the muon efficiency ϵ_μ is reweighted as a function of the p_T muon spectrum obtained from the Monte Carlo sample of $B_s \to J/\psi\phi$ that does not require the identification of a muon. We obtain the total efficiency of the muon selection in the J/ψ decay with the following relation:

$$\epsilon_{\mu i}^{TOT} = \epsilon(p_{t1})_i \cdot [1 - \epsilon(p_{t2})_i] + \epsilon(p_{t2})_i \cdot [1 - \epsilon(p_{t1})_i] + \epsilon(p_{t1})_i \cdot \epsilon(p_{t2})_i \quad (7.15)$$

where $(p_{t1,2})_i$ are the transverse momenta of the two muonic tracks in the decay of the i-th J/ψ candidate.
Then calculating the average over all the J/ψ candidates in the Monte Carlo sample of $B_s \to J/\psi\phi$ we obtain the final result:

$$\epsilon_\mu^{TOT} = 0.8271 \pm 0.0033(stat)$$

In the systematic errors estimate, the effect of using a parametrization that takes into account the dependence of ϵ from η as well will be computed.

7.4   Systematic errors

This section lists and describes the main systematic effects that we consider for determining the uncertainty on the Branching Ratio.
These are:

- uncertainties on the number of events derived from the fit due to:

  - the variation in the fit mass range;
  - the parametrization of the background with one or two gaussian function.

- uncertainties on the background subtraction;

- uncertainty on the muon efficiencies;

- uncertainty on the ratio of trigger and selection efficiencies due to effects not considered in the Monte Carlo simulation, such as:

  - the polarization of $B_s \to J/\psi\phi$ and $B_s \to \phi\phi$;
  - the limited range of data taking runs implemented in the simulation;
  - the range of p_T;
  - the effect of the different particles types involved in the final states $\mu\mu KK$ and $KKKK$ related to the XFT efficiency.

95

- uncertainty due to the Branching Ratio of the normalization channel.

Not all of these effects have been evaluated yet; the used strategy for the ones we have computed is presented below.

Systematic uncertainty on the number of events
The first systematic is that due to the change in the fit mass range. The range used to fit over the signal is, respectively, [5.20, 5.60] GeV/c^2 for the $B_s \to \phi\phi$ and [5.23, 5.60] GeV/c^2 for the $B_s \to J/\psi\phi$. The choice of the upper limit is made considering the presence of possible reflections of the Λ_b that we do not know well enough, while the lower limit at 5.2 GeV/c^2 is due to the presence of other partially reconstructed decays for lower values of invariant mass. It was chosen to put a different threshold for the two decays due to the fact that the fit for the $B_s \to J/\psi\phi$ decay has the mass constraint. This systematic error evaluation is performed by varying the lower limit of the fit range.
The systematic errors are: $\Delta N_{\phi\phi} = 9$ and $\Delta N_{J/\psi\phi} = 7$.
    The second effect concerns the systematic error that arise from the use of a signal parametrization with a Gaussian instead of two with the same mean value and a different resolution. In this case the bias is calculated from the difference in the number of events as obtained by the two parametrizations and we obtain: $\Delta N_{\phi\phi} = 8$ e $\Delta N_{J/\psi\phi} = 41$.
The overall uncertainties that take into account these two effects and enter into the determination of the number of events are: $\Delta N_{\phi\phi}(syst) = 17$ e $\Delta N_{J/\psi\phi}(syst) = 48$.

The uncertainties on the background subtraction are essentially due to the error in quantifying the number of events of the reflections in the fit. The dominant contributions on this error come from the error on the Branching Ratio of $B_s \to J/\psi\phi$ and on the ratio of $\frac{f_s}{f_d}$, leading to a variation of 38% in the background subtraction. The obtained systematic errors are: $\Delta N_{\phi\phi} = 2$ e $\Delta N_{J/\psi\phi} = 13$.

The systematic uncertainty on ϵ_μ. The effect of using a parametrization as a function of the pseudorapidity as well has been estimated. The differences between the obtained result and that using the average parametrization give the final results [53]:

$$\epsilon_\mu^{TOT} = 0.8271 \pm 0.0033(stat) \pm 0.0075(syst)$$

Uncertainty on the trigger and selection efficiencies ratios due to effects not considered in the Monte Carlo simulation. The only effect examined so far is the one due to the polarizations of the $B_s \to \phi\phi$ and $B_s \to J/\psi\phi$ decays. In the used Monte Carlo, the polarizations were set in such a way

that all the final states have the same probability. To study the systematic effect of this assumption, we used in the Monte Carlo for the $B_s \rightarrow J/\psi\phi$ decay the measured polarization, while for the $B_s \rightarrow \phi\phi$ decay we used the polarization values of the very similar decay $B_d \rightarrow \phi K^*$ [49]. The obtained difference between the efficiencies with the two values of polarization gives the systematic error.

The final efficiencies are therefore:

$$\epsilon_{HIGHPT}^{\phi\phi} = 0.003632 \pm 0.000015(stat) \pm 0.00022(syst)$$

$$\epsilon_{HIGHPT}^{J/\psi\phi} = 0.003500 \pm 0.000046(stat) \pm 0.00021(syst)$$

7.5   Measurement of the Branching Ratio

In this chapter, we have evaluated all the numbers that enter the formula 6.1 to calculate the Branching Ratio. The other needed values are taken from the PDG [47].

Thus, the result for the ratio between the two Branching Ratio is:

$$\frac{BR(B_s \longrightarrow \phi\phi)}{BR(B_s \longrightarrow J/\psi\ \phi)} = 0.0143 \pm 0.0009(stat) \pm 0.0017(syst)$$

The value of the Branching Ratio of $B_s \rightarrow J/\psi\phi$ in the PDG is a CDF measurement where the value $\frac{f_s}{f_d} = 0.40 \pm 0.06$ was used, while the current value is $\frac{f_s}{f_d} = 0.28 \pm 0.04$. Because $B_s \rightarrow J/\psi\phi$ is proportional to $(\frac{f_s}{f_d})^{-1}$, we reweight the value of $B_s \rightarrow J/\psi\phi$ for $\frac{f_s}{f_d}_{CDF} \cdot \frac{f_d}{f_s}_{PDG}$.

The final result thus obtained is:

$$BR = [2.04 \pm 0.13(stat) \pm 0.24(syst) \pm 0.69(BR)] \cdot 10^{-5}$$

The statistical error, the systematic error and the one that depends on the error of the BR of $B_s \rightarrow J/\psi\phi$ are presented separately; it can be appreciated that the last error is the dominant one. When a new measurement of the BR of $B_s \rightarrow J/\psi\phi$ (by the Belle experiment or by CDFII) will be published, then it will be possible to improve the error on the BR of $B_s \rightarrow \phi\phi$.

The final measurement is consistent with the theoretical prediction [52] and with the previous result obtained with a statistic of only 8 events of the $B_s \rightarrow \phi\phi$ decay.

Chapter 8

Conclusions

In this thesis we studied the $B_s \to \phi\phi$ and $B_s \to J/\psi\phi$ decays using a sample of $2.9 fb^{-1}$ collected using the Two Track Trigger in CDFII since 2002 until April 2008.

The signals yields determination and the Branching Ratio measurement of the $B_s \to \phi\phi$ normalized to the $B_s \to J\psi\phi$ decay have been performed.

The Branching Ratio is evaluated using the following relation:

$$\frac{BR(B_s \to \phi\phi)}{BR(B_s \to J/\psi\phi)} = \frac{N_{\phi\phi}}{N_{J/\psi\phi}} \frac{\epsilon_{TOT}^{J/\psi\phi}}{\epsilon_{TOT}^{\phi\phi}} \frac{BR(J/\psi \to \mu\mu)}{BR(\phi \to KK)} \epsilon_\mu^{TOT} \tag{8.1}$$

where $\frac{\epsilon_{TOT}^{J/\psi\phi}}{\epsilon_{TOT}^{\phi\phi}} = 0.906 \pm 0.030$ is obtained from Monte Carlo simulation. $\epsilon_\mu^{TOT} = 0.8271 \pm 0.0033$ is evaluated using the p_T muon spectra on Monte Carlo generated $B_s \to J/\psi\phi$ events while the efficiencies functions are evaluated using a $J/\psi\phi \to \mu\mu$ data sample in the TTT.

The number of events obtained in the two decays channels are:

$$N_{\phi\phi} = 296 \pm 15$$
$$N_{J/\psi\phi} = 1766 \pm 39$$

The final measurement we obtain is:

$$\frac{BR(B_s \to \phi\phi)}{BR(B_s \to J/\psi\phi)} = [143 \pm 9(stat) \pm 17(syst)] \cdot 10^{-4}$$

from which, using the Branching Ratio of $B_s \to J/\psi\phi$ [47], modified according to the updated measurements of the ratio of production cross section of B_s and B_d mesons, we have:

$$BR(B_s \to \phi\phi) = [2.04 \pm 0.13(stat) \pm 0.24(syst) \pm 0.69(BR)] \cdot 10^{-5}$$

The dominant contribution to the uncertainty of the measurement arise from

the error of the BR $(B_s \to J/\psi\phi)$.

Comparing this result with that of the first publication [1] which is: $BR(B_s \to \phi\phi) = [1.4 \pm 0.6(stat) \pm 0.6(syst)] \cdot 10^{-5}$, we see that there is a good agreement and a substantial improvement on the statistical uncertainty.

CDFII is expected to collect by the end of 2009 an integrated luminosity of 6-8 fb^{-1} and if the data taking run will be extended to 2010, an additional 2 fb^{-1} will be available. It is clear therefore that, despite the suppression that the Two Tracks Trigger has at high instantaneous luminosity, we expect to conclude the Run II with a significant increase of the data samples of these decays.

This analysis represents the preparatory work and the first step towards the measurement of polarization in the channel $B_s \to \phi\phi$, crucial to solve the *polarization puzzle* [23]. It has allowed a comprehensive understanding of the different signal components in the TTT, the background and the trigger and prescale effects.

Finally, our measurement provides LHC_b with the information needed to estimate the time needed to collect sufficient statistics for their foreseen measurements in the $B_s \to \phi\phi$ channel.

Another important result of this work is the evaluation of a sample of $B_s \to J/\psi\phi$ decays independent from the DI_MUON trigger, which is used in CDFII to study such decays. We have shown that the use of the TTT events can increase of 25 % the sample of $B_s \to J/\psi\phi$ decays, used to make measurements of particular interest such as the determination of effects of CP violation, the calculation of the angles of the unitary triangles and the measurement of $\Delta\Gamma_s$.

Bibliography

[1] D. Acosta et al. (CDF Collaboration), Phys. Rev. Lett. **95**, 031801 (2005).

[2] P.W. Higgs, Phys. Rev. Lett. **12**, 132 (1964); idem, Phys. Rev. **145**, 1156 (1966); F. Englert and R. Brout, Phys. Rev. Lett. **13**, 321 (1964); G.S. Guralnik, C.R. Hagen, and T.W. Kibble, Phys. Rev. Lett. **13**, 585 (1964).

[3] M. Hedron, *Searches for the Higgs Boson*, 34th International Conference on High Energy Physics, Philadelphia,PA; 2008.

[4] H. Fritzsch and M. Gell-Mann, Proc. XVI International Conference on High Energy Physics, Batavia, IL, USA, 1972, eds. J.D. Jackson, A. Roberts and R. Donaldson (Fermilab, Batavia, IL, USA, 1972), Vol. 2, p. 135.

[5] H. Fritzsch, M. Gell-Mann and H. Leutwyl, Phys. Lett. B47 (1973) 365.

[6] A. Pich, Aspects of Quantum Chromodynamics, arXiv:hep-ph/0001118.

[7] F. Mandl, G.Shaw *Quantum Field Theory (Revised Edition).* Wiley and Sons, 1993.

[8] N. Cabibbo, Phys. Rev. Lett. 10, 531 (1963);
M. Kobayashi and T. Maskawa, Prog. Theor. Phys. 49, 652 (1973)

[9] L. Wolfenstein, Phys. Rev. Lett. 51, 1945 (1983).

[10] http://www.slac.stanford.edu/xorg/ckmfitter/plots_fpcp07/ ckmEval_results_fpcp07.html

[11] C. Jarlskog, *commutator of the quark Mass matrices in the Standard Electroweak Model. and a measure of Maximal CP Nonconservation*, Phys. Rev. Lett. 55, 1039-1042 (1985).

[12] HFAG: *Rare B decay Parameters*,
http://www.slac.stanford.edu/xorg/hfag.

[13] G. Valencia, *Angular correlations in the decay $B \to VV$ and CP violation* , Phys. Rev. **D39** 11, 1989.

[14] G.P. Di Giovanni, *B_s mixing, $\Delta\Gamma_s$ and CP violation at the TeVatron* , 2008, [hep-ex/0805.2302v2].

[15] E. Ben-Haim, *The b quark fragmentation function, from LEP to TeVatron*, FERMILAB-THESIS-2004-50.

[16] J. Pumlin, D.R.Stump, and W.L.Tung, Phys.Rev.D 65, 014011 (2002); D.R. Stump et al., Phys.Rev.D 65, 014012 (2002); J.Pumplin et al., Phys.Rev. D 65, 014013 (2002). P. Nason, S.Dawson, and R.K. Ellis, Nucl.Phys.B 303, 607(1988); Nucl.Phys. B327, 49 (1989); Nucl. Phys. B335, 260(1990).

[17] D. Acosta et al. [CDF Collaboration], *Measurement of the J/psi meson and b-hadron production cross sections in $p\bar{p}$ collisions at $\sqrt{s} = 1960$ GeV*, Phys.Rev. D 71, 032001 (2005).

[18] X. Li, G. Lu, Y.D. Yang, *Charmless $\bar{B} \to VV$ decays in QCD factorization*, 2008, [hep-ph/0309136v2].

[19] G. Buchalla, *B Physics Theory for Hadron Colliders*, 2007, [hep-ph/0809.0532v1].

[20] A. Datta, D. London, J. Matias, M. Nagashima and A. Szynkman, *Final-state Polarization in B_s decays*, 2006, [hep-ph/0802.0897].

[21] $B_d \to \phi K^{0*}$: recent measurements can be found in B. Aubert et al. [BABAR Collaboration], Phys.Rev. Lett. 93, 231804 (2004), 98, 051801 (2007),
arXiv:0705.0398 [hep-ex]; K.-F. Chen et al. [Belle Collab-oration], Phys. Rev. Lett. 94, 221804 (2005);
P. Busseyet al. [CDF Collaboration], presented at ICHEP-2006.

[22] B. Aubert et al. [BABAR Collaboration], Phys. Rev. Lett. 97, 201801 (2006); J. Zhang et al. [BELLE Col-laboration], Phys. Rev. Lett. 95, 141801 (2005).

[23] Hsiang-nan Li, *Resolution to the $B_d \to \phi K^*$ polarization puzzle*, 2005, [hep-ph/0411035 v3].

[24] S. Descotes-Genon, J. Matias and J. Virto, *Penguin-mediated $B_{d,s} \longrightarrow VV$ decays and the $B_s - \bar{B}_s$ mixing angle*, 2007, [hep-ph/005.0477v3].

[25] L. Silvestrini, *Searching for New Physics in $b \longrightarrow s$ Hadronic Penguin Decays*, 2007, [hep-ph/0705.1624].

102

[26] R.K. Ellis, W.J. Stirling, B.R. Webber, *QCD and Collider Physics* Cambridge University Press, 2003.

[27] Marriner *Run II handbook.* http://www-bd.fnal.gov/lug/runII_handbook/RunII_index.html September 21, 1998.

[28] http://www-bd.fnal.gov/runII/index.html http://www-bdnew.fnal.gov/operations/rookie_books/rbooks.html

[29] D. P. McGinnis, Fermilab Tevatron status, C. Horak (ed.), proccedings of the Particle Accelerator Conference (PAC 05), (2005).

[30] CDFII Collaboration, *The CDFII detector: Technical Design Report*, FERMILAB-Pub-96/390-E (1996).

[31] D. Mohl et al., *Physics and Technique of Stochastic Cooling*, Phys. Reports **58**, 73 (1980).

[32] P. Gatti,*Performance of the new tracking system at CDFII* , Ph. D. Thesis, University of Padova, FERMILAB-THESIS-2001-23, 2001.

[33] C. S. Hill, *Initial experience with the CDF layer 00 silicon detector*, Nucl. Instr. Methods, **A511**, 118 (2003).

[34] A. Affolder et al, *Intermediate silicon layers detector for the CDF experiment*, Nucl. Instr. Methods, **A453**, 84 (2000).

[35] A. Affolder et al., *CDF Central Outer Tracker*, Nucl. Instr. Methods, **A526**, 249 (2004).

[36] S. Bertolucci et al., *The CDF central and endwall hadron calorimeter*, Nucl. Instr. Methods, **A267**,301 (1988).

[37] A. Ascoli et al., *CDF central muon detector*, Nucl. Instr. Methods, **A268**, 33 (1988).

[38] A. Annovi et al., *CDF: B Physics performance & trigger - operational experience*, Nuclear Physics B (Proc. Suppl.) **170**, 283 (2007)

[39] ROOT, *An Object Oriented Data Analysis Framework by Rene Brun*, http://root.cern.ch.

[40] K. Anikeev, C. Paus, P. Murat, *Description of Bgenerator II*, CDF Note n.5092, August 1999.

[41] D. Lange, A. Ryd, *The EvtGen Event Generator Package*, CHEP proceedings 1998.

103

[42] GEANT, *GEANT-Detector Description and simulation Tool*,
http://www.web.cern.ch/wwwasd/geant/.

[43] S. D'Auria et al., *CDF B Monte Carlo*,
http://www.cdf.fnal.gov/internal/physics/bottom/b-montecarlo/.

[44] S. Donati, G. Punzi, *Two Track Trigger with full SVT simulation*, CDF
Note n.3780, 1998.

[45] Torbjörn Sjöstrand et al, *PYTHIA 6.2, Physics and manual*, 2001, [hep-ph/0108264].
Or *http://www.thep.lu.se/∼torbjorn/pythiaaux/introduction.html*, May
27, 2005.

[46] Donatella Torretta (CDFII Operations Group 2009), personal comunication, january 2009.

[47] Particle Data Group; Phys. Lett. **B667**, 1 (2008).

[48] G. Punzi, in *Proceedings of the Conference for Computing in High-Energy and Nuclear Physics (CHEP 03), La Jolla*, California, 2003,
econf C0303241, TUMT005, 2003.

[49] G. De Lorenzo, M. Rescigno, *Measurement of the polarization amplitudes in $B \to J/\psi K^*$ and $B \to \phi K^*$ using Two Track Trigger at CDFII*
, CDF Note n.8096, July 2006.

[50] S. Pappas, M. Schmidt, *Measurement of the polarization in $B \to VV$
decays*, CDF Note n.4672, 1998.

[51] Y. Gotra, J. Kraus and T. Miao, *Run II Level I Low p_t Muon Trigger
Efficiency Measurement*, CDF Note n.6162, 2003.

[52] D. Bortoletto, *B Physics at Hadron Colliders*, 2002, [hep-ex/0212022v1].

[53] L. Ortolan, Physics Master Degree thesis, (Trieste University, november
2008).

104

List of Figures

105

106

107

List of Tables

109

110

Acknowledgements

Ci sono posti che toccano e cambiano l'animo delle persone, e Trieste è certamente uno di questi.

I tre anni trscorsi qui sono stati intensi, ricchi di espenrienze ed emozioni.

Sono tante le persone che devo ringraziare, per quello che mi hanno insegnato e per essermi state vicine nei momenti difficili, soprattutto in quest'ultimo periodo, ma questa pagina non basta ad elencarle .....

..... però tutti i loro nomi sono scritti nel mio cuore.